Local Infrared Spectroscopy of Highly Doped Semiconductors Structures Based on Scattering-type Nanoscopy and Photoinduced Force Microscopy

Yi Huang

Thèse
de doctorat
de l'UTT

Yi HUANG

Local Infrared Spectroscopy of Highly Doped Semiconductor Structures Based on Scattering-type Nanoscopy and Photoinduced Force Microscopy

Spécialité :
Matériaux, Mécanique, Optique et Nanotechnologie

2018TROY0027 Année 2018

utt
UNIVERSITÉ DE TECHNOLOGIE
TROYES

THESE

pour l'obtention du grade de

DOCTEUR de l'UNIVERSITE DE TECHNOLOGIE DE TROYES

Spécialité : MATERIAUX, MECANIQUE, OPTIQUE ET NANOTECHNOLOGIE

présentée et soutenue par

Yi HUANG

le 21 septembre 2018

Local Infrared Spectroscopy of Highly Doped Semiconductor Structures Based on Scattering-type Nanoscopy and Photoinduced Force Microscopy

JURY

M. J. C. WEEBER	PROFESSEUR DES UNIVERSITES	Président (Rapporteur)
M. A. AMBROSIO	PRINCIPAL SCIENTIST	Rapporteur
Mme A.-L. BAUDRION-BÉAL	MAITRE DE CONFERENCES	Examinateur
M. J.-L. BIJEON	PROFESSEUR UTT	Examinateur
M. A. BRUYANT	MAITRE DE CONFERENCES - HDR	Directeur de thèse
M. T. TALIERCIO	PROFESSEUR DES UNIVERSITES	Examinateur

Abstract

In this thesis, highly doped semiconductor (HDSC) InAsSb nanostructures have been investigated by near-field nanoscopy in the mid-infrared range. First, infrared plasmonic materials are introduced as well as well as the characterization tools used in this thesis. Herein, two types of nanostructured HDSC samples are studied: HDSC 1D gratings and HDSC 2D array. To characterize the HDSC samples, both phase-sensitive scattering type nanoscopy (s-SNOM) and the more recent Photoinduced Force Microscopy (PiFM) are used. The fundamental aspects of these two microscopies are presented and detailed instrumental information is provided. For HDSC 1D gratings, both techniques are used for spectroscopic nano-imaging in the vicinity of the plasma frequency, where the material behaves as an epsilon-near-zero (ENZ) material. The two responses are compared and discussed in terms of model. For HDSC 2D array, the investigation is carried out by s-SNOM. Both localized plasmonic resonance and ENZ properties are observed and compared with analytical simulations. The signature of a highly localized surface plasmon resonance confined on the edge mode is observed in the experimental images, in agreement with electromagnetic simulations.

Acknowledgement

I would like to express my gratitude to all the people who has helped me during the period of my doctoral studies and the writing of this thesis.

First and foremost, I would like to express my gratitude to my supervisors, Prof. Aurélien BRUYANT, for his constant guidance and support in my research. During my four year study, I learned not only knowledge and the methods of doing research from him, but also the attitude to life and research. I could not have finished my PhD without him. Also I would like to thank Prof. Rémi VINCENT, Prof. Sylvain BLAIZE, Prof. Renaud BACHELOT and Prof. Gilles LERONDEL for their suggestions and help during my research.

I am deeply grateful to have Prof. Jean-Claude WEEBER and Prof. Antonio AMBROSIO for agreeing to review my Phd work and I really appreciate all their suggestions about my dissertation. I also would like to thank all my other jury members, Prof. Thierry TALIERCIO, Prof. Anne-Laure BAUDRION and Prof. Jean-Louis BIJEON for the fruitful discussions and comments after my presentation. I am grateful for their kind consideration and encouragement.

I wish to express my gratitude to China Scholarship Council (CSC) for the financial support during the last five years in France. I really appreciate the support for my experiments from French ANR (SUPREME-B, ANR-14-CE26-0015) and Nano'mat. Thanks to all the members from SUPREME-B for offering samples, suggestions and help during my work.

I would like to express my sincere gratitude to Julien VAILLANT and Regis DETURCHE for their help of electronics during my experiment. I also appreciate the helps from Tzu-Heng WU, who has provided many helpful suggestions and supports. Thanks to my colleagues in University of Technology of Troyes: David LEGRAND, LoÏc LE CUNFF, Anna RUMYANTSEVA, Serguei KOCHTCHEEV, Feng TANG, Feifei ZHANG, etc. Thanks the secretaries of the pôle P2MN Mme Patricia ADNET, and the secretaries of

the doctoral school: Mme Isabelle LECLERCQ, Mme Pascale DENIS and Mme Therese KAZARIAN, for their help throughout my PhD study.

I want to thank my friends in UTT for their valuable aids and supports, and all my other friends in France or in China. Special thanks to Mengying REN, Shijie ZHU, Junze ZHOU, Yunlong ZHU, Xi JIA and Ying PENG who always help me and give me their best suggestions. Last but not least, I offer sincere thanks to my mother and all my family members, for their loving consideration and great trust in me through these years.

General introduction

The field of plasmonics considers the interactions of light with the free electrons in a solid state medium, where the electrical carriers behave like a charge-separated gas, i.e a plasma. A major advantage of plasmonic materials and plasmonic structures lies in their ability to confine electromagnetic oscillations to strongly subwavelength volumes. In this thesis, plasmonic materials consisting in highly doped semiconductors (HDSC) are spectroscopically investigated in the infrared range (IR) with scanning probe microscopes. Therefore this thesis deals with IR spectroscopy, IR plasmonics, and IR near-field microscopy.

The word "spectrum" was first coined by Sir Isaac Newton (in 1672) to describe the rainbow of colors observed when the sunlight is passing through a prism. In 1802, William Hyde Wollaston observed missing patches of colors from different sources using an improved prism spectrometer including a slit and a lens to focus the sunlight spectrum on a screen, without being able to explain these absorption lines at that time. Later on, in 1815, the German physicist Joseph von Fraunhofer made decisive instrumental advances by introducing an objective prism for collimated light (a refractor in fact) and an angle measurement system to observe the absorption lines of different light sources[1]. Several years later, he also introduced dispersive gratings. This instrumentation enabled dispersive spectroscopy to become a more precise and quantitative scientific technique. Since then, spectrometry plays a crucial role in experimental science including chemistry[2, 3, 4], biology[5, 6], physics[7] and astronomy[8] to study the interaction between matter and electromagnetic radiation.

In these fields, infrared (IR) spectroscopy is widely used to identify and study material because this spectral region contains the information of vibrational excitations of bonds or groups within molecules. The mid-infrared (mid-IR) region is called the "fingerprint region" ($600-1600\ cm^{-1}$) , because many materials exhibit unique vibrational modes in this frequency range. Nowadays, large databases of infrared spectrum have been collected, which allows for identification of unknown materials by simply comparing their spectrum with the database. However, besides phonon physics, IR spectroscopy can also be used to determine the plasmonic response induced by the free carriers.

The promise of plasmonics in the molecular fingerprint region has been long hindered by material limitations since the plasma frequency ω_p of noble metals lies far above this infrared domain. Recently, the field of infrared plasmonics is witnessing a clear momentum of interest with the rapid development of advanced infrared materials offering unprecedented control over their optical properties. Among a list of candidates[9], there are many promising materials for mid-IR plasmonics such as 2D materials like graphene, owing notably to its dynamic tunability capability when supported on a proper substrate[10], as well as all-semiconductors structures whose plasma frequency can be widely tuned across the fingerprint region by adjusting the dopants density. With such adjustable ω_p, localized surface plasmon resonances can be achieved at a designed frequency below ω_p.

While the spectroscopic response of an assembly of nanostructures can be determined through direct spectroscopy, advanced microscopic methods have to be employed to gain more insight in the plasmonics modes of the structures that are confined in the sample near-field. The growing interest in plasmonic-like IR material is accompanied by a recent blooming of available nano-spectroscopic imaging systems[11, 12, 13] that are highly relevant, if not mandatory, to explore 2D or nano-structured polaritonic materials.

One of the most commonly used technique for recording the IR spectrum is the Fourier-transform infrared spectroscopy (FTIR). The spectral resolution of commercial FTIR can be as accurate as $0.001\ cm^{-1}$. However the spatial resolution of standard FTIR, coupled with the best optical microscopes, is at the scale of several micrometers.

At the end of the nineteenth century, Ernst Abbe and Lord Rayleigh have clearly demonstrated the spatial resolution limit, known as "diffraction limit" for optical microscopy. This "limit" allows early optical microscopy to observe cells through light, but prevent to reach

or approach atomic level. To solve this issue, near-field infrared spectroscopy or infrared nanoscopy has been developed for about 18 years. [1]

The last decade especially is witnessing the emergence of novel nanospectroscopic tools. Nanoscale spatial resolution spectroscopy can be achieved when spectroscopy is combined with *atomic force microscope* (AFM), such as *scattering scanning near-field optical microscopy* (s-SNOM) coupled with tunable laser source [15, 16, 17, 18], *tip-enhanced Raman spectroscopy* (TERS)[19, 20, 21], *photothermal induced resonance* (PTIR)[22, 23, 24], *photo-induced force microscopy* (PiFM)[25, 26] or even more recently *infrared peak force*[27], etc. All of these techniques have emerged as potentially equally relevant characterization techniques to generate a local IR spectra.

In this work, we focus our attention on both s-SNOM and PiFM for investigating highly doped semiconductors that are of great interest for the development of infrared plasmonic systems. With both near-field techniques, hyperspectral nano-imaging can be obtained. These microscopies are based on scanning the sample surface with nanometric probes, illuminated with a laser source, in order to characterize the interactions between nano-optical field and nano-structures. Near-field imaging is found to be indispensable to demonstrate theoretical predictions, to characterize nanophotonic devices and to provide feedback for design improvements. For instance, near field microscopy can be used to image the local density of states[28], to reveal guided modes, to determine local polarization of various samples[29, 30, 31] including waveguides, photonic crystals, microcavities and more generally integrated optical devices. In the infrared range though, most efforts are devoted to the identification of the structure polarizability or dielectric function in order to enable chemical recognition, or to reveal the characteristics of confined phonon-polariton or plasmon-polariton, notably for novel 2D materials.

[1] Higher resolution can also be achieved using far-field microscopy. For example, using shorter photonic or electronic wavelength. In 1933, the first nanoscopic measurements were performed with the invention of the electron microscope, developed by Ernst Ruska after he and Max Knoll developed the first electromagnetic lens two years before[14]. However no information on the infrared spectrum can be obtained with such microscope, unless Electron Energy Loss Spectroscopy can be performed at very small energy which is not currently the case. More recently, new optical approaches referred to as "far-field nanoscopy" have been proposed. On October 8, 2014, the Nobel Prize in Chemistry was awarded to Eric Betzig, W.E. Moerner and Stefan Hell for "the development of super-resolved fluorescence microscopy (e.g., stimulated emission depletion microscopy and stochastic optical reconstruction microscopy)," which brings optical microscopy into the nanodimension.

If the s-SNOM signal has been investigated in many literatures, a quantitative description of the signal scattered by the probe-sample system remains challenging and a benchmarking with new approaches like PiFM are desirables. On the other hand, the signal nature of the more recent PiFM technique is also actively discussed until now. For example, it was pointed out in several studies that this optomechanical technique could be mostly sensitive to the photoexpansion induced by the material absorption rather than the optical force existing between the sample and the local probe.

To conduct this comparison, the investigated samples consist of highly doped InAsSb gratings on undoped GaSb substrate. These all semiconductor samples have been demonstrated to exhibit localized surface plasmon resonance[32] (LSPR) and its plasma frequency falls in the mid-IR region. Increasing the doping level of the HDSC results in a blueshift of the resonance peak while increasing the ribbon width results in a redshift, as confirmed by numerical simulations by Milla et al.[33]. This provides an efficient means of fine-tuning the LSPR properties. As a plasmonic resonator, there is an enhanced electrical field in vicinity of the resonator and the resonance frequency of HDSC is sensitive to the refractive index of the surrounding medium. These optical properties allow HDSC to be potentially used within a mid-IR sensing device combining both surface enhanced infrared absorption (SEIRA) spectroscopy and surface plasmon resonance (SPR) sensing[34].

Interestingly, the near-field optical signal scattered by a nano-probe is found to exhibit sharp variations when the dielectric function is slightly negative and approaches zero. For this reason it is actually convenient to work in this range to detect minute changes in the physical parameters such as doping concentration, stress, defects, etc. Such high near-field sensitivity related to small dielectric function values can hence be obtained in all polar materials in the vicinity of longitudinal optical (LO) phonon resonances[35] (where the complex dielectric function is small), while far-field spectra typically exhibit dissipative lineshapes related to the transverse optical (TO) phonon absorption lines[36], where the imaginary part is large. In principle, a similar sensitivity can also be reached in vicinity of the plasma frequency of the investigated HDSC where the real part of the dielectric function is also crossing zero with a weak imaginary part.

Organization of the thesis

In the present work, the infrared response of sub-wavelength gratings made of highly doped InAsSb on a GaSb substrate is investigated by means of near-field infrared nanoscopy, namely s-SNOM and PiFM.

Fundamental aspects are introduced in Part I (including chapter 1, chapter 2 and chapter 3). The first chapter introduces infrared plasmonics and highly doped semiconductors. The dielectric function of the considered material is accounted for by the Drude model and the investigated material is positioned within the current landscape of promising materials for IR plasmonics. Moreover, the specificity of epsilon-near-zero (ENZ) material in term of near-field response is introduced. In chapter 2, we describe theoretically the near-field optical interaction between s-SNOM probe and sample using analytical models based on a dipole-dipole approximation approach. A theoretical description of the photo-induced force is then given in chapter 3.

Part II (including chapter 4 and chapter 5) is focused on the experiment and discussion of the results. In chapter 4, the experimental details are given. We first introduce the investigated highly doped semiconductor samples. Then experimental setups used in the investigation are introduced: a home-made phase sensitive mid-IR s-SNOM equipped with three quantum cascade lasers (QCL) continuously tunable from 9.1 μm to 11.5 μm and a commercial PiFM (Vistascope from Molecular Vista, inc.). In chapter 5, the experimental images obtained are presented as well as FDTD simulations. Different modes in vicinity of the plasma frequency are observed. Experimental amplitude and phase spectra are obtained by s-SNOM and compared with the photo-induced force spectra obtained by PiFM. Analytical simulations are carried out and compared with experimental data. Detailed discussions of the near-field signals are made in this chapter. Finally, a general conclusion is drawn and some perspectives are presented.

Contents

Abstract 1

Acknowledgement 2

General introduction 4

I Fundamental aspects 1

1 Infrared plasmonics and highly doped semiconductors 2

1.1 Dielectric function of the HDSC 3

1.1.1 General definition of the dielectric function $\varepsilon(\omega)$ 4

1.1.2 HDSC optical constants from Drude-Lorentz model 6

1.1.3 Reflectivity modeling of HSDC with Drude model 10

1.1.4 Surface Plasmon-Polariton mode in metal or HDSC 14

1.1.5 Localized surface resonance (LSPR) 25

1.2 Potential materials for IR plasmonics 26

1.2.1 Silicon and Germanium 29

1.2.2 III-V semiconductor 30

1.2.3 Transparent Conducting Oxides 32

1.2.4 2D Plasmonic Materials 33

1.3 Conclusion 34

2 Fundamental aspects of s-SNOM 35

2.1 A short historical overview 36

2.2 Different types of SNOM . . . 37
2.2.1 Aperture SNOM (a-SNOM) . . . 38
2.2.2 s-SNOM . . . 39
2.2.3 Hybrid-probe SNOM . . . 41
2.2.4 Probe choice . . . 42
2.3 Analytic models of probe-sample interaction in s-SNOM . . . 42
2.3.1 Dipole approximation . . . 43
2.3.2 Flaws and improvement of the Dipole model . . . 50
2.4 Conclusion . . . 54

3 Fundamental aspects of PiFM **55**
3.1 Background introduction of PiFM . . . 56
3.2 Comparison with other near-field spectroscopy techniques . . . 61
3.3 Analytic approximation of photo-induced force . . . 64
3.3.1 Optical force calculation based on Maxwell's stress tensor . . . 65
3.3.2 Dipole-dipole approximation between probe and particle . . . 67
3.3.3 Dyadic Green's function method for PiFM . . . 70
3.4 Conclusion . . . 72

II Near field spectroscopic investigation **74**

4 Experimental details **75**
4.1 Investigated HDSC samples . . . 76
4.1.1 Fabrication procedure . . . 76
4.1.2 HDSC 1D gratings . . . 77
4.1.3 2D periodic rectangular nanoantenna array . . . 83
4.2 Mid-IR nanoscopy: setups and experimental development . . . 84
4.2.1 s-SNOM . . . 85
4.2.2 PiFM setup . . . 95
4.3 Conclusion . . . 106

5 Experimental results and discussions **108**

5.1 Nano-spectroscopic imaging of the HDSC submicronic ribbons 109
5.1.1 s-SNOM images and spectra 109
5.1.2 PiFM images and spectra 119
5.2 Near-field optical images of 2D periodic nanoantenna array 127
5.3 Conclusion 130

Conclusion and perspectives **132**

Résumé étendu **136**
1 Aspects fondamentaux 136
2 Partie expérimentale 146

Bibliography **159**

List of Figures

1.1.1 Drude's dielectric functions of bulk plasmonic materials for different damping constants. . . . 9
1.1.2 Example of reflectivity spectra measured on highly doped III-V semiconductors. . . . 10
1.1.3 Simulation of far field signal of HDSC thin film. . . . 13
1.1.4 Representation of different modes at a single interface. . . . 16
1.1.5 Dispersion relation of a SPP (single interface). . . . 18
1.1.6 Radiation pattern of long Au nanowire on a IR polaritonic material. . . . 20
1.1.7 Dispersion relation of the two SPP modes of HDSC in a slab (lossless case). 21
1.1.8 ENZ confined modes. . . . 22
1.1.9 PTIR spectrum of SiO_2 films. . . . 23
1.1.10 Simulation of Berreman mode in 50 nm SiO_2 film. . . . 24
1.1.11 Simulation of ENZ mode in5 nm SiO_2 film. . . . 24
1.1.12 Sketch of wedge geometry. . . . 25
1.2.1 Band diagram and density of states of metal and highly doped semiconductor. 27
1.2.2 Classification of potential materials for plasmonics. . . . 29

2.1.1 Electromagnetic field regions: from near-field to far field. . . . 36
2.2.1 Operation mode of a-SNOM. . . . 38
2.2.2 Illumination of s-SNOM. . . . 39
2.2.3 Mid-IR s-SNOM investigation of a polar material SiC in vicinity of phonon resonance. . . . 40
2.2.4 Example of hybrid-probe. . . . 42
2.3.1 Model of probe-sample interaction and dipole image theory. . . . 44

2.3.2 Probe-dipole illumination and detection system. 46
2.3.3 Magnitude of the dimensionless effective polarizability for a spherical scatterer. 50

3.1.1 PiFM of 6-tamra dye molecule images on glass as a function of wavelength. 57
3.1.2 PiFM image of YOYO-3 dye molecule images on glass as a function of wavelength. 57
3.1.3 Fingerprint region of PS-b-P2VP. 59
3.1.4 FDTD simulations and PiFM image of gold disk dimers. 60
3.2.1 Operational scheme of PTIR microscopy. 62
3.2.2 Operational scheme of PFIR microscopy. 63
3.3.1 Simulation of force vs distance relationship of PiF. 67
3.3.2 The particle-dipole model of the PiFM system. 68
3.3.3 The probe-dipole model of the PiFM system. 70
3.3.4 Calculated $\langle \mathbf{F}_z \rangle$ on a gold tip on pure glass and gold film covered glass. . . . 72

4.1.1 Process flow for sample fabrication. 77
4.1.2 HDSC gratings. 77
4.1.3 High-resolution X-ray diffraction of HDSC gratings. 78
4.1.4 Reflectance spectra in p-polarized light with an angle of incidence of 60°. . . 79
4.1.5 Experimental complex dielectric function $\varepsilon(\lambda)$ of InAsSb. 80
4.1.6 Reflection FTIR spectra of HDSC gratings with different angles of incidence. 82
4.1.7 FDTD simulation of reflectance of HDSC gratings. 82
4.1.8 2D periodic nanoantenna array. 84
4.1.9 Micro-FTIR spectrum of HDSC 2D grating. 84
4.2.1 Probe fabrication. 86
4.2.2 Michelson interferometer system used for GLIA detection in s-SNOM. . . . 88
4.2.3 Example of background suppression with GLIA. 91
4.2.4 Approach curve of s-SNOM. 93
4.2.5 A photo of mid-IR laser sources used in s-SNOM. 94
4.2.6 s-SNOM home-built setup. 95
4.2.7 PiFM force detection schema. 96

4.2.8 Home-made setup for laser modulation. 99
4.2.9 PiFM image with modified laser system. 100
4.2.10 Drawing of focusing path of PiFM. 101
4.2.11 Visible PiFM with objective scan. 102
4.2.12 z component imaging of the laser spot (PiFM). 103
4.2.13 PiFM images by transmission mode and s-SNOM signal collection from top. 104
4.2.14 PiFM: Side illumination system. 105
4.2.15 Laser spot imaging in reflection mode. 106

5.1.1 Zoomed s-SNOM images of HDSC gratings. 111
5.1.2 Scattering cross section of a vertically polarized dipole above a surface. . . . 112
5.1.3 FDTD simulation of electric field amplitude for selected wavelengths. 114
5.1.4 Near-field spectra on HDSC gratings obtained with s-SNOM. 116
5.1.5 Relative near field signal on HDSC for different thickness. 117
5.1.6 HDSC Gratings with lower plasma frequency. 119
5.1.7 PiFM images of HDSC gratings. 120
5.1.8 Representation of dipole-image dipole model of PiFM. 122
5.1.9 Near-field spectra on HDSC gratings obtained with PiFM. 124
5.1.10 FDTD simulation of optical force. 125
5.2.1 s-SNOM image of 2D array. 128
5.2.2 s-SNOM optical image of 2D array at different wavelengths. 129
5.2.3 FDTD simulation reflectance of 2D array 129
5.2.4 FDTD E field simulation of 2D array at different wavelength (XZ plan). . . 130

1.1 Simulation du signal en champ lointain et champ proche de HDSC. 138
1.2 Système dipôle/ dipôle image éclairé sous angle. 142
1.3 Modèle dipôlaire initial d'un système PiFM. 145
2.1 Morphologie des rubans HDSC 147
2.2 Morphologie des nanoantennes rectangulaires périodiques 2D. 148
2.3 Configuration s-SNOMs. 149
2.4 Système PiFM 150
2.5 Images s-SNOM des réseaux HDSC. 151

2.6 Spectres de champ proche sur HDSC obtenu avec s-SMOM. 153
2.7 Images PiFM de réseaux HDSC. 154
2.8 Spectres de champ proche sur HDSC obtenus par PiFM. 156
2.9 Image s-SNOM de l'échantillon 2D. 157

Part I.

Fundamental aspects

1. Infrared plasmonics and highly doped semiconductors

Contents

1.1 Dielectric function of the HDSC **3**
1.1.1 General definition of the dielectric function $\varepsilon(\omega)$ 4
1.1.2 HDSC optical constants from Drude-Lorentz model 6
1.1.3 Reflectivity modeling of HSDC with Drude model 10
1.1.4 Surface Plasmon-Polariton mode in metal or HDSC 14
1.1.5 Localized surface resonance (LSPR) 25
1.2 Potential materials for IR plasmonics **26**
1.2.1 Silicon and Germanium 29
1.2.2 III-V semiconductor 30
1.2.3 Transparent Conducting Oxides 32
1.2.4 2D Plasmonic Materials 33
1.3 Conclusion **34**

For the last few decades, plasmonics has been a hot topic for researchers notably for light enhancement, sensors and detectors. More recently IR plasmonic is emerging as a potential tool to enhance infrared spectroscopy capability, especially through the technique named SEIRA (Surface Enhanced InfraRed Absorption spectroscopy), which can be used to identify and study material in small concentration due to local field enhancement in the vicinity of infrared plasmonic resonators. In fact, the field of infrared plasmonics is

witnessing a clear momentum of interest with the rapid development of advanced infrared materials offering unprecedented control over their optical properties. These properties are primarily described by the dielectric function of the considered material, or the frequency-dependent conductivity in the case of 2D materials. As will be detailed in chapter 2, the near-field optical techniques can be particularly sensitive to the dielectric function of the investigated sample.

In this chapter, first we present the dielectric function of the highly doped semiconductor (HDSC) materials considered in this work, whose behavior is mostly governed by the conduction electrons. The Drude model is therefore presented, as it can precisely account for the HDSC response. Secondly, we introduce reflectivity modeling of HSDC with Drude model and then describe the surface plasmon-polariton mode in HDSC. Finally we position the HDSC material in the landscape of IR plasmonics material and briefly introduce the notion of epsilon-near-zero (ENZ) material.

1.1. Dielectric function of the HDSC

The response of a material to an external electric field is primarily determined by the polarization vector, which is connected to the electrical field via the permittivity or dielectric function ε. In other words, the dielectric function ε rules the optical response of a solid. For harmonic fields ranging from UV to THz, the dielectric function has typically a strong dependence on frequency and is conveniently treated as a complex function of the frequency ω of the impinging light frequency ω:

$$\varepsilon(\omega) = \varepsilon'(\omega) + i\varepsilon''(\omega) \tag{1.1.1}$$

The dielectric function, is the key parameter describing the electrical and optical properties of a material versus frequency, wavelength, or energy. The situation valid in the majority of metals is to consider that the optical properties are mainly due to the behavior of conduction electrons. Below the plasma frequency ω_p, the real part ε' of the permittivity becomes negative accounting for the collective oscillations of free carriers in the material[37], which is a required condition for the excitation of a plasmonic surface or localized mode. The

imaginary part of the dielectric function ε'' is related to the losses associated with the scattering of conduction electrons by defects, surface states, and lattice vibrations[38].

The contribution of the free electrons or holes in metals or semiconductors is typically accounted for using the classic Drude model. In the following, this model is used to correctly describe the infrared response of the considered highly doped semiconductors.

1.1.1. General definition of the dielectric function $\varepsilon(\omega)$

In the absence of bound (induced) charges, like in vacuum, the dielectric function ε is a constant[1] $\varepsilon_o = 4\pi/K_c$, given by the Coulomb proportionality constant (K_c) in the Coulomb's force expression. This permittivity defines the magnitude of electric flux density created by free charges in vacuum.

In an isotropic polarizable medium, the complex dielectric function $\varepsilon(\omega)$ allows to discriminate the contribution of the free and bound charges in the electric field expression. $\varepsilon(\omega)$ typically depends on the electrical frequency ω, and is usually defined in terms of electric field $\mathbf{E}(\omega)$ and polarization $\mathbf{P}(\omega)$:

$$\varepsilon\mathbf{E} = \varepsilon_0\mathbf{E} + \mathbf{P} \tag{1.1.2}$$

where the frequency dependence is omitted for conciseness. The polarization vector[2] $\mathbf{P}$ describes the electrical polarization induced by bound charges, which corresponds to the net dipole moment per unit of volume in the material under consideration. The left term $\varepsilon\mathbf{E}$ is the electric displacement field $\mathbf{D}$[3], according to the constitutive equation. In practice, it is more convenient to use $\mathbf{D}$ rather than $\mathbf{E}$, because $\mathbf{D}$ is not related to the (bound) charges induced by $\mathbf{E}$ but is only related to the external (free) charges[4]. The linear relationship between $\mathbf{P}$ and $\mathbf{E}$ is written:

$$\mathbf{P} = \varepsilon_0\chi\mathbf{E} \tag{1.1.3}$$

[1] ε_0 is the vacuum permittivity that has a value of approximately $8.85 \times 10^{-12} F/m$.
[2] The dipole moment density vector $\mathbf{P}$ is in (C/m²) .
[3] $\mathbf{D}$ is also known as electrical induction or flux density vector (C/m²). The term "displacement" field, introduced by Maxwell, is kept by tradition.
[4] i.e: $div\,\mathbf{D} = \rho_{ext}$ while $div\,\mathbf{E} = \rho_{ext} + \rho_{ind}$.

where χ, which characterizes the polarization created by the electric field, is zero in vacuum, and is named dielectric susceptibility. By introducing the relative, dimensionless, dielectric function $\varepsilon = \varepsilon/\varepsilon_o$, the relation between these quantities is simply:

$$\mathbf{E} = \varepsilon\mathbf{E} - \chi\mathbf{E} \quad i.e: \quad \chi = \varepsilon - 1 \tag{1.1.4}$$

The initial benefit of this separation, again, is that the flux of $\varepsilon\mathbf{E}$ depends solely on the external charges. In order to derive an expression for ε, we can write:

$$\varepsilon(\omega) = 1 + \chi(\omega) = 1 + \frac{P}{\varepsilon_o E} \tag{1.1.5}$$

This can be generalized by considering that the dipole moment density P can have distinct origins, e.g. the contribution of phonons in the case of polar materials (Lorentz oscillator model), the contribution of free electrons (Drude model), etc. Therefore, the dielectric function can be more explicitly expressed as:

$$\varepsilon(\omega) = 1 + \chi_{interband} + \chi_{phonon} + \chi_{Drude} \tag{1.1.6}$$

In the case of the highly doped materials that we will consider, we will be working at optical frequencies (near 1000 cm^{-1}) far from interband (at higher energies) or phonon resonance (at lower energy). Therefore, the dielectric function will be considered as having the following form in the investigated range:

$$\varepsilon(\omega) = \varepsilon_\infty + \chi_{Drude} \tag{1.1.7}$$

where ε_∞ accounts for the real, non resonant, background polarizability, or in other words the refractive index of the undoped material $\varepsilon_\infty = n^2_{undoped}$. Before evaluating the dipole moment density provided by the Drude model, more insight can first be gained by combining constitutive equation and Maxwell's equations.

In matter, Maxwell's equations connect the four macroscopic fields **D** (electrical induction), **E** (the electric field), **H** (the magnetic field), **B** (the magnetic induction) with the charge density ρ_{ext} and the free current density $j_{\mathbf{ext}} = \sigma\mathbf{E}$, as follow:

$$div\,\mathbf{D} = \nabla \cdot \mathbf{D} = \rho_{ext} \quad and \quad \nabla \cdot \mathbf{B} = 0 \; (Gauss's\,laws) \tag{1.1.8}$$

$$rot\,\mathbf{E} = \nabla \times \mathbf{E} = \frac{-\partial B}{\partial t} \quad and \quad \nabla \times \mathbf{H} = \mathbf{j_{ext}} + \frac{\partial D}{\partial t} \; (Faraday's\,law \,\&\, Ampere's\,law) \tag{1.1.9}$$

With the help of constitutive equations ($\mathbf{B} = \mu\,\mathbf{H}$ and $\mathbf{D} = \varepsilon_{real}\,\mathbf{E}$), and considering the harmonic regime (where we can redefine $\mathbf{D} = \varepsilon\,\mathbf{E}$, as previously with $\varepsilon = \varepsilon' + i\varepsilon''$), the last two equations can be made more symmetric:

$$\nabla \times \mathbf{E} = -j\omega\mu\,\mathbf{H}$$

$$\nabla \times \mathbf{H} = \sigma + j\omega\varepsilon_{real}\frac{\partial D}{\partial t} = j\omega\varepsilon\,\mathbf{E}$$

where the permittivity is now complex, with $\varepsilon' = \varepsilon_{real}$ and $\varepsilon'' = -\sigma/\omega$. The relative dielectric function of a lossy material is then represented as:

$$\varepsilon(\omega) = \varepsilon(\omega)' + i\varepsilon(\omega)'' \; with \; \varepsilon(\omega)'' = \frac{\sigma(\omega)}{\omega\varepsilon_0} \tag{1.1.10}$$

1.1.2. HDSC optical constants from Drude-Lorentz model

Drude model of electrical conduction, proposed in 1900 by Paul Drude, allows us to introduce the notion of dielectric function and make it possible to understand the influence of quasi-free electrons on the optical properties. For majority of metals, the optical properties are mainly due to the behavior of conduction electrons, which is the same situation for semiconductors. So we use Drude model to describe the dielectric function of our HDSC sample and detailed parameters are listed in Chapter 4.

This model considers the electrons to be a gas of charge carriers traversing in a medium of uniformly distributed positive ions. Several assumptions are used in the Drude model:

- Electrons are considered as classical particles. Without external field, the average value of the velocity distribution of the free charges (given by the temperature) is zero. When an external electric field is applied, the motion of each electron between collisions is rectilinear as described by the Newton's laws of motion.

- An electron is assumed to experience a collision in an infinitesimal time interval dt, with a probability per unit time of dt/τ. The time τ is known as the collision time or mean free time. In Drude's model, τ is assumed to be independent of the electron position and is independent of time.

- The velocity and direction of the electron after a collision only depend on the local temperature distribution again and is completely independent of the velocity before the collision.

From these assumptions, the electrical conductivity and therefore the dielectric function of a plasma can be obtained. The starting point is the electronic equation of motion, similar to the one used in the Lorentz model of dipole oscillators but without restoring force. The two considered forces are the damping force proportional to the velocity $\mathbf{v}$, and the driving force:

$$\frac{d}{dt}\mathbf{p}(t) = -\frac{\mathbf{p}(t)}{\tau} + e\mathbf{E} \tag{1.1.11}$$

where $\mathbf{p}(t) = \mathbf{m}^*\mathbf{v}(t)$ is the average momentum per charge carrier, τ is the momentum scattering time and e, m^*, N are respectively the electron charge, effective mass and number of electrons or holes per unit volume. Then, considering an harmonic driving field of the form $\mathbf{E}(t) = \mathbf{E}_o e^{i\omega t}$, $\mathbf{v}(t)$ is obtained providing an expression for the current density $\mathbf{J}(t) = Ne\mathbf{v}(t) = \sigma(\omega)\mathbf{E}(t)$. The complex expression for conductivity is derived as:

$$\sigma(\omega) = \frac{\sigma_0}{1 - i\omega\tau} \; with \; \begin{cases} \sigma_o = C\tau \\ and \; C = \frac{Ne^2}{m*} \end{cases} \tag{1.1.12}$$

By replacing $\sigma(\omega)$ in Equation 1.1.10, we obtain the complete expression of the dielectric function:

$$\varepsilon(\omega) = \varepsilon_\infty + i\frac{\sigma(\omega)}{\omega\varepsilon_0} = \varepsilon_\infty\left(1 - \frac{\omega_p^2}{\omega^2 + i\gamma\omega}\right) = \varepsilon'(\omega) + i\varepsilon''(\omega) \tag{1.1.13}$$

where $\omega_p = \sqrt{\frac{C}{\varepsilon_0\varepsilon_\infty}}$ denotes the plasma frequency, and the relaxation rate$\gamma = \tau^{-1}$.

It is interesting to express ε in a canonical form in order to compare plasmonic materials. Dividing ε by the background polarizability, the reduced dielectric function $\tilde{\varepsilon} = \varepsilon/\varepsilon_\infty$ can be expressed as a function of two normalized parameters $\tilde{\omega} = \omega/\omega_p$ and $\tilde{\gamma} = \gamma/\omega_p$:

$$\frac{\varepsilon(\tilde{\omega})}{\varepsilon_\infty} = 1 - \frac{1}{\tilde{\omega}}\frac{1}{(\tilde{\omega} + i\tilde{\gamma})} = \tilde{\varepsilon}'(\omega) + i\tilde{\varepsilon}''(\omega) \tag{1.1.14}$$

From this result, the real and imaginary part can be expressed as:

$$\begin{cases} \tilde{\varepsilon}' & = 1 - \frac{1}{\tilde{\omega}^2+\tilde{\gamma}^2} \approx 1 - \frac{1}{\tilde{\omega}^2},\ for\, \tilde{\omega} \gg \tilde{\gamma} \\ \tilde{\varepsilon}'' & = \frac{\tilde{\gamma}}{\tilde{\omega}\left(\tilde{\omega}^2+\tilde{\gamma}^2\right)} \approx \frac{\tilde{\gamma}}{\tilde{\omega}^3}\ for\, \tilde{\omega} \gg \tilde{\gamma} \end{cases} \tag{1.1.15}$$

As exemplified later on (cf. Figure 1.1.2), τ remains typically in the order of few $10^{-13}\,s$ at room temperature for common semiconductors. Therefore, the value for $\tilde{\gamma}$ in good quality HDSC is typically smaller than 0.1, so that approximation above are correct on a large bandwidth[5]. In that case, the sign of dielectric function $\varepsilon'(\omega)$ crosses zero at $\omega \approx \omega_p$ ($\lambda = \lambda_p$), switching from positive to negative values as the wavelength increases. This also indicates that ε'' is small ($\ll 1$) for $\omega =\lesssim \omega_p$.

This behavior is shown in:

[5]The approximation is also valid for metals even if τ is in the order of $10^{-14}s$, this is because the plasma frequency is also much higher.

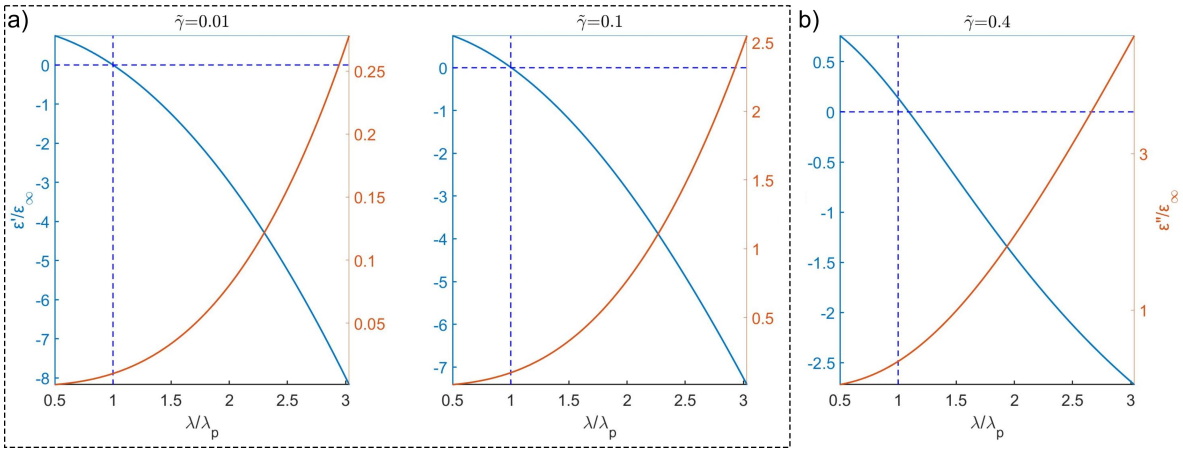

Figure 1.1.1.: Drude's dielectric functions of bulk plasmonic materials for different damping constants $\tilde{\gamma} = \gamma/\omega_p$. This parameter is typically smaller than 0.1.

Since $\tilde{\gamma}$ remains small (cf. Figure 1.1.1 a)), we see that at $\omega = \omega_p$ we have $\varepsilon' = 0$. We also observe that ε' nearly doesn't change, while ε'' scales with $\tilde{\gamma}$.

- Refractive index and extinction coefficient

From the wave equation we know that the complex refractive index $n = n_r + i\kappa$ is directly related to ε through the relation $\varepsilon = n^2$. Therefore:

$$\begin{cases} \varepsilon' &= n_r^2 - \kappa^2 \\ \varepsilon'' &= 2n_r\kappa \end{cases} \tag{1.1.16}$$

which gives:

$$\begin{cases} n_r &= \frac{1}{\sqrt{2}}\left(|\varepsilon| + \varepsilon'\right)^{1/2} \approx \sqrt{\varepsilon'} \;\; for\, \omega \lesssim \omega_p \\ \kappa &= \frac{1}{\sqrt{2}}\left(|\varepsilon| - \varepsilon'\right)^{1/2} \approx \frac{\varepsilon''}{2\sqrt{\varepsilon'}} \;\; for\, \omega \lesssim \omega_p \end{cases} \tag{1.1.17}$$

where the latter approximations are valid for $\omega =\lesssim \omega_p$ considering that in that case ε'' is small enough. This result indicates that a plane wave $E_o e^{i(kr-\omega t)}$, propagating with a wave vector $k = nk_o$ along a direction z is decaying like $e^{-\alpha z}$, with an absorption coefficient $\alpha = 2\kappa\frac{\omega}{c}$.

1.1.3. Reflectivity modeling of HSDC with Drude model

The validity of the Drude model to account for the plasmonic response of HDSC can be judged from reflectivity measurement, using spectrometers with large IR bandwidth such as conventional Fourier Transform InfraRed (FTIR) spectrometers working in quasi-normal incidence. The reflectivity is determined from the complex material refractive indexes $n = n_r + i\kappa$ with the help of the Fresnel coefficients. For normal incidence on a bulk material, the reflection in energy is given by:

$$R = \left|\frac{n-1}{n+1}\right| = \frac{(n_r-1)^2+\kappa^2}{(n_r+1)^2+\kappa^2} \tag{1.1.18}$$

This expression can be used to fit the experimental data. For degenerate semiconductors[6] below the plasma frequency, $R(\tilde{\omega})$ is correctly approximated by the Hagen-Rubens expression $R(\tilde{\omega}) = 1 - 2\sqrt{\frac{\tilde{\omega}\tilde{\gamma}}{2\pi}}$, which is valid for most metal in the infrared. Additional information from other characterization methods can help in the fitting task. Especially, the charge carrier concentration can be obtained with Hall-effect measurement. Example of reflectivity spectra measured on highly doped semiconductor are shown in Figure 1.1.2.

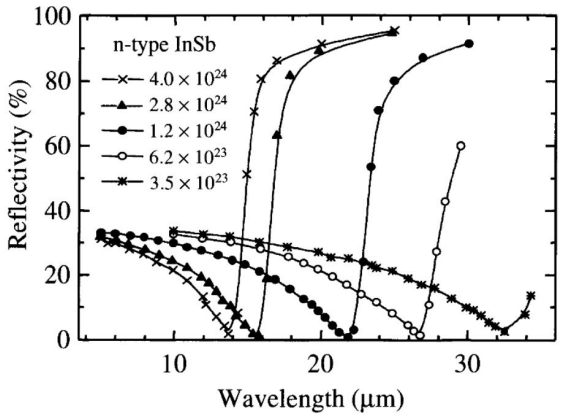

N (cm^{-3})	τ (s)	m*/m$_e$	$\tilde{\gamma}$
3.5 ×10^{17}	4.7 ×10^{-13}	0.023	0.039
6.2 (5) ×10^{17}	4.0 ×10^{-13}	0.029	0.038
1.2 ×10^{18}	4.0 ×10^{-13}	0.032	0.029
2.8 ×10^{18}	3.2 ×10^{-13}	0.040	0.026
4.0 ×10^{18}	2.6 ×10^{-13}	0.041	0.028

Figure 1.1.2.: Example of plasma edges measured on n-doped III-V semiconductor. The spectra can be correctly fitted using the Drude model parameters on the right table. The electron density is in cm^{-3} in the table, the other values are in USI. Adapted from[39].

[6]The HDSC we will study are also entirely degenerate at room temperature.

These measurements are performed at frequencies smaller than the semiconductor band gap (large wavelengths), and higher than the phonon absorption band (near 50 μm in InSb). After a minimum close to the plasma wavelength, a strong, metal-like, reflection is progressively appearing as the dielectric function becomes more and more negative based on the Drude model prediction. Usually, such transition is not so clearly observed in noble metals where the plasma frequency is at a much larger frequency. This is due to the contribution of interband transition in the visible or UV range.

From the above equations, the zero reflectivity can be determined analytically. This minimum is slightly blue-shifted compared to ω_p, more precisely, it is obtained for:

$$\omega_{min}^2 = \frac{\varepsilon_\infty}{\varepsilon_\infty - 1}\omega_p^2, \tag{1.1.19}$$

not far from $\varepsilon' = 1$ (vacuum or air permittivity value). This formula is useful to determine the plasma frequency or effective mass of the considered HDSC material.

Far-Field Spectroscopy (FTIR)

In our work, we use reflective mode of FTIR and the reflectance is described as Equation 1.1.18. In the FTIR spectrum, a resonant dip in the reflectivity near ω_p can be observed. This provides an easy way to measure the plasma wavelength and the carrier concentration[40].

FTIR is a routine analytical technique[41] to obtain infrared spectrum of absorption or emission of a solid, liquid or gas. In IR plasmonics, the so called "Brewster" and "plasmonic" modes can be specidically analyzed in the reflectance spectra provided by FTIR. The world's first commercial FTIR spectrometer[7] appeared in 1969 after the minicomputers were available because electronic computer was needed to perform the Fourier transform. FTIR spectrometers are mostly used for measurements in the mid and near IR regions. The spectral resolution of standard FTIR instruments is $4cm^{-1}$ while higher resolution can be obtained by increasing the maximal retardation, which is the oscillation

[7]FTIR consists of an IR light sources, a Michelson interferometer, a sample support, a detector and some electronics for conversion of raw data (analog signal) into real spectrum (numeric signal) using fast Fourier transform algorithm.

amplitude of the movable mirror[8]. The study of high-resolution FTIR has been a great interest[42].

The interferogram measured by the detector is turned into a spectrum by applying the Fourier transform. In FTIR measurement, a gold mirror is measured first as the reference signal for reflection or for transmission the reference is obtained in air. Then the relative reflectance or transmittance of the sample is normalized to the reference spectrum.

Compared to standard dispersive spectrometer, FTIR has some advantages[43]:

- Fellgett's advantage[44]: the multiplex is due to the simultaneous collection of the information from all wavelengths in one acquisition.
- Jacquinot's advantage: instead of entrance and exit slits used in dispersive system, the circular aperture allows more light through and the interferometer throughput of FTIR is only determined by the diameter of the collimated beam coming from the source.
- Connes' advantage: the wavelength scale of FTIR is more stable and accurate because it is calibrated by a laser beam of known wavelength that passes through the interferometer.
- FTIR is less sensitivity to stray light because the apparent wavelength is determined by the modulation frequency in the interferometer. Furthermore, FTIR has a high signal-to-noise ratio due to the short acquisition time and high intensity.

$\rightarrow$However, when it comes to high loss materials or extra thin films, the FTIR (and far-field spectroscopy in general) is less sensitive. This is shown through simulated reflectivity spectra on HDSC (cf. Figure 1.1.3). This should be compared with the reflectivity spectra obtained on thick HDSC film samples (Figure 1.1.3 (a)).

[8]In FTIR, a movable mirror is included in the Michelson interferometer. An optical path difference is introduced when they are reflected by the mirror and come back to the beamsplitter and interfere. As the movable mirror goes to different position, the optical path difference varies and each wavelength would go through constructive and destructive interferences containing all the information for all the wavelength of the source.

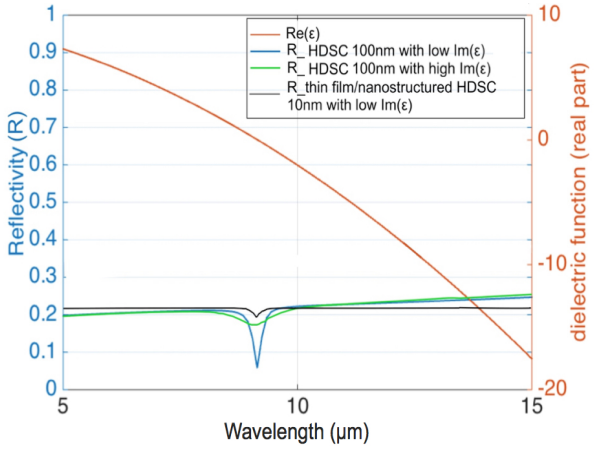

(a)

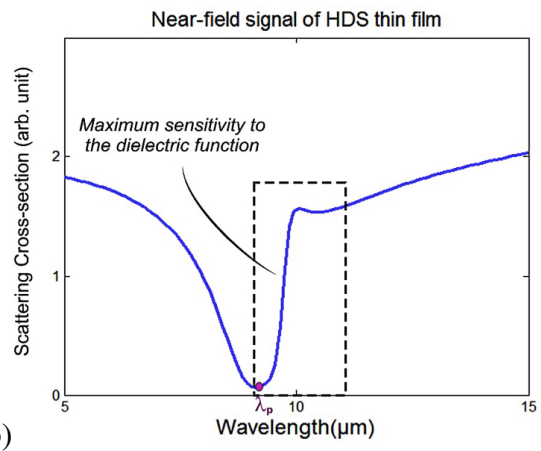

(b)

(c)

Simulation of R with Drude model	Thickness of InAsSb	Incident angle	Refractive index of substrate GaSb	The relaxation rate γ of InAsSb	ε_∞ (InAsSb)	Plasma frequency of InAsSb	Imaginary part of dielectric function InAsSb
Bulk HDSC with low loss	100nm	45°	3.77	$3.8*10^{12}$	10.4	$6.64*10^{14}$	Im (ε)_Drude
Bulk HDSC with high loss	100nm						5*Im (ε)_Drude
Thin film HDSC	10nm						Im (ε)_Drude

Figure 1.1.3.: Simulation of far field signal of HDSC thin film: (a) Far field reflectivity of HDSC; (b) Near field signal of 10nm HDSC thin film; (c) Parameters used for the simulation of R. For all the simulations, the bulk substrate is made of undoped GaSb, while the thin top layer of InAsSb is highly doped.

We can see from Figure 1.1.3 (a) that the reflectivity increases as the real permittivity goes from positive to negative. Comparing high loss and low loss HDSC 100 nm film, the change of reflectance at plasma frequency decreases a lot (the high loss HDSC is simulated by multiplying its imaginary permittivity by five). Then if we decrease the thickness of the film to 10 nm, the reflectivity dip will be much less obvious (c.f Figure 1.1.3 (a)).

→On the other hand, the near field signal shows a strong variation when epsilon is near zero (c.f Figure 1.1.3 (b)). The dispersion relation of HDSC described in next section will

help to have a better understanding of the signal sensitivity near λ_p. The expression of the near-field signal will be detailed in the next chapter.

1.1.4. Surface Plasmon-Polariton mode in metal or HDSC

In matter, light propagating as $E_o e^{i(kr-\omega t)}$ is always coupled with bound or free charges. Therefore a "pure" photon only exists in vacuum (in the absence of charge). In this specific case, the frequency-wave vector dispersion relation is rigorously linear[9]:

$$\omega(k) = ck$$

where the slope is the constant c which is both the phase velocity and group velocity (ω/k and $\partial\omega/\partial k$) of light in vacuum, which also defines the free space wavelength λ_o via $k = k_o = \frac{2\pi}{\lambda_o}$. On the other hand, in matter, the phase velocity $v = c/n$ of the light wave is typically wavelength dependent, i.e: $\omega(k) = v(k)k$. As the photon propagates, it interacts with the charges and this new coupled quasi-particle is named *polariton* whenever the signature of a strong coupling exists. For a metal or doped semiconductor, the corresponding polariton is named *plasmon-polariton*. From the Drude model, the existence of a strong coupling between plasma and light is obvious when we approach the plasma frequency, as we will detail below.

Polaritonic materials, like metal, doped semiconductor or polar material, can sustain an electromagnetic surface mode. Usually, the surface is the interface separating the polaritonic material from another medium such as air or a dielectric material with positive permittivity. This situation is sketched in Figure 1.1.4 for a plane interface separating two media (n_1, n_2) in $z = 0$. The surface mode is characterized by a light confinement at the surface: the light presents an exponential decay on both sides of the interface. This behavior is made possible when ε is mostly real and negative on a given spectral range which is the case in polaritonic materials (before the plasma frequency or longitudinal optical phonons for polar material). This can be understood from the continuity of $D_z = \varepsilon E_z : D_z$ being continuous, ε has to change sign across the interface, so that the electric field sign, i.e. its

[9]This relation is figuring a light cone when representing $\omega(k_x, k_y)$. It is usual to plot the frequency-wave vector dispersion in unit of k_o/c so that the slope of this cone is the refractive index, i.e. one in vacuum.

direction, is reversed across the interface in order to maintain the charge resonance on the surface. Near the plasma frequency, this leads to a strong coupling between the driving field and the plasma at the interface. This surface mode is known as Surface Plasmon Polariton (SPP). It also exists with phonon (SPhR)[10].

Below, we consider the case of single interface before treating the case of a slab. This analysis is relevant as our samples will mostly consist of truncated slabs of HDSC materials[11].

SPP on a single interface

Before describing further the simplest SPP mode of a single interface, let's consider different solutions of the wave equation satisfying the boundary condition shown on Figure 1.1.4. In the two first cases (a) and (b), where dielectrics are considered, we can have an incident wave, a reflected one and a transmitted (evanescent) one.

In the first case, we have an exponential decay in the upper medium. This can be observed when passing from a high to a low refractive index as shown in Figure 1.1.4 a), when the incidence angle is exceeding the critical angle. In that case, the parallel wave vector component β which is always conserved across plane interfaces is higher that $k_1 = n_1 k_0 = \sqrt{\beta^2 + k_{z1}^2}$ generating an evanescent wave in this medium, since the vertical component of the wave vector has to be imaginary. These modes can also be excited with a point-like source in the sample near-field: the light emitted or scattered by the source will indeed radiate most of its power above the critical angle if it is close enough from the surface.

[10] It is named phonon-polariton for waves propagating in a polar material supporting optical phonon modes. The SPhP occurs below the LO frequency where the dielectric function is also becoming negative like for a metal with ω_p.

[11] As mentioned in the general introduction, the samples consists in highly doped InAsSb on GaSb substrate.

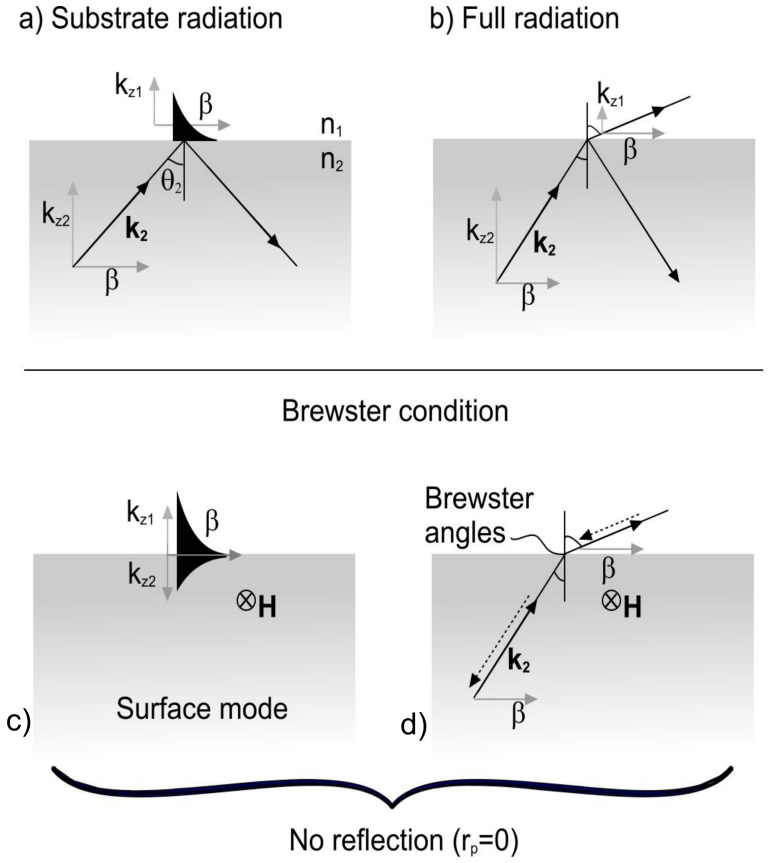

Figure 1.1.4.: Representation of different modes at the interface: (a) Substrate radiation mode, confined in the upper medium only; (b) Full radiation mode, in the case of a plane wave coming from n_2; (c) Fully confined surface mode; (d) Brewster case, represented in the case of two plane waves propagating in one or the other direction.

The situation where the incident beam is below the critical angle is shown in Figure 1.1.4 b). There is no confinement (full radiation mode), it corresponds to a simple refraction of radiation waves.

In the two other cases (Figure 1.1.4, bottom), *there is no reflection*. There are only two waves: one in the substrate and one in the superstrate. For a single interface, the analysis of the Fresnel coefficients r^{TM} and r^{TE} shows that this situation only exists in p (i.e. TM) polarization[12]. The condition $r^{TM}= 0$ for having no reflection is known as *Brewster*

[12] p polarization corresponds to transverse magnetic polarization (TM) where H is perpendicular to the incidence plane.

incidence in the case of propagating waves represented in Figure 1.1.4 d). However, this condition can be satisfied by an evanescent wave as well, since they also obey to the Fresnel's relations. In that case, the surface mode is characterized by two exponential decays (Figure 1.1.4 c)).

In the medium n_1, the Brewster angle θ_B for which $r^{TM}(\theta_B) = 0$ is well-known:

$$\theta_B = \arctan(x) \quad with \ x = \sqrt{\frac{\varepsilon_2}{\varepsilon_1}} \tag{1.1.20}$$

Since $\beta = k_1 \sin(\theta_B) = \sqrt{\varepsilon_1}\frac{\omega}{c}\sin(\theta_B)$, we obtain immediately the dispersion relation $\beta(\omega)$[13]:

$$\beta = \frac{\omega}{c}\sqrt{\varepsilon_s}, \ with \ \varepsilon_s = \frac{\varepsilon_1\varepsilon_2}{\varepsilon_1+\varepsilon_2} \tag{1.1.21}$$

The corresponding dispersion relation $\omega(\beta)$ is shown on Figure 1.1.5, considering $\varepsilon_1 = 1$ (air) for the superstrate and using for ε_2:

- (a) the approximate, lossless expression $\varepsilon_2 = \varepsilon_\infty\left(1 - \frac{1}{\tilde{\omega}^2}\right)$, as in Figure 1.1.5 (left), or
- (b) the complete expression which includes the losses (same figure, right plot).

If dielectric are considered, $\beta(\omega)$ is smaller than $k_1 = \frac{\omega}{c}\sqrt{\varepsilon_1}$ and $k_2 = \frac{\omega}{c}\sqrt{\varepsilon_2}$, because $\varepsilon_s < \varepsilon_1, \varepsilon_2$ for real and positive permittivities. This is the usual radiation Brewster mode, where $\omega(\beta)$ is above the light cone $\omega = ck$. Here, this case is fulfilled for $\omega > \omega_p$, where the material behaves like a dielectric. However, the situation changes drastically if negative permittivity are considered ($\omega < \omega_p$). In that case, the dispersion relation $\omega(\beta)$ will be below the light cone. As can be seen on Equation 1.1.21, if $\varepsilon_2 \to -\varepsilon_1$, then very large β value can be obtained, leading to evanescent waves in both media. The condition $\varepsilon_2 = -\varepsilon_1$ is fulfilled when[14] $\omega = \omega_{SPP} = \frac{\omega_p}{\sqrt{\frac{1}{\varepsilon_\infty}+\varepsilon_1}}$, according to the lossless expression for ε_2.

[13] $\sin(\arctan(x)) = \sqrt{\frac{x^2}{1+x^2}}$

[14] The expression corresponds to $\omega_{SPP} = \omega_p/\sqrt{(2)}$, for a pure plasma ($\varepsilon_\infty = 1$) in air. It is interesting to note that the SPP resonance does not occur at the natural oscillation frequency of the carriers in the bulk comprised between two interfaces, which is ω_p. The natural resonant frequency depends on the geometry, e.g. $\omega_p/\sqrt{(3)}$ for a sphere, and $\omega_p/\sqrt{(2)}$ for a single interface.

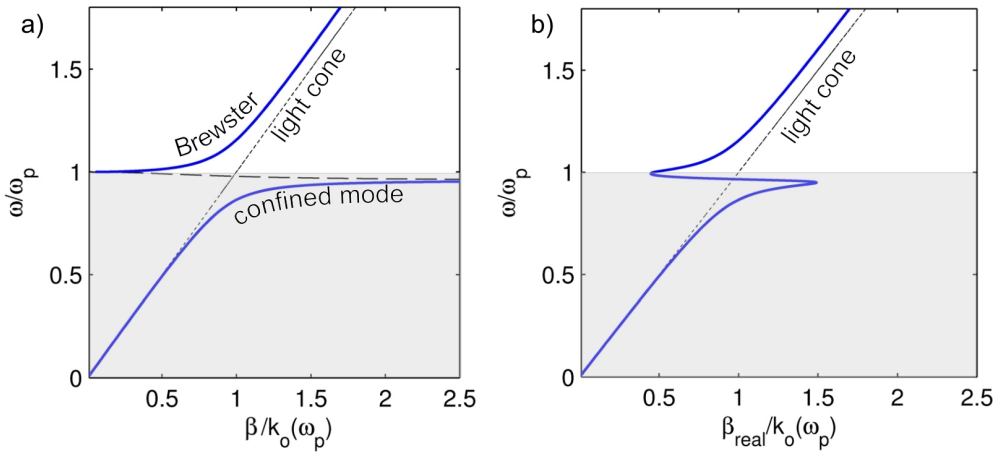

Figure 1.1.5.: Dispersion relation of a SPP in the case of a semi-infinite surface in air, using a lossless Drude model (left) and a lossy one (Equation. 1.1.14). The parameters used for the plotting are $\varepsilon_\infty = 11.7$ and $\tilde{\gamma} \approx 0.03$.

Because of the losses, ε_2 is complex, the maximum value of β corresponding to the strongest vertical confinement is achieved when $|\varepsilon + \varepsilon_2|$ is minimal, i.e. when $|\varepsilon_2 + 1|$ is minimal in our case. This is the resonant condition where the SPP can be optimally excited. However, because of its evanescent nature, this cannot be directly excited by radiation waves even if $\varepsilon_2 \approx -1$, but a point excitation like a scattering nano-probe in the sample near-field will overlap with the surface mode profile and will excite it.

The dispersion relation in the lossless case is:

$$\omega^2 = \omega_p^2/2 + c^2\beta^2 \pm \sqrt{\frac{\omega_p^4}{4} + c^4\beta^4} \tag{1.1.22}$$

We note the existence of gap in the dispersion relation between ω_{SPP} and ω_p. In fact, in this range β is a pure imaginary number, having no propagating character (purely evanescent modes represented by dashed line).

The dispersion relation including losses is shown on the right plot: although β cannot reach the highest value, we still have confined modes. This mode, once excited, can propagate along the surface, and the propagation length L along x is naturally fixed by the imaginary component of the wave vector: $L = 1/\mathrm{Im}(\beta)$. This distance corresponds to an attenuation of the signal intensity of $1/e^2$. An interesting dispersion relation appears

between ω_p and ω_{SPP}, characterized by a negative velocity and a high density of mode as indicated by the shallow slope. These modes are referred to as "quasi-bounded" modes[45]. The Drude parameters taken for this simulation (cf. caption) approximately corresponds to InAsSb ($\varepsilon_\infty = 11.7$) where we can have a plasma wavelength as small as $\lambda_p \approx 5.5$ µm ($\omega_p = 3.4310^{14}\,Hz$) when it is highly doped, with $\gamma_p \approx 10^{13}\,s^{-1}$.

Before discussing the case of the slab, we can illustrate how the radiation pattern of an emitter or a scatterer can be affected in the very near-field of a such semi-infinite polaritonic material, while scanning the infrared frequency of the source. The Figure 1.1.6 shows the calculated radiation of infinitely long gold nano-antenna deposited on a polaritonic material, in the vicinity of the plasma frequency. As can be seen, the radiation pattern strongly change with the dielectric function value of the substrate. In fact, this radiation pattern will also strongly depends on the polarization of the incident field.

More insight regarding the description of radiation pattern will be given in next chapter dedicated to the signal description of SNOM probes that can be regarded as vertical nanoantenna. The angular distribution of the light coming from scattering nano-antenna will be indeed of great importance in the context of near-field optical microscopes used to image and characterize HDSC surfaces to understand and interpret the observed signal, and more specifically its dependence to the sample dielectric function.

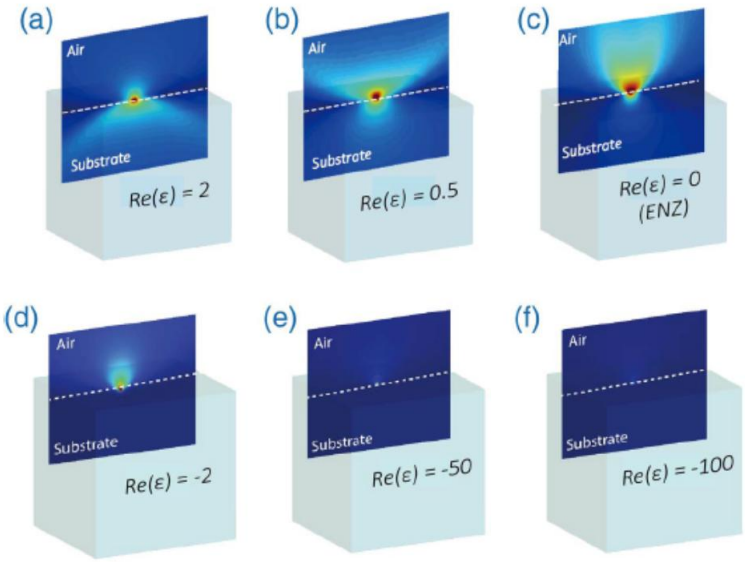

Figure 1.1.6.: Radiation pattern of long gold nanowire on a IR polaritonic material. From[46].

SPP modes in a slab, leaky mode and ENZ confined mode In a slab, the optical constants β of the confined eigenmodes can be determined through a similar procedure, by searching the complex or real β values providing the minimum reflection. Again, the confined eigenmodes are found in TM polarization for polaritonic materials.

For a thick enough slab supported by a substrate, the two modes do not "see" each other (thickness >> skin depth). The eigenmodes dispersion will mostly correspond to 2 independent surface modes, one on each interface. This situation is shown in Figure 1.1.7 blue curve. We note that:

- The SPP confined at the air-HDSC interface occurs as previously when $\varepsilon_{HDSC} \approx -1$ where $\omega = \omega_{SPP}^{sup} = \frac{\omega_p}{\sqrt{\frac{1}{\varepsilon_\infty}+1}}$ which is close to ω_p.
- Similarly, the SPP confined at the substrate-HDSC interface occurs when $\varepsilon_{HDSC} \approx -\varepsilon_{substrate}$ where $\omega = \omega_{SPP}^{inf} = \frac{\omega_p}{\sqrt{\frac{1}{\varepsilon_\infty}+\varepsilon_{substrate}}}$.

However these two modes will couple as the thickness is strongly decreased.

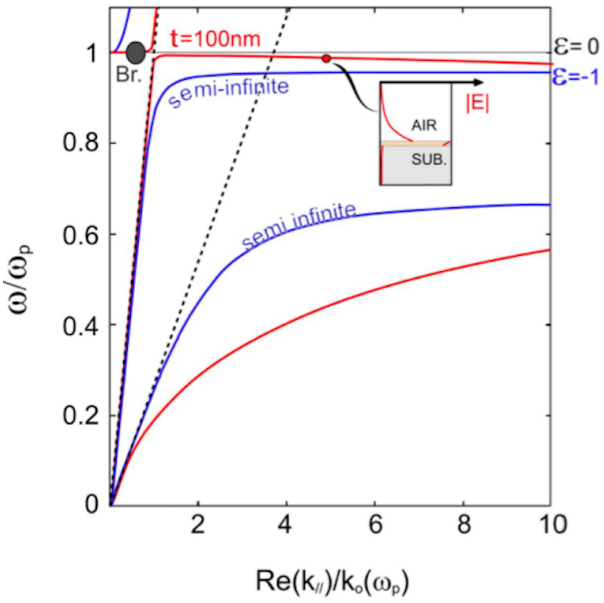

Figure 1.1.7.: Dispersion relation in of the semi-infinite HDSC (blue curve) and finite HDSC (thickness of the slab is 100 nm, red curve) slab (lossless case, $\gamma = 0$). The considered substrate is GaSb, the other parameters are the same as previously.

For the finite HDSC slab, the surface plasmon polariton (SPP) resonance mode is at $\varepsilon = -1$, but this mode can't be excited by farfield. However, if we bring a near field probe, we can have a high spatial frequency of the light (large parallel wave-vector components $k_{//}$), then the SPP mode can be detected by near field reflection coefficient (β) when $\varepsilon = -1$, β tends to be infinite. When ε pass 0 from 1 to -1, the near field reflection coefficient has a large variation, which shows a maximum sensitivity in this region.

In our case, we will deal with HDSC layer of about 100 *nm*, which is shown in Figure 1.1.7 red curve. Because of the small thickness of the slab, we can see that the SPP at substrate-HDSC interface tends to disappear. The SPP at air-HDSC interface tends to shift from $\varepsilon = -1$ to $\varepsilon = 0$, as expected[47]. The near field probe sees the same signal as the semi-finite HDSC slab because the SPP resonance mode of both slabs tends to $\varepsilon = -1$ at very high spatial frequency. When the thickness of the slab is super small, we can observe from the Figure 1.1.8 (c) that the upper confined dispersion curve becomes very flat.

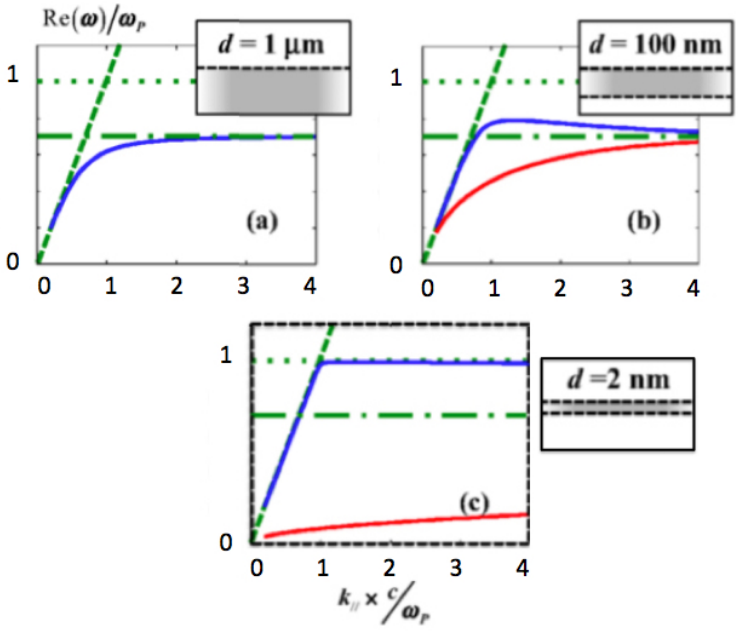

Figure 1.1.8.: Dispersion curves for decreasing thickness d, starting with a symmetric structure (air-plasma-air). As d decreases below the skin depth, the mode split into anti-symmetric (red) and symmetric SPP. The upper dispersion curve becomes very flat even very close from the light cone. The Brewster mode above is not shown but in (c) it would be along the green dot above light cone. Adapted from[48].

From the Figure 1.1.8 we can observe that as the the thickness of the slab decreases, the upper confined dispersion curve shifts toward ω_p (bulk plasma frequency comprised between the two surfaces). The flatness of these curves is particularly pronounced when the thickness of the material slab is small, indicating the presence of a resonant mode (eigenmodes). On the other hand the radiation Brewster mode above the light cone becomes also very flat near ω_p. However because it is above the light cone it is not really confined although resonant and it is slowly leaking out of structure, typically at grazing angle. The characteristics of these two resonant modes near $\varepsilon = 0$ are shortly described hereafter:

- **Brewster (Berreman) leaky mode (BE mode).** While the Brewster condition is in principle always met at normal incidence near $\varepsilon = 0$, the resonant character of the radiation Brewster mode becomes progressively very strong as the thickness decreases. This mode, which is radiating out of the slab, can then be efficiently excited when the

light is impinging with an angle. This mode used to be referred as Berreman (leaky) mode, to describe the same phenomena but in the case of a polaritonic material related to LO phonons rather than electron plasma. Because of its resonant character, absorption peak of the Brewster/Berreman mode can be observed IR far-field spectra (in TM polarization, with an angle) although the absorption in the vicinity of ω_p is small.

- **The ENZ confined mode.** Compared to the Brewster mode, the ENZ cannot be excited by a radiation wave, as it is found below the light cone. This mode requires extremely small thickness to exhibit a flat dispersion curve (e.g. $\lambda_p/50$ or less). Examples of dispersion curves are shown in Figure 1.1.8.

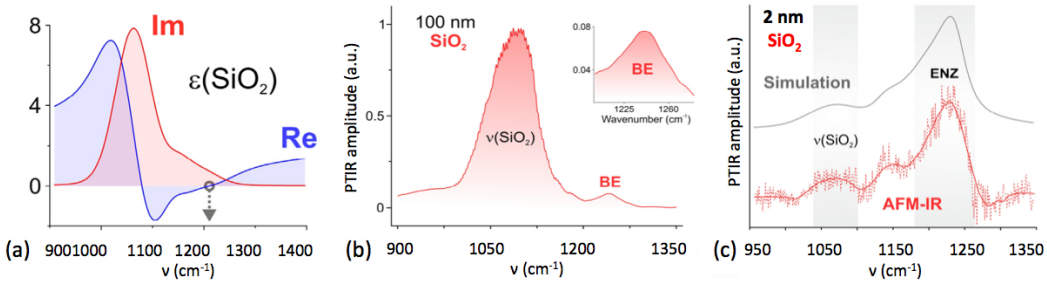

Figure 1.1.9.: Dielectric function and PTIR spectrum of SiO_2 films: (a) Dielectric function of SiO_2 in mid-IR region with marked 1211 cm^{-1} position where Re[ε] = 0 and Im[ε] = 0.73; (b) PTIR spectrum of 100 nm SiO_2 film (BE mode); (c) Simulated absorption (top) and PTIR spectra (bottom) of 2 nm SiO_2 film (ENZ confined mode). Adapted from[49].

These two resonant modes can be distinguished by spectroscopic study according to the article of Shaykhutdinov et al.[49]. They investigated the absorption spectrum of ENZ material with PTIR[15] and simulated the two modes with FDTD (finite- difference time-domain) method on SiO_2 thin films. $\nu(SiO_2)$ corresponds to the maximum of imaginary part of $\varepsilon(SiO_2)$, shown in Figure 1.1.9 (a). The measured BE absorption of 100 nm SiO_2 film is a weaker effect (Figure 1.1.9 (b)) found at 1241 cm^{-1} while measured and simulated

[15]PTIR is Photo-Thermal Induced Resonance. This technique combines AFM with infrared spectroscopy to detect the absorption spectrum due to thermal expansion of the sample. The PTIR spectrum is sensitive to the imaginary permittivity of the material.

peak positions of ENZ local field confinement (Figure 1.1.9 (c)) of 2 nm SiO_2 film is a stronger effect found at 1229 cm^{-1}.

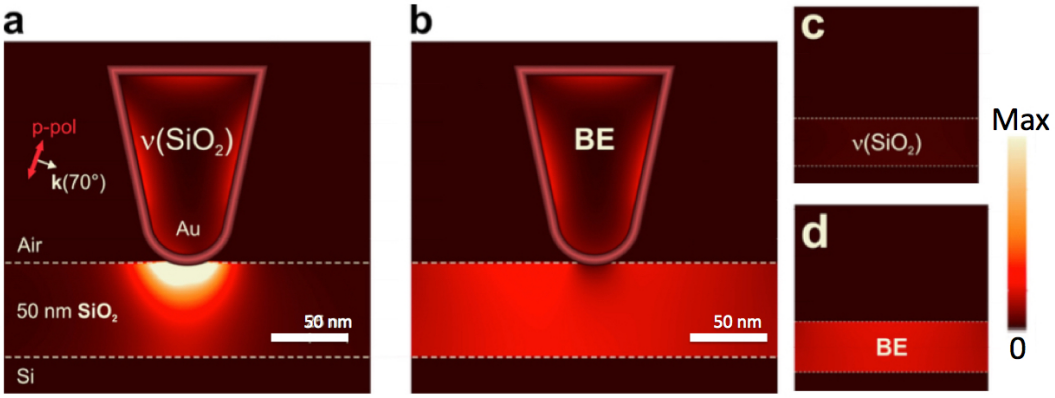

Figure 1.1.10.: Simulation with RSoft: (a) tip induced absorption at $\nu(SiO_2)$; (b) BE absorption in a 50 nm SiO_2 film on Si under p-polarized illumination at 70°; Corresponding simulations without the tip are shown in (c) and (d), respectively. Adapted from[49].

Comparing the simulation with (Figure 1.1.10 (a) and (b)) and without probe (Figure 1.1.10 (c) and (d)), at $\nu(SiO_2)$ a strong plasmonic enhancement is induced by the gold probe while different from ENZ mode, the field distribution at BE mode the field in SiO_2 film is not affected by the probe. The BE mode absorption appears when the dielectric function is close to zero and is associated with a collective oscillation of charges in the thin films[50, 47].

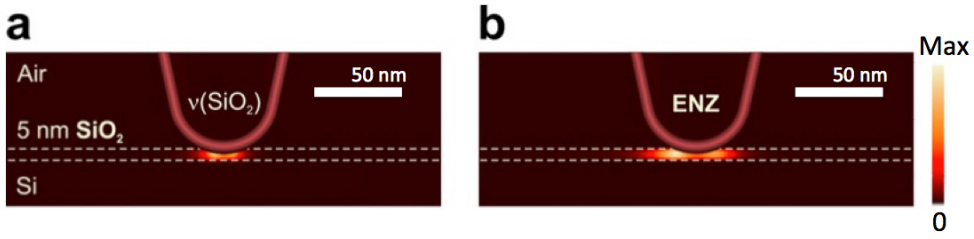

Figure 1.1.11.: Simulation with RSoft: (a) tip induced absorption at $\nu(SiO_2)$; (b) ENZ absorption in a 5 nm SiO_2 film on Si under p-polarized illumination at 70°. Adapted from[49].

ENZ mode is only observed in *ultrathin* films[50]. From Figure 1.1.11 we can see that at both $\nu(SiO_2)$ and ENZ mode, the tip induced enhancement exists and in ENZ mode, plasmon–ENZ coupling and confinement provided by the probe appears in the near field regime and the z component of the electric field is inversely proportional to the thickness of the film[50, 47].

1.1.5. Localized surface resonance (LSPR)

In our work, we are interested in structured HDSC, which has localized resonant mode. When metal "nanoparticles" are excited by light, the SPPs are highly localized at the particle and the near field is enhanced at its resonance ω_{LSPR}. This resonance is highly sensitive to the refractive indexes n surrounding the nanoparticle.

The oscillation frequency of the free carriers depends on the material geometry. For example, for a plasma within a small sphere, the eigenfrequency of the charge oscillation is $\omega_{LSPR} = \frac{\omega_p}{\sqrt{3}}$ (or $\frac{\omega_p}{\sqrt{1+\frac{2}{\varepsilon_\infty}}}$, in presence of a background permittivity ε_∞ within the plasma), where ω_p is still the plasma frequency of the bulk. According to the lossless Drude model, this leads to a resonant polarizability at $\varepsilon = -2$, as expected from the expression of the bare polarizability of a sphere:

$$\alpha = \frac{\varepsilon - 1}{\varepsilon - 2} \tag{1.1.23}$$

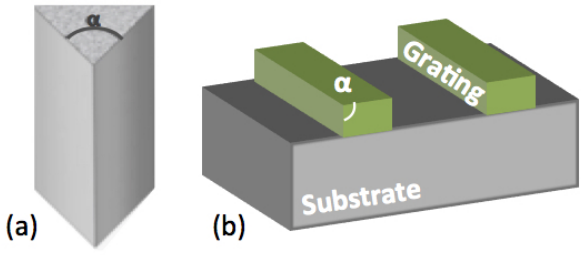

Figure 1.1.12.: Sketch of wedge geometry: (a) wedge geometry with a solid angle α; (b) geometry for grating.

If we consider the geometry of the surface, the surface plasmon wedge frequency ω_s is expressed as $\omega_s = \omega_b\sqrt{\alpha/2\pi}$ where ω_b is the bulk plasma frequency and α is the wedge solid angle (shown in Figure 1.1.12 (a)) and the real permittivity at LSPR[51] is:

$$Re(\varepsilon) = 1 - 2\pi/\alpha \tag{1.1.24}$$

In our case (c.f. Figure 1.1.12 (b)), the wedge is 90° ($\alpha = \pi/2$), the plasmon wedge frequency ω_s equals to $\omega_b/2$ and $Re(\varepsilon)$ is -3.

The interest in investigating HDSC sample is the potential substrate in surface-enhanced infrared absorption spectroscopy (SEIRA), which is used to identify molecules and can be applied for biosensors. As a mid-IR LSPR sample, the IR field would be enhanced in the proximity of the structure, and when molecules are attached on the SEIRA substrate, the molecular absorption of IR light increases due to coupling with plasmonic resonators.

1.2. Potential materials for IR plasmonics

Incident light is strongly confined and enhanced by plasmonic nanostructures that have an electromagnetic coupling with the surrounding material, which makes IR plasmonics to be a hot topic for years. Gold and silver are well-known materials for plasmonic because these two noble metals have low rate of scattering of free electrons in them, which leads to high conductivity in the radio frequency range and high reflectivity in the optical range[52]. Their plasma frequency lies in ultraviolet and they have a small negative real dielectric function at visible wavelength, which allows to excite plasmon from visible light. Moreover, gold and silver have lower imaginary part of dielectric function compared with other metals, which means less ohmic losses[53]. By changing the shape of the gold or silver nanoparticle, or changing the surrounding dielectric matrix, the plasmonic resonance can reach near-infrared region of the spectrum[54, 55, 56]. However, extending this resonance into infrared wavelength becomes challenging because of several issues. The plasma frequency of metals is fixed, which limits the tunability of their optical properties. Moreover, in IR range, gold and silver have large value of negative real permittivity[57] behaving like perfect conductor whose optical response is described as antenna resonance rather than as

plasmonic effect[37]. The carrier density in metals is high and the electron-electron scattering causes losses: their imaginary permittivity is high, which results in large ohmic losses. This large negative real part and losses are not desired in IR plasmonic devices design.

Besides, noble metals are expensive and the fabrication technique of gold and silver does not follow the standard silicon nanofabrication technology, which makes it difficult for plasmonic on-chip integrated devices[38].

According to the standard conductivity description, the Fermi level shifts and electrical current flows when an external field is applied to the material. While at relatively low frequencies, the states close to the Fermi level will participate in conduction and the absorption is determined entirely by the density of states (DOS) and scattering strength near the Fermi level. The scattering is related to lattice vibrations, surface imperfections, impurities, or additional electrons excited from below the Fermi level. The scattering strength, which is the strength of the interaction between electrons, phonons, and impurities, does not change obviously at different interband energy and in different materials, but the density of states vary at different energy level, shown in Figure 1.2.1. In metals the DOS is large and Fermi level is high in the conduction band (shown in Figure 1.2.1 (a)), while in highly doped semiconductors, because of a relatively low density of carriers, the Fermi level is very low and the DOS available for scattering is much smaller than in metals (shown in Figure 1.2.1 (b)). This allows highly doped semiconductors to have small absorption losses in IR range.

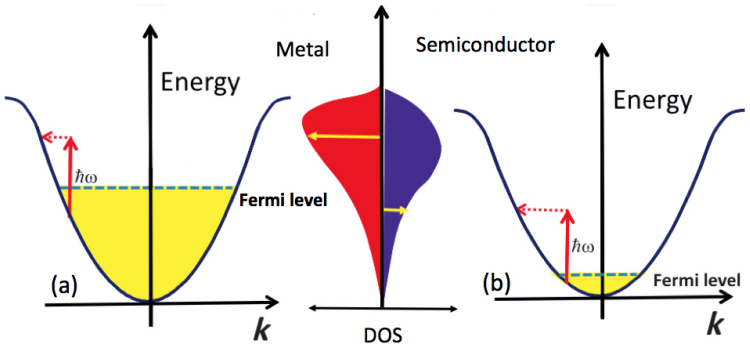

Figure 1.2.1.: Band diagram and density of states of (a) metal and (b) highly doped semiconductor. Lower density of states in the semiconductor is responsible for the reduced loss. Figure adapted from[38].

Although losses cannot be avoided, there are still three main approaches to minimize the effects of losses[38, 52, 58]:

- Engineering the shape and size of plasmonic structures to reduce penetration of electromagnetic wave in metal;
- Combining gain medium to compensate losses;
- Considering alternative plasmonic materials other than noble metals.

The first approach is necessary for subwavelength confinement to store energy[52]. In reality, even the highest gain provided by existing active materials is not enough to compensate the large losses[58, 59]. To explore alternative plasmonic materials seems to be a better option.

Besides losses, the real part of dielectric function ε' is another essential factor to be considered for plasmonic material because it determines the optical performance. As is introduced in the literature of Law et al.[57]: *"at wavelengths where the real part of the permittivity is small and negative, both SPP and LSPR excitations can be confined to length scales much smaller than the wavelength of light. It is this subwavelength volume of the plasmonic modes which makes them so attractive for both nanophotonic (subwavelength waveguides and laser cavities) and sensing (strengthened interaction with molecules by means of field localization and enhancement) applications."* In Figure 1.2.2, the potential materials are classified of two factors:

1. Carrier concentration. The carrier concentration has to be high enough to provide a negative ε' and ideally should be tunable;
2. Carrier mobility. Lower carrier mobilities means higher material losses.

In addition, a third axis corresponding to the undesirable "interband losses" is also added. So, the ideal material for plasmonics would lie at the left end of the plot on the horizontal plane where interband losses are zero[58]. Although such a perfect material never exist, there are still many potential candidates, such as doped semiconductors, transparent conducting oxides (TCOs), graphene, etc. We are interested in mid-IR range in our work, we

can see from Figure 1.2.2 that III-V semiconductors like InAsSb are an excellent choice with high mobility and low losses (cf. caption for details).

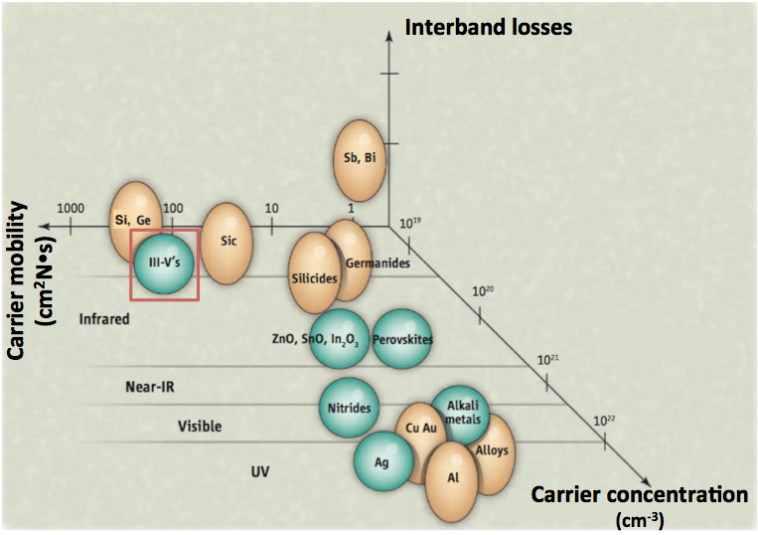

Figure 1.2.2.: Plasmonic material ordered by carrier concentration, mobility and interband losses. In this 3D space, the blue spheres represent materials with low interband losses, and the red ellipsoids are for materials with larger interband losses, which depends strongly on the electromagnetic spectrum range. Figure adapted from[58, 38].

1.2.1. Silicon and Germanium

For doped semiconductor, the accessible spectral range is limited by the maximum doping level and the frequency corresponding to the bandgap should be considered to avoid interband transition. The frequency of the bandgap should be higher than the frequency where plasmonic behavior occurs. Silicon and germanium are the standard materials of semiconductors in plasmonic applications and the technique of their fabrication and processing is well studied. Doped Si[60, 61, 62, 63] and doped Ge[64, 65, 66] have been used for plasmonics in IR. Compared with Si, Ge has higher electron mobility[67] and smaller optical bandgap while the dopant solubility of Ge is smaller than that of silicon[68] and the background permittivity of Ge is higher, which means that for a given wavelength, higher doping in Ge is needed. Both Si and Ge would need very high doping to perform plasmonic

behavior at the telecommunication wavelength[53], while both materials are limited by the solid-solubility. But they are commonly used for plasmonics in mid-IR range.

1.2.2. III-V semiconductor

Since III-V HDSC have been used in this thesis, this category of plasmonics material will be here described in more details. The material were made in the Nanomir group of T. Taliercio, in IES at Montpellier, which has demonstrated interesting LSPR in the mid-IR for SEIRA applications.

III-V semiconductors, such as InAs, GaAs, InP and GaN, offer potential for plasmonics in the infrared spectral range and their applications have been investigated and can be found in many articles[69, 70, 71]. These materials exhibit a wide tunability in the optical bandgap that can be controlled[72]. For GaAs and InP, their optical bandgap and background permittivity are comparable to that of silicon[73]. For instance, silicon is a common dopant in GaAs. For n-doping GaAs, the carrier concentration would saturate when donor density is higher than $5{\times}10^{18}\,cm^{-3}$[74, 75]. On the other hand, p-doping with Be or C can be used to achieve carrier concentrations higher than $10^{20}\,cm^{-3}$ while holes have a higher effective mass and poor carrier mobility[76].

The first InAs/GaSb system is proposed for plasmonics in 2011 and InAs can reach the smallest plasma wavelength among common semiconductors, with a very high carrier incorporation[77]. InAs can be doped higher than n-GaAs and Law et al.[37] have demonstrated the LSPR behavior in subwavelength disks of heavily doped InAs at a wavelength of 9 μm. InAs is a semiconductor with a low band gap $0.35\,eV$ and low effective mass $m^* = 0.026m_0$[78]. InAs can easily be doped n-type up to a few $10^{20}\,cm^{-3}$[79]. Thanks to its high electron mobility and its low effective mass, InAs is very often used in infrared optoelectronics, for example for the manufacture of lasers.

Regarding the supporting substrate choice (GaSb), it should noted that the conduction band offset between InAs and GaSb is large (1 eV), which avoids charge transfer from InAs to GaSb layer when InAs is heavily doped because there is no carrier leakage until the Fermi level of InAs reaching the edge of the GaSb conduction band[80]. The lattice constant of

InAs is 6.0584$\mathring{A}$ which is close to that of GaSb ($a_{GaSb} = 6.0954\mathring{A}$) and incorporating 9% Sb with InAs allows lattice matching to GaSb[78, 32].

Several metamaterial and plasmonic devices have been demonstrated using these materials in mid-IR. For example, a system of planar, alternating layers of heavily doped InGaAs and undoped AlInAs can be used for negative reflection as a hyperbolic metamaterial[81][16].

Furthermore, highly doped InAsSb, near ω_p, has naturally epsilon-near-zero properties in mid-IR range which can be used for designing specific plasmonic behavior[82]. These semiconductors are also used for electric field-effect tuning of the characteristics of THz and Mid-IR photonic devices[83, 84]. If they are heavily doped and used as plasmonic components, the tunability could be much higher.

Up to now, except for nitrides, III–V compounds have been widely studied for plasmonic applications in the MIR and longer wavelengths. Obtaining plasmonic properties at shorter wavelength like telecommunication wavelengths requires a carrier concentration over $10^{20}\,cm^{-3}$, which is very challenging due to the limit of the solid solubilities of the dopants. In this context, III-Nitrides semiconductors are still a promising low-loss alternative plasmonic material for NIR. For example, GaN has a direct bandgap of about 3.3 eV and the wide bandgap reduces the minimum carrier concentration required to achieve metallic properties at a given wavelength. With slightly higher doping, GaN could be turned plasmonic at NIR telecommunication wavelengths[85, 86].

Epsilon-Near-Zero (ENZ) material

Doped semiconductor have a real permittivity value changing sign near the plasma frequency while keeping a relatively small imaginary permittivity. Such materials, where the relative permittivity ε approach near-zero values around a given frequency, are called Epsilon-Near-Zero (ENZ) material[40] and are particularly investigated in the context of metamaterials[87, 88]. Many plasmonic materials may behave as ENZ materials near their plasmas frequencies and are in fact already used in semiconductor industry (ITO, InSb).

[16] Hyperbolic metamaterial is an extremely anisotropic material. When light polarization passes in one axis of the material, it behaves as metal while when light polarization comes from the perpendicular axis it turns to dielectric.

More generally, the ENZ condition can be fulfilled in polaritonic materials near ω_p or ω_{LO} (longitudinal phonon resonance).

Liberal and Engheta[89] summarize the principles, unique features and technological potential of ENZ materials. The tunneling effect[89] of the ENZ material makes it possible to be a supercoupling between two waveguide[87, 90]. Another potential is that it can be used to design zero-index media (ZIM), which has both ε and μ near zero at the needed frequency[91, 92]. Moreover, the directivity enhancement of ENZ allows it to be used in the system that is able to control the direction of emission of a source[93, 89] or the to manipulate the phase fronts of sources in order to obtain anomalous imaging, lensing and radiative effects[94]. This aspect will be detailed further, when we will detail the signal provided by a scattering probe in the sample near-field in the next chapter.

Alù et al.[95] also demonstrated that this material can cancel the scattering from dielectric or conducting objects so that it may be used as a good cover.

As mentioned ENZ materials are attracting a lot of interest in recent years in the context of metamaterials due to the peculiar wave features in such medium. Notably, the large wavelength stretching occurring in ENZ materials entails a strongly reduced phase radiation that can be advantageously used for the design of antenna in the IR or THz range. While the characteristics of emitters or antenna on ENZ substrates have been already investigated in several recent papers[96, 97, 98], more attention can be explicitly paid to vertical polarizable antennas in the immediate vicinity of an ENZ surface. In fact, this situation is readily achieved in near-field nanoscopy experiments using conventional scattering nanoprobes that can be put in close interaction with ENZ materials for spectroscopic imaging purpose[49].

1.2.3. Transparent Conducting Oxides

Oxide semiconductors such as zinc oxide, cadmium oxide and indium oxide can be highly doped to make them conducting films. These semiconductors, known as transparent conducting oxides (TCOs), are transparent in the visible range because they have a large bandgap. Highly doped TCOs have metal-like optical properties in the NIR range and they show high DC conductivity. The optical properties of TCOs can be tuned by changing

the doping level as other semiconductors. They are good candidates for NIR plasmonics because they can be patterned by standard fabrication procedures and grown into thin films and many different nanostructures can be achieved.

The generally acknowledged TCOs are aluminum-doped ZnO (AZO), gallium-doped ZnO (GZO) and indium tin oxide (ITO). Among these 3 materials, AZO has the lowest losses while GZO and ITO can have much higher carrier concentration.

Several achievements obtained with these materials in the field of plasmonic IR can be briefly mentioned. Rhodes et al.[99] observed surface plasmon resonance (SPR) on ITO thin films deposited on a prism. This system was able to support SPPs when infrared light was incident in the Kretschmann geometry . Mishra et al.[100] reported an SPR-based, ITO-coated fiber optic hydrogen gas sensor. Naik et al.[101] have also experimentally demonstrated negative refraction in AZO/ZnO. Garcia et al.[102] presented a tunable LSPR in ITO nanoparticles and the tunablility was achieved by varying the carrier concentration or by doping electrochemically.

1.2.4. 2D Plasmonic Materials

2D materials are crystalline materials consisting of a single layer of atoms, also referred to as single layer materials. Graphene was the first 2D material to be discovered and after the demonstration of plasmons in graphene, plasmonics with 2D materials has gained a lot of attention[103, 104, 105]. As a 2D material, the SPP in doped Graphene can hardly be described by a metal-like permittivity (Drude), which requires to define an effective thickness, but rather by its surface conductivity.

The most important advantages of Graphene are notably a high electric field confinement together with a weak damping[106] and the possibility to electrostatically tune its plasma frequency simply by applying a voltage. The nanostructured graphene has been demonstrated to work as a high-sensitivity tunable plasmonic biosensor because of its unique electro-optical properties[107]. The prospects for applications of graphene is broad, such as electro-optical modulation, optical sensing, quantum plasmonics, light harvesting, spectral photometry, and tunable lighting at the nanoscale. More details of graphene plasmonics are given by Low et al.[108]and its opportunities and challenges can be found in the article

of F. Javier[105]. However, it should be noted, that challenges remain for graphene plasmonic since the substrate typically strongly affect its characteristics, requiring very specific supporting material to keep sufficient propagation length.

However, graphene is not the only interesting material and other 2D materials are emerging, in combination with graphene or independently. For example, another 2D plasmonic material, black phosphorus (BP) has also been investigated[109]. In the mentioned article, localized surface plasmons modes have been numerically demonstrated in monolayer BP using nanoribbon and nanopatch arrays and its anisotropic properties make it possible to be designed as a polarization sensor. Other challenges exist for these new 2D materials like BP, notably regarding the methods to obtain large scale monolayer BP films.

1.3. Conclusion

To conclude, dielectric function and Drude model was presented and the formulas are listed to help understand well the permittivity of doped semiconductor and many other materials consisting conduction electrons. The dielectric function plays an important role in the light-matter interaction that is the principle of many characterization techniques. Reflectivity modeling of HSDC were presented based on Drude model and SPP and LSPR mode were introduced briefly to give an overview of the concept appeared in this thesis. Standard analytical technique FTIR was presented in this section and simulations of reflectance of high loss and ultra small object are shown. Both field distribution affected by probe near the film surface of Brewster/BE mode and ENZ mode were described by simulations.

Then several potentials IR plasmonic materials were introduced because noble metals have some limitations in IR range. Considering the losses and plasmonic properties, there are still many choices and we highlight some of it. III-V semiconductors are good choice for mid-IR plasmonics with low losses and among them, our interest is InAs which has been investigated by many researchers and fruitful information can be found in literatures. ENZ material was briefly presented because near plasmas frequencies, the permittivity of plasmonic materials approaches zero, which allows them to have unique properties and varied applications. The fundamental aspects of the two near field techniques used in our investigation are presented in the following two chapters.

2. Fundamental aspects of s-SNOM

Contents

2.1 A short historical overview **36**

2.2 Different types of SNOM **37**

2.2.1 Aperture SNOM (a-SNOM) 38

2.2.2 s-SNOM 39

2.2.3 Hybrid-probe SNOM 41

2.2.4 Probe choice 42

2.3 Analytic models of probe-sample interaction in s-SNOM **42**

2.3.1 Dipole approximation 43

2.3.2 Flaws and improvement of the Dipole model 50

2.4 Conclusion **54**

To study the interaction between light and nanometer-scale objects, microscopy with resolution beyond the diffraction limit coupled with spectroscopic techniques are becoming indispensable. As light interacts with minute structures, the evanescent waves produced at the boundaries of materials decay exponentially over a distance that is almost independent from the wavelength. Because of this localization, the evanescent waves can provide a very high spatial resolution. Scanning near-field optical microscope (SNOM) is a relatively well established, non destructive, experimental technique used for direct mapping of the evanescent fields confined in the near-field of a sample. Such tool is the first nanoscopic method used to investigate the response of the HDSC materials, as it will be described in the experimental part. In this chapter, we present the basics of s-SNOM. First we provide a short historical background of SNOM and its development. After this general introduction

to the technique, we describe the probe-sample interaction using analytical, quasi-static, approximations and taking into account a side illumination, as it will be the case in our mid-IR SNOM experiments.

2.1. A short historical overview

When light is scattered by a structure, we can coarsely define three important regions between the object and a remote observation plane: the Fraunhofer or far-field diffraction zone, the intermediate Fresnel zone, and the near field zone (shown in Figure 2.1.1).

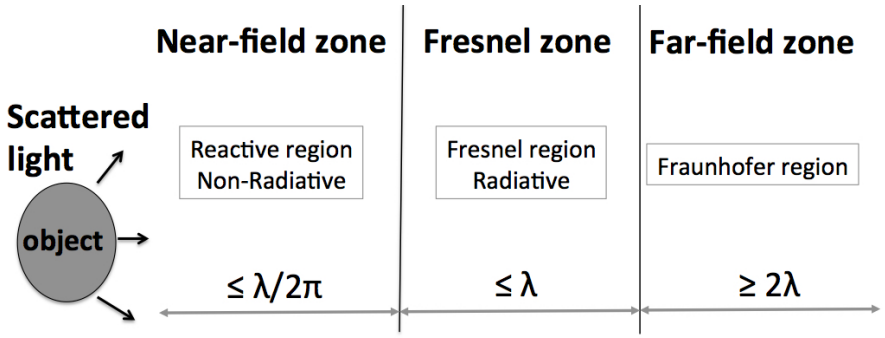

Figure 2.1.1.: Schematic of electromagnetic field regions scattered by an object.

Classical optical microscopy works in the far field region, and therefore cannot have directly access to the high spatial frequencies carried by the evanescent waves in the near-field region. The spatial resolution limit is known as the Abbe diffraction limit[110], which is also accounted for by the Fraunhofer diffraction pattern of small aperture. To break this limit and bring optical microscopy to a higher resolution, Edward Hutchinson Synge proposed the idea of exciting and collecting diffraction in the near field in 1928[111]. His original idea was based on the use of a tiny hole of about 100 nm positioned after the light source, maintained at a distance smaller than 100 nm from the surface. Following this idea, a subwavelength mapping could be achieved by point-by-point scanning. Later on, John A. O'Keefe developed similar theories in 1956. However, the nano-source and detector positioning were impassable technological barriers at that time and the brilliant idea remained unproven for decades[112].

In 1972, Ash and Nicholls first broke the Abbe's diffraction limit using radiation with wavelength of 3 cm[113]. Finally, a decade later, thanks to the use of piezoelectric crystals, STM (scanning tunneling microscope) and AFM (atomic force microscope) were invented by Gerd Binning and Heinrich Rohrer in 1981. Almost at the same time, a patent on an optical near field microscope using a sub-wavelength aperture was filed by D. Pohl[114], followed in 1984 by the first paper demonstrating the use of visible radiation for near field scanning[115]. Lewis et al. were also aware of the potential of a near field optical microscope at this time[116]. They reported first results in 1986 confirming super-resolution[117, 118].

Instead of using a small aperture, the idea of using a particle or a tip in near field microscopy was proposed by Wessel[119] and first realized by Specht et al.[120]. In 1994, Inouye and Kawata first reported a near field microscope by scattering light directly at a metal tip placed close to a sample surface[121]. Only a couple of months later, Zenhausern et al. showed a similar technique with a reported resolution of 3 nm[122] and one year later the resolution achieved to 10 angstrom[15]. Later in 1996, first s-SNOM measurement performed at mid-IR wavelength (10.6 μm) with a resolution of 17 nm shows clearly that the resolution does not depend on the wavelength but mostly on the radius of the tip apex[123]. In the same period, underestimated difficulties in the result interpretation were also pointed out[124], considering the possible crosstalk between topographical and optical information. Nowadays, scanning near field microscopy has become much more mature, and is a demanded characterization technique for research with companies manufacturing commercial SNOM[125, 126, 127, 128].

2.2. Different types of SNOM

In the short historical overview, two types of SNOM were mentioned. The basic distinction between them is the nature of the probe used as local illuminators or collectors. These probes are typically categorized in two broad families: the sub-wavelength aperture probes and the scattering type probes. During this work, only scattering probes also named apertureless probes were used. The specificity of this approach is briefly introduced here.

2.2.1. Aperture SNOM (a-SNOM)

In a-SNOM, a small aperture probe, which is typically based on tapered optical fibers with or without metal coating, is placed close to a sample surface (cf. Figure 2.2.1). Figure 2.2.1 (d) shows an aperture probe with metal coating which manufactured with the help of a Focused Ion Beam[129]. Nowadays, a-SNOM has become a more popular instrument which is commercially available. The different operation modes of a-SNOM are sketched in Figures 2.2.1(a-c).

For illumination mode (Figure 2.2.1 (a)), light is transmitted through the fiber and the extremity of the fiber works as a nano-source, while the light coming from the sample is collected by far-field optical elements[130, 131]. Conversely, for detection mode, the sample is illuminated through far-field optical elements while the near field is detected by a fiber as illustrated in Figure 2.2.1 (b)[132]. Finally, a simultaneous illumination and collection mode (Figure 2.2.1 (c)) is realized by using the same probe to illuminate and collect the signal back-scattered in the aperture [133].

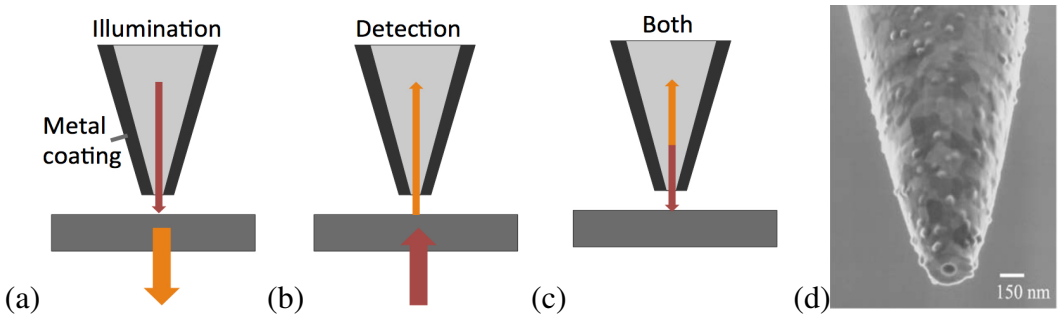

Figure 2.2.1.: Operation mode of a-SNOM: (a) illumination mode; (b) detection mode; (c) illumination and detection mode; (d) SEM image of a-SNOM probe. Adapted from[129].

The main advantage of a-SNOM is the small *background field*[1] because of the local illumination, which makes the aperture probes highly suitable for imaging complex objects like biological samples. However, the resolution of a-SNOM is critically limited by

[1] A problem inherent to the SNOM technique in general is that the contributions coming from sources different from the tip apex can be collected. The origin of these sources can be, for example, scattering dusts, roughness, optical losses (in waveguide structures) . In addition, the body of the probe itself can radiate or scattered some light that can be detected. All these unwanted contributions are usually referred as “background light”.

the diameter of the aperture. Additionally, a-SNOM struggles with low signal efficiency when apertures are made smaller[134]. Suggestions were made to alleviate this problem by designing special shaped nano-aperture, such as bowtie-antenna-shaped apertures[135] or C-shaped apertures[136]. Moreover careful cutting of the fiber probe may result in extraordinary transmission offering an improved coupling through the aperture[137], and specific aperture shapes offer a way to detect more selectively a field component.

2.2.2. s-SNOM

Apertureless SNOM, or scattering-type SNOM (s-SNOM) was first introduced in 1994[122, 121, 123, 138]. A scattering tip, usually an AFM tip, is placed close to the sample surface and the light scattered by this probe contains information of the near field interaction with the sample. Often, this technique takes advantage of the fact that the near field signal depends on the local dielectric constant, so that a contrast arises between regions of different optical properties. Three illumination modes are illustrated in Figure 2.2.2. The side illumination (Figure 2.2.2 (a)) and top illumination (Figure 2.2.2 (b)) correspond to a reflection backscattering mode while the bottom illumination (Figure 2.2.2 (c)) can be used in transmission mode. The transmission illumination type is recommended for thin transparent samples and it can be compatible with the use of a high numerical aperture objective lens which reduces background light influence[139].

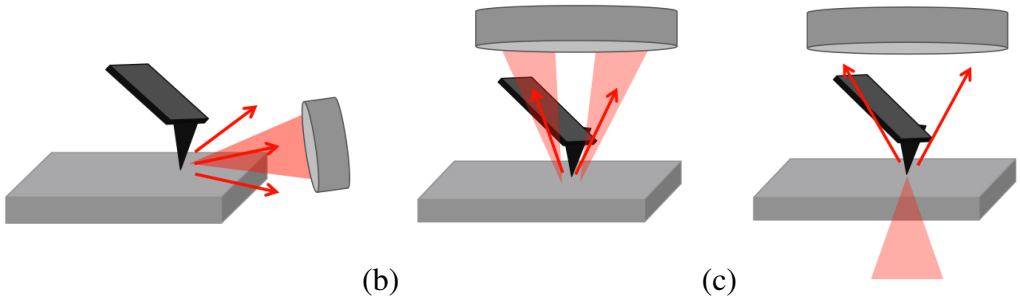

(a) (b) (c)

Figure 2.2.2.: Illumination of s-SNOM: (a) side illumination; (b) top illumination; (c) bottom illumination.

S-SNOM is based on a scanning probe microscope[35, 140, 141], either an atomic force microscope (AFM)[142]or a scanning tunneling microscope (STM)[119]. This type of

SNOM is considered as more robust and because of the probe sharpness, it provides good topographic and optical resolution. Since the resolution of SNOM depends on the diameter of the probe, we tend to use probes with very small diameters. However using a small probe may also mean small scattered signal. Although the most used tips are the commercial Si and silicon nitride tips, metal coated dielectric tips[143] and metallic tips are used by many groups in order to enhance the scattered signal.

With a mid-IR s-SNOM with side illumination, Hillenbrand et al.[35] observed a contrast reverse between Au and SiC at 978 cm^{-1}, the phonon resonance of SiC ($\varepsilon_{SiC} \approx 0$). From Figure 2.2.3, we can see that when the wavelength of the incident light changed, the signal on SiC changed while there is no signal change on Au. The s-SNOM signal is very sensitive near phonon resonance. We assume that the contrast reverse phenomenon would be observed in our experiment with HDSC samples near the plasma frequency.

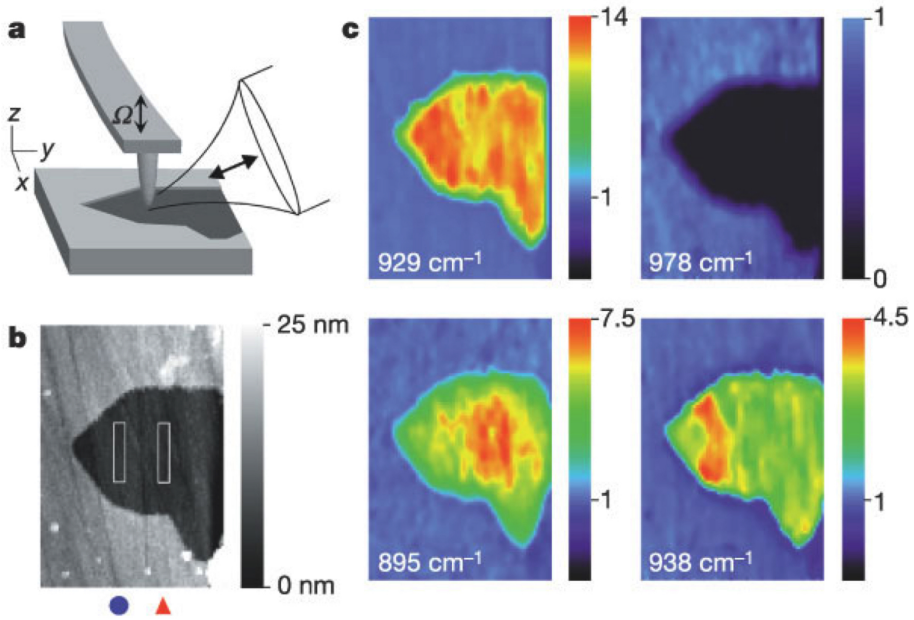

Figure 2.2.3.: Mid-IR s-SNOM investigation of a polar material SiC in vicinity of phonon resonance: (a) experimental scheme of mid-IR s-SNOM; (b) topography of partly Au-covered SiC sample (image size 1.6 $\mu m \times 2.3\,\mu m$); (c) the near-field amplitude images taken at different wavelengths. From[35].

One of the major drawbacks of s-SNOM is the background signal which is scattered by the sample itself or the probe body, as shortly mentioned before. Since the field scattered

by the apertureless probe is collected in the far-field, the near field signal is often buried in a large background coming from the whole detection spot. In order to solve this issue, the tapping mode is commonly used for the scan so that the useful scattered signal is modulated at the tip frequency. Such approach is necessary but not sufficient to suppress efficiently the background. To suppress the background signal from the probe body, the collected signal is demodulated at higher harmonic frequencies of the probe[144, 145]. However, this technique loses part of the useful signal while low signal is always an issue for SNOM. For the purpose of enhancing the near field signal, specific interferometric techniques can be implemented to filter out the background light strongly as well as distinguishing the amplitude and phase of the complex near field signal.

In our setup, we use the side illumination with the backward-scattered light collection, where the alignment requires a fine focus adjustment. Tungsten tips fabricated by electrochemical etching are used to provide good electric field enhancement in the mid-IR as well as mechanical hardness. An interferometric detection method, generalized lock-in amplifier detection (GLIA)[146] is implemented in our work, which provides phase and amplitude information. More details of our setup are given in chapter 4.

2.2.3. Hybrid-probe SNOM

To complete this introduction, we can also mention the existence of hybrid probes, proposed in order to combine the advantages of a-SNOM and s-SNOM[147, 148]. This idea came for the sake of benefiting from the almost background-free a-SNOM and having the topographic and optical resolution of s-SNOM. Simply speaking, hybrid probe is to add a scatterer at the apex of an aperture probe. An example of hybrid-probe developed at the University of Troyes[149] is shown in Figure 2.2.4. In this approach, a carbon nano-probe is positioned next to the edge of the aperture of a standard aperture probe. This antenna improves the topography as well as the scattering efficiency.

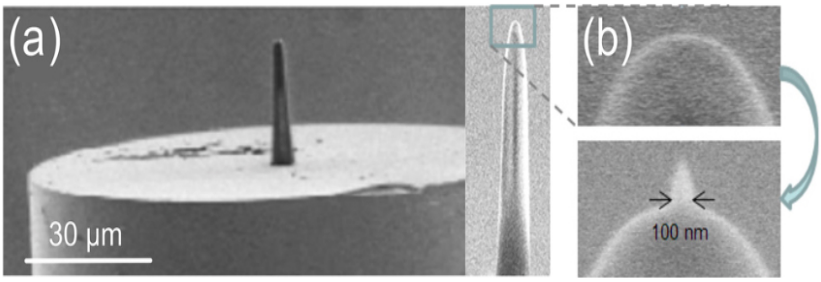

Figure 2.2.4.: Hybrid-probe: (a) Example of polymer-tipped optical fiber; (b) SEM images of the probe apex without and with a carbon nano-probe. From[149].

2.2.4. Probe choice

The aperture probe can hardly be considered for infrared nanoscopy as the optical fibers present huge absorption losses in the mid-IR. The aperture probe material will restrain the spectral bandwidth and should be probably avoided for broadband spectroscopy imaging. For mid-IR near field study, we use apertureless tungsten (W) probe glued on a tuning fork. Tungsten is a hard metal and with electrochemical etching, we can obtain sharp tungsten probes with a diameter smaller than 30 nm. Detailed fabrication procedure is presented in chapter 4. Moreover, tungsten is much cheaper than gold. However, W is easy to be oxidized so that freshly prepared probes are preferred in the measurement.

2.3. Analytic models of probe-sample interaction in s-SNOM

The s-SNOM characterization technique is able to transfer information on the investigated sample from near-field to far field. In most of the experiments performed in the mid-infrared region, the s-SNOM is operating in reflection, with a side-illumination from a mirror objective and the backward scattering is collected using the same mirror objective lens. Many electromagnetic methods have been used to account for the experimental signal. Among these methods, analytic models based on dipole approximation are found to

be very instructive to understand the probe–sample interaction occurring in a s-SNOM experiment. The advantage of these phenomenological methods is that they provide a simple expression for the s-SNOM signal that can predict the signal variation as a function of sample's permittivity under the probe apex. In this subsection, we present an analytical model based on dipole approximation and its extension consisting in a rigorous electromagnetic approach based on volume integral method involving dyadic Green functions. Most of this part follows derivations presented in more details in the PhD work of Z. Sedaghat[149]. Here, the most important steps and results are summarized to serve as a basis to understand the experimental results as well as to better understand the possible expressions for the PiFM signal (next chapter).

2.3.1. Dipole approximation

In this model, we consider the scattering probe as a small polarizable sphere and the sample is large compared to the probe as to be regarded as semi-infinite. The probe sample system shown in Figure 2.3.1. The incident electric field induces a dipole in the probe and another image dipole is induced in the sample creating a coupled system. The electromagnetic radiation of the dipole in the vicinity of the sample is then observed in the far field zone. To describe this system, we start by expressing the field of a single oscillating dipole in free space using the corresponding dyadic Green function notation.

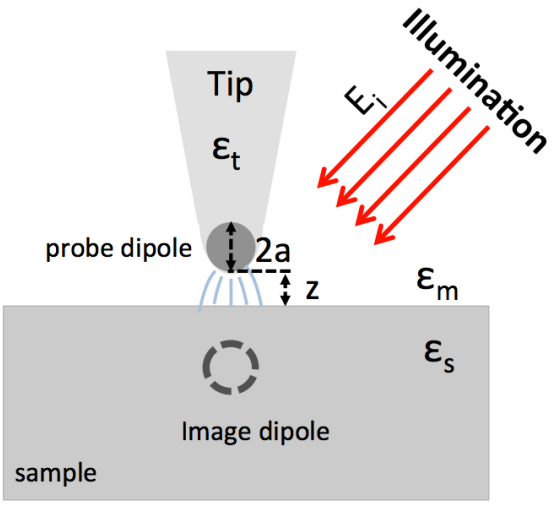

Figure 2.3.1.: Model of probe-sample interaction and dipole image theory. ε_t, ε_m and ε_s are the permittivity of tip, surrounding medium and sample respectively. z is the distance between sample and probe and a is the tip apex radius.

Dipole near a surface

We consider an electromagnetic dipole $\mathbf{p} = pe^{i\omega t}u_p$ oscillating at a frequency of ω in a homogeneous medium ε_m. The complex field radiated at observation point is[150]:

$$\mathbf{E}(r) = K(r)\left\{\frac{k^2}{r}(u_r \times p)\times u_r - \frac{ik}{r^2}[3u_r(u_r\cdot p)-p] + \frac{1}{r^3}[3u_r(u_r\cdot p)-p]\right\} = S(r_2,r_1)p \quad (2.3.1)$$

where $K(r) = K_c e^{ikr}$ and k ($k = \sqrt{\varepsilon_m}k_0$) is the wave vector in the medium. From Equation 2.3.1, we can see that the Green dyadic $S(r_2,r_1)$ that links $\mathbf{E}$ and p has three contribution terms:

$$S(r_2,r_1) = S^{ff} + S^{if} + S^{nf} \quad (2.3.2)$$

corresponding to the three zones described before (see in Figure 2.1.1). $k \to k_o$ when the surrounding medium is air ($\varepsilon_m = 1$), then the three Green dyadic terms are:

- $S^{ff} = K(r)\frac{k_0^2}{r}$, dominant for far field zone ($r \gg \lambda$);
- $S^{nf} \approx K(r)\frac{1}{r^3}\left[3u_r\cdot u_r' - Id\right] = S_{stat}$, dominant for near field zone ($r \ll \lambda$);

- $S^{if} = K(r)\frac{ik_0}{r^2}\left[Id - 3u_r \cdot u_r^{'}\right] = -ik_0 r S_{stat}$, dominant for intermediate zone ($r \approx \lambda$).

In typical s-SNOM experiment, the probe dipole is close to the sample surface and illuminate by an external field $\mathbf{E}_i$ (shown in Figure 2.3.1), the induced dipole moment is described as $\mathbf{p} = \alpha \mathbf{E}_i$. For small sphere, the polarizability α is a complex number. When the distance between the probe and sample is very small, a part of the light is reflected from the surface toward the probe, shown in Figure 2.3.2. This extra "self-field" will modify the dipole moment and the probe-dipole radiation. To calculate this self-field, electrostatic image charge theory can be used, assuming that the spherical probe is very small compared to the wavelength and that the probe-sample distance is in the order of the probe diameter.

By influence of the electrical force, opposite image charges are then induced in the sample. From the electrostatic image charge theory, the image (mirror) induced dipole moment $\mathbf{p}_{im}$ is[151, 152]:

$$\mathbf{p}_{im} = \beta \begin{pmatrix} -1 & 0 & 0 \\ 0 & -1 & 0 \\ 0 & 0 & 1 \end{pmatrix} p \quad with \quad \beta = \frac{\varepsilon_s - \varepsilon_m}{\varepsilon_s + \varepsilon_m} \tag{2.3.3}$$

where β is the Fresnel reflection coefficient in the electrostatic limit. ε_s and ε_m are the dielectric functions of the sample and the external medium. The orientation of the image dipole depends on the probe dipole. When the probe dipole is parallel to the sample surface (xy plan), the image dipole is anti-parallel while it keeps the same orientation for a vertical probe dipole (z direction).

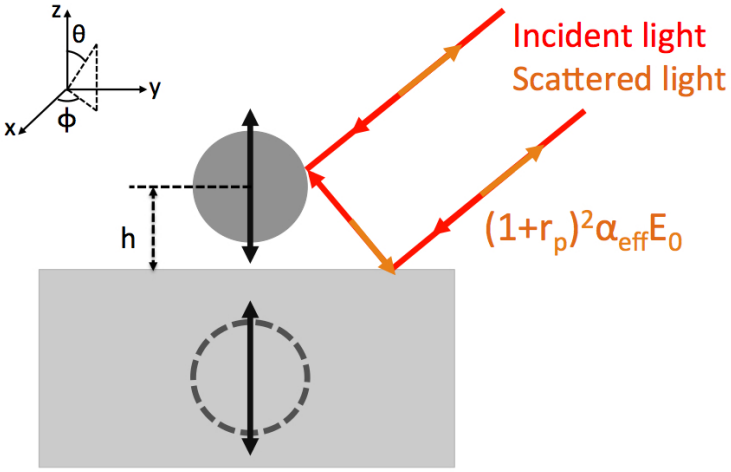

Figure 2.3.2.: The dipole (point of the probe) is illuminated by a direct field E_0 and a reflected field r_pE_0. The back-scattered field includes also a direct and a reflected contribution.

The quasi-static self-field induced by this image dipole at the probe position can be precisely expressed by using the near-field contribution of the dyadic tensor :

$$E_{self} = S^{stat}(r_p, r_{im})p_{im} \tag{2.3.4}$$

where r_{im} and r_p are the position of p_{im} and p respectively. Using the expression of the image dipole moment p_{im} and dyadic tensor, we find:

$$\mathbf{E}_{self} = K_c\beta \begin{pmatrix} -\frac{1}{8h^3} & 0 & 0 \\ 0 & -\frac{1}{8h^3} & 0 \\ 0 & 0 & -\frac{2}{4h^3} \end{pmatrix} p = S^{nf}_{self}(r_p, r_p)p \tag{2.3.5}$$

where S^{nf}_{self} is the dyadic tensor accounting for the reflection when the probe dipole is close to the sample surface. Taking into account the self-field, the total field at the probe position is now:

$$E_{local} = E_i + E_{self} = E_i + S^{nf}_{self}(r_p, r_p)p \tag{2.3.6}$$

and

$$\mathbf{p} = \alpha E_{local} \tag{2.3.7}$$

From Equation 2.3.6 and Equation 2.3.7, we can deduce an expression for "effective polarizability" α_{eff} for the external excitation field $\mathbf{E}_i$:

$$\mathbf{p} = \alpha_{eff}\mathbf{E}_i \quad with \quad \alpha_{eff} = \frac{\alpha}{1 - \alpha S^{nf}_{self}(r_p, r_p)} \tag{2.3.8}$$

where the self-field E_{self}[2] is taken into account. The tensor α_{eff} has two distinct components:

$$\alpha_{eff} = \begin{pmatrix} \alpha_{eff\parallel} & 0 & 0 \\ 0 & \alpha_{eff\parallel} & 0 \\ 0 & 0 & \alpha_{eff\perp} \end{pmatrix} \; with \; \alpha_{eff\parallel} = \frac{\alpha}{1 - \frac{\alpha\beta K_c}{8h^3}} \; and \; \alpha_{eff\perp} = \frac{\alpha}{1 - \frac{\alpha\beta K_c}{4h^3}} \tag{2.3.9}$$

The importance of the effective polarizability given by Equation 2.3.8 is obvious since the scattered field collected in far-field is proportional to the coupled dipole moment $\mathbf{p}$. We can now go one step further and determine the angular radiation pattern scattered by the probe in far-field, where the detection usually happens. As shown in Figure 2.3.2, there are two contributions to the far field radiation in a direction (θ, φ) of the homogeneous space above the surface, a direct contribution $\mathbf{E}_d$ and a reflected one $\mathbf{E}_r$:

$$\mathbf{E}_{scat}(\theta, \varphi) = \mathbf{E}_d(\theta, \varphi) + \mathbf{E}_r(\theta, \varphi) \tag{2.3.10}$$

In other word, eventual diffusion from the sample is omitted which is acceptable as long as the probe is not too close from an edge. In addition the s-SNOM, the probe polarization is typically along the z direction ($\mathbf{u}_z$) to benefit from the lightning rod enhancement at the tip apex. Usually only the vertical component of the field is considered even if the polarization is not purely vertical because the term $\alpha_{eff\perp} = \alpha_{eff,zz}$ is considered as markedly stronger. For a vertically oriented dipole, the direct contribution becomes simply :

[2]The self field E_{self} is also used in the expression of $\mathbf{E}_z$ in PiFM in next chapter (Equation **??**).

$$\mathbf{E}_d(\theta,\varphi) = \mathbf{E}_d(\theta) = K(r)\frac{k^2}{r}e^{ikr}\mathbf{p}_z\sin(\theta)u_\theta \tag{2.3.11}$$

Since the far-field radiation of a vertical dipole is purely p-polarized (along $\mathbf{u}_\theta$), the reflected contribution is simply $\mathbf{E}_r = r_p\mathbf{E}_d$. The scattered field is:

$$\mathbf{E}_{scat}(\theta,\varphi) = \mathbf{E}_{scat}(\theta) = K(r)\frac{k^2}{r}\mathbf{p}_z\sin(\theta)(1+r_p(\theta))u_\theta \tag{2.3.12}$$

If we consider the configuration depicted in Figure 2.3.2, the external incident field $\mathbf{E}_i$ is the sum of the directly incident field E_0 at large angle θ_0 and its reflection on the sample. Considering that the angle of incident field is indeed large and that mainly the vertical component of the field matters for the probe excitation, a qualitative approximation can be made:

$$\mathbf{p} = \alpha_{eff}\mathbf{E}_i \quad with \quad \mathbf{E}_i \approx (1+r_p(\theta_0))E_0u_z \tag{2.3.13}$$

Then the detected scattered field is considered approximately equal to :

$$\mathbf{E}_{scat}(\theta_0) \approx E_0K(r)\frac{k^2}{r}e^{i\omega t}\sin(\theta_0)\alpha_{eff\perp}(1+r_p(\theta_0))^2u_\theta \tag{2.3.14}$$

The scattered power in a small solid angle $d\Omega$ is :

$$dP_{scat}(\theta,\varphi) = \langle S(\theta,\varphi)\rangle\, dA \text{ with } \langle S\rangle = \frac{1}{2}\sqrt{\frac{\varepsilon_0\varepsilon}{\mu_0\mu}}\,|\mathbf{E}_{scat}|^2 \text{ and } dA = r^2d\Omega \tag{2.3.15}$$

The differential scattering cross section obtained by normalizing $dP_{scat}(\theta,\varphi)$ by incident power flux ($\langle S_i\rangle = \frac{1}{2}\sqrt{\frac{\varepsilon_0\varepsilon}{\mu_0\mu}}\,|\mathbf{E}_i|^2$) is:

$$\frac{d\sigma(\theta,\varphi)}{d\Omega} = \frac{dP_{scat}(\theta,\varphi)}{\langle S_i\rangle} \tag{2.3.16}$$

For vertical dipole at a small distance h, we insert the obtained expression for $\mathbf{E}_{scat}$:

$$\frac{d\sigma_\perp(\theta,\varphi)}{d\Omega} = \frac{k_0^4\left|\alpha_{eff\perp}\right|^2}{16\pi^2\varepsilon_0^2}\sin^2(\theta)\left|1+r_p(\theta)\right|^2 \tag{2.3.17}$$

and for an horizontal dipole, a similar derivation would give:

$$\frac{d\sigma_{\parallel}(\theta,\varphi)}{d\Omega} = \frac{k_0^4 \left|\alpha_{eff\parallel}\right|^2}{16\pi^2\varepsilon_0^2}(\left|1-r_p(\theta)\right|^2\cos^2\theta\cos^2\varphi + |1+r_s(\theta)|^2\sin^2\varphi) \tag{2.3.18}$$

These differential scattering cross sections specify the angular distribution of the scattered light. Then the total scattering cross section of the particle for the two perpendicular polarizations are:

$$\sigma_{\perp} = \int_{2\pi} d\sigma_{\perp} \propto \frac{\alpha_t^2}{(1-\frac{\alpha_t\beta K_c}{4h^3})^2} \tag{2.3.19}$$

and

$$\sigma_{\parallel} = \int_{2\pi} d\sigma_{\parallel} \propto \frac{\alpha_t^2}{(1-\frac{\alpha_t\beta K_c}{8h})^2} \tag{2.3.20}$$

where $d\sigma_{\perp}$ and $d\sigma_{\parallel}$ are given by Equation 2.3.17 and Equation 2.3.18.

According to Equation 2.3.19 and Equation 2.3.20, the scattering cross section is affected by the dipole-sample distance h and the polarizability of the probe α_t which is proportional to its volume.

For a probe very far from the sample ($h \gg a$), the denominators in Equation 2.3.19 and Equation 2.3.20 are very close to 1 so that $\alpha_{eff} \approx \alpha_t$. In this case, the scattering cross sections $\sigma(h)$ are usually minimal. When the probe approaches the surface, the denominators usually monotonically decreases (not always depending mostly on the value of β), so that the scattered power seems to increase exponentially until contact at $h = a$.

However as h decreases, a strong maximum in $\sigma_{\perp}$ may also be obtained near $\Re(\alpha_t\beta K_c) = 4h^3$. Neglecting the imaginary parts of α_t and β , the pole is reached for:

$$\beta\tilde{\alpha}_t = 4\tilde{h}^3 \quad with \quad \tilde{h} = \frac{h}{a} \tag{2.3.21}$$

where the dimensionless polarizability $\tilde{\alpha}_t = \frac{K_c}{a^3}\alpha_t$ is used to compare different probes. Thus, according to Equation 2.3.21for high polarizability probe, the maximum can be found before the contact. The resonance is then termed as *tip-induced resonance* and it is obtained for ε_t close to -2 for a sphere. This is visible on Figure 2.3.3 where the magnitude of the

squared effective polarizability ($\propto \sigma_{\perp}$) is shown as a function of both sample and probe permittivities. Similarly a resonance can be found for very large electrostatic reflection coefficient β, which is termed *sample-induced resonance*, and occurs near $\varepsilon_s = -1$. These sample-induced resonances are not obtained for many materials as permittivities are rather large for most of the materials, so that the ratios β and α_t are close to one. However real sharp probes can exhibit higher polarizability than a sphere. In addition β values can be large for polaritonic materials as ε is crossing zero to become negative with a small imaginary part. Therefore, as the distance becomes becomes small a strong coupling can occur .

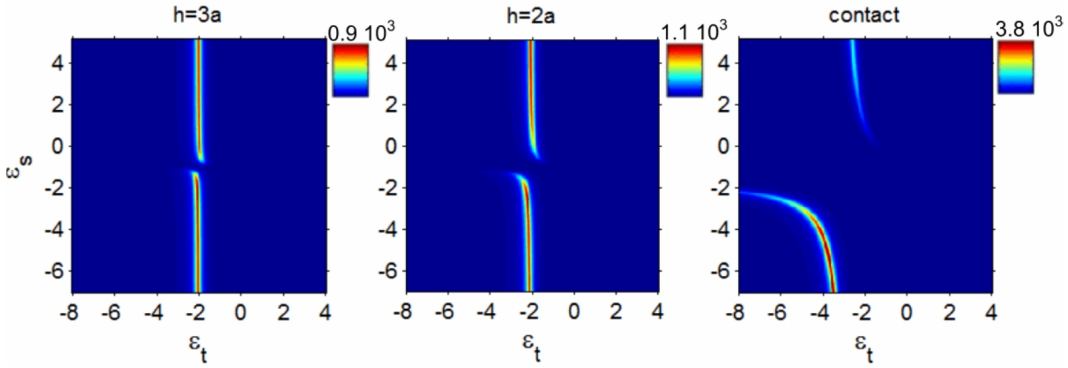

Figure 2.3.3.: Magnitude of the dimensionless effective polarizability $|\alpha_{eff\perp}(\tilde{\varepsilon}_{scat}, \varepsilon)|$ for a spherical scatterer at three different heights above the sample surface. An imaginary part of 0.1 is added to both permittivities.

2.3.2. Flaws and improvement of the Dipole model

In real experiment, the probe used for scanning the sample is usually very elongated. The vertical polarizability of needle-shaped probe is larger than that of a sphere. Several improvements can then be made such as considering the polarizability of small ellipsoid. In that case, tip induced resonance can be found at more negative value of the dielectric function, for $\varepsilon_t \approx -r^{1.6}$ where r is long axis to short axis ratio. However, an analytic expression for the real probe polarizability that are nearly semi-infinite does not exist. To determine the tip resonance position, it is interesting to consider the expression $Re(\varepsilon) = 1 - 2\pi/\Omega$[51] where $\Omega \approx \pi A^2$ represents the apex solid angle of the tip, for a conic apex full angle equals

to $2A$[3]. In consequence, the tip LSPR may be expected at strongly negative values, which is the case for metal in the mid-IR range. However if a the Drude model is used to estimate the tip permittivity, the imaginary part is also very strong so that no resonance is actually expected.

Thus, for more precise investigation, numeric methods should be considered, such as FDTD (finite-difference time-domain method) and FEM (finite element method). A drawback of the common electromagnetic solvers is that they often fail in precisely determining the scattered far field and do not provide many physical insights on the probe-sample interaction without extensive parametric studies.

Dyadic Green's function method

If we consider the probe as an ensemble of particles, the local field is a superposition of the incident radiation and all the partial fields scattered by the surrounding particles. To determine the total resulting field, the response of matter to incident radiation can be formulated by a collective response of individual dipoles, each occupying a volume element. This is the Dyadic Green's function method, or volume integral equation method (VIEM). As is seen in Equation 2.3.1, the field scattered at observation point (r_{obs}) by a single dipole is given by

$$\mathbf{E}_{scat}(r) = S(r_{obs}, r_p)p \tag{2.3.22}$$

Considering now large object, we use the polarization density $\mathbf{P}$ to generalize this formula:

$$\mathbf{E}_{scat}(r) = \int_{V_{r_p}} S(r_{obs}, r_p)\mathbf{P}(r_p)dV_{r_p} \tag{2.3.23}$$

where the integration include all the dipoles defined by their volume dV_{r_p} and $\mathbf{P}$ is related to the permittivity contrast between the material and the external medium via:

$$\mathbf{P}(r_p) = \varepsilon_0\chi\mathbf{E}(r_p) \quad with \quad \chi = \Delta\varepsilon(r_p) \tag{2.3.24}$$

[3]For the probes used in this work, $A \approx 0.02rad$, the estimated real permittivity of the probe $Re(\varepsilon_{probe}) \approx -1249$.

where $\Delta\varepsilon$ is the contrast between the material and the external medium and $\mathbf{E}(r_p)$ is the internal field. To evaluate the internal field, the situation is more complex now as we have a continuous collection of interacting dipoles. The problem can be solve iteratively[153]. Alternately, the field can calculated with an other method such as FDTD. Then , since we consider the field scattered in far field by a probe above a surface, we can use the far field propagator $\mathscr{S}$, the Equation 2.3.23 turns to:

$$\mathbf{E}_{scat}(r) = \int \mathscr{S}(r_{obs}, r_p)\mathbf{P}(r_p)dV_{r_p} \quad with \quad \mathscr{S} = S^{ff} + S^{ff}_{surf} \tag{2.3.25}$$

where S^{ff} corresponds to the Green dyadic tensor in free space in Equation 2.3.2. With $r_{obs} = (x,y,z)$ and $r_p = (x_p, y_p, z_p)$, it can be re-expressed explicitly:

$$S^{ff}(r_{obs}, r_p) = \frac{K(r)k^2}{r} e^{\left[-ik(\frac{xps}{r}+\frac{ypy}{r}+\frac{zpz}{r})\right]} \times \begin{bmatrix} 1-\frac{x^2}{r^2} & -\frac{xy}{r^2} & -\frac{xz}{r^2} \\ -\frac{xy}{r^2} & 1-\frac{y^2}{r^2} & -\frac{yz}{r^2} \\ -\frac{xz}{r^2} & -\frac{yz}{r^2} & 1-\frac{z^2}{r^2} \end{bmatrix} \tag{2.3.26}$$

and its surface reflected propagator S^{ff}_{surf} is written as[154]:

$$S^{ff}_{surf}(r_{obs}, r_p) = \frac{K(r)k^2}{r} e^{\left[-ik(\frac{xps}{r}+\frac{ypy}{r}+\frac{zpz}{r})\right]} \times \begin{bmatrix} \frac{x^2z^2}{\rho^2r^2}f_2 + \frac{y^2}{\rho^2}f_3 & \frac{xyz^2}{\rho^2r^2}f_2 + \frac{xy}{\rho^2}f_3 & -\frac{xz}{r^2}f_1 \\ \frac{xyz^2}{\rho^2r^2}f_2 + \frac{xy}{\rho^2}f_3 & \frac{y^2z^2}{\rho^2r^2}f_2 + \frac{x^2}{\rho^2}f_3 & -\frac{yz}{r^2}f_1 \\ -\frac{xz}{r^2}f_2 & -\frac{yz}{r^2}f_2 & (1-\frac{z^2}{r^2})f_1 \end{bmatrix} \tag{2.3.27}$$

with $f_1 = r_p(kk_\parallel)$, $f_2 = -r_p(k_\parallel)$, $f_3 = r_s(k_\parallel)$. $k_\parallel$ is the parallel wave vector given by $k_\parallel = k\frac{\rho}{r}$, where ρ is the radial coordinate of r in a cylindrical basis (u_ρ, u_φ, u_z). A similar expression involving transmission Fresnel coefficients can be found in[154] to calculate the far-field scattered through the surface. This method is particularly interesting to calculate the radiation patterns of a probe interacting with finite size object above a surface (object can be added in the integration volume).

Interestingly, such method shows that, when a dipole like scatterer approaches near a structure edge, a strongly asymmetric radiation pattern is arising (not shown here). Therefore the s-SNOM signal observed on the right edge or on the left edge of a structure is supposed to be strongly different, for a one-side illumination/detection. This is not really the case in mid-IR s-SNOM experiment though, as can be checked in most experimental results from literature. The asymmetric radiation across edges, however, can be observed in visible or NIR experiments. One possible explanation can be that real probes must be accounted for by relatively long probe, and that the shape of the radiation patterns of these probes excited at large wavelength remains relatively symmetric, even when they are crossing the edge of a nanostructure[4].

The disadvantage of this method compared to the simple dipole one is that the analytical expression is lost. Longer probe can be considered, but not semi-infinite probe either: this may still result in nonphysical resonances caused by the finite size (e.g. for probes of few microns in the mid-IR).

Lightning rod model

In the case of materials supporting strong surface phonons, a lightning rod model is proposed by McLeod et al.[13]. This method was not considered in this thesis, so only a brief description is presented.

In the previous described dipole-dipole model, the field inside the dipole sphere is homogeneous and evaluated at the center position. It means that we are considering two symmetric charge distributions accumulated on each top and bottom side of the sphere. This dipolar model can capture many features of the near-field signal scattered by tip apex while a real probe exhibits a strongly asymmetric charge distribution, with a higher charge density near the very apex.

The lightning rod model considers an axisymmetric probe of arbitrary geometry. The scattered field is considered to come from reorganization of charges developing along the entire length of the probe surface due to the incident light and the near field close to the sample surface, and the charge density on the probe is instantaneous distributed. This

[4]Further investigations are needed to confirm this behavior.

model quantitatively describes that the electric fields are localized strongly by an elongated geometry to a pointed apex.

2.4. Conclusion

To conclude, we have introduced some fundamental aspects of scattering typed scanning near field optical microscopy—s-SNOM. First a historical overview was presented and then three different types of SNOM, aperture-SNOM, s-SNOM and hybrid-probe SNOM were introduced briefly. Their advantages and drawbacks were presented. An example of s-SNOM investigation of a polar material showed signal change near phonon resonance. Then the nature of s-SNOM signal was presented. We have detailed the probe-sample signal to obtain the analytical expression of the field scattered in far field by a dipole probe above a surface, expressed in term of a dyadic function and this dipole approximation model is used for fitting experimental data. Finally some flaws and improvement of the dipole model was discussed. A general introduction of another near field approach PiFM will be described in the next chapter.

3. Fundamental aspects of PiFM

Contents

3.1 Background introduction of PiFM **56**

3.2 Comparison with other near-field spectroscopy techniques **61**

3.3 Analytic approximation of photo-induced force **64**

3.3.1 Optical force calculation based on Maxwell's stress tensor . . 65

3.3.2 Dipole-dipole approximation between probe and particle . . . 67

3.3.3 Dyadic Green's function method for PiFM 70

3.4 Conclusion **72**

Recently, new nano-spectroscopic techniques based on the use of atomic force microscope (AFM) have been developed beside SNOM. Theses techniques have been also used for investigating spectroscopically the materials at the nanoscale. One of the most interesting alternative to SNOM is the Photo-induced Force Microscopy (PiFM), which is able to mechanically detect optical interactions, i.e. without optical detector. Instead of detecting the optical scattering, the local optical force, induced by the illumination of the probe−sample region, is mechanically detected by the cantilever using a bimodal operation for the AFM. In this chapter, a background introduction to PiFM is provided. As for s-SNOM, an approximated model describing the photo-induced force is discussed. General comparison is finally made between the spectroscopic near-field techniques.

3.1. Background introduction of PiFM

The detection of optical scattering and gradient forces on micron sized particles was first reported in 1970 by Arthur Ashkin and then optical tweezers were used to hold and move microscopic dielectric objects[155]. The approach has been particularly successful in studying a variety of biological systems[156] in recent years. Many simulation and theoretical works have been conducted, while measuring optical force directly has also been the object of research and analysis for many years[157]. H. Kumar Wickramasinghe came up with the idea of mechanically detecting the measurable attractive force generated by dipole-dipole interaction in viable way almost a decade ago. This new near field technique is called photo-induced force microscopy (PiFM), originally called image force microscopy. Rajapaksa et al.[158] set up the system and performed the experiments. The first article about PiFM appeared in 2010[159] to show that this technique can detect and image the molecular resonance of feature down to the single molecular size purely by mechanical detection of the force between the optically driven molecular dipole and its mirror image in a metal coated probe. In this article, they performed PiFM image on 6-tamra dye molecule (Figure 3.1.1) and YOYO-3 dye molecule (Figure 3.1.2) on glass at different wavelengths in the visible range. The contrast of PiFM signal between dye molecule and the substrate changed at different wavelength near their absorption peak. From the inset in Figure 3.1.1 (e) we can see that the recorded PiFM data points at different wavelengths correspond well with the absorption spectrum taken by a standard spectrometer.

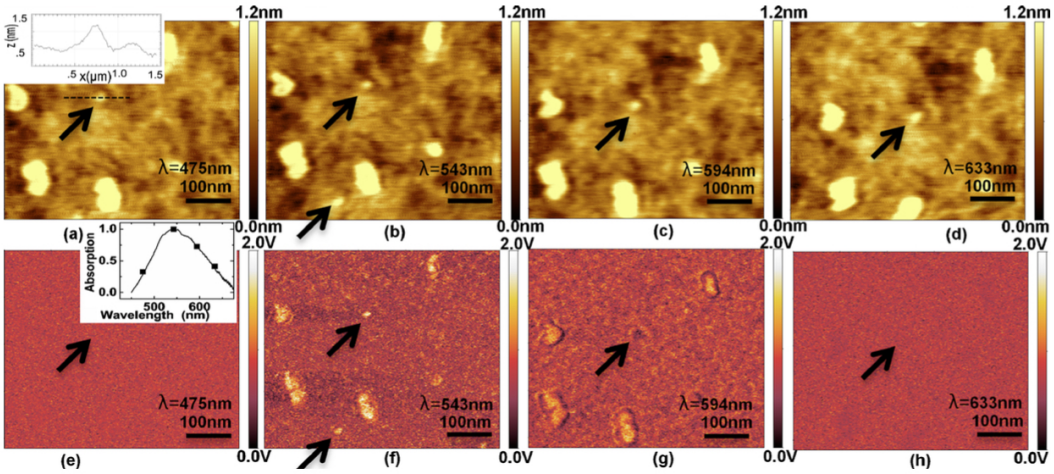

Figure 3.1.1.: 6-tamra dye molecule images on glass as a function of wavelength: (a)-(d) topography images; (e)-(h) simultaneously recorded PiFM images. Inset in (a): line scan across a molecular feature. Inset in (e): spectral data points from PiFM images compared with bulk measurements from spectrometer. From[159].

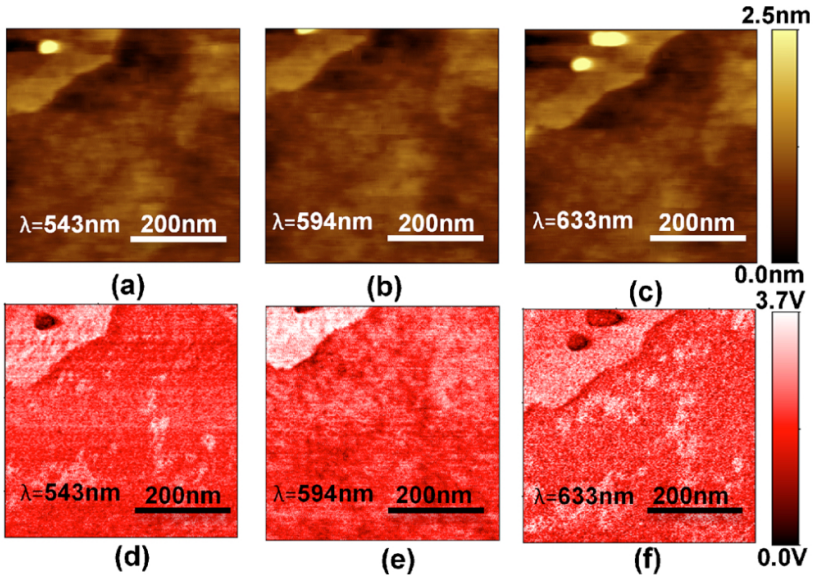

Figure 3.1.2.: YOYO-3 dye molecule images on glass as a function of wavelength: (a)-(c) topography images; (d)-(f) simultaneously recorded PiFM images. From[159].

The first commercial PiFM is fabricated in 2011[1]. Till now, it has been used as a high resolution microscopic and spectroscopic tool for investigation of different materials.

In 2015, F. Huang et al.[31] demonstrated that PiFM is able to recover the electric field intensity distribution of tightly focused laser beams with different polarizations. Their experimentally recorded force images agree well with theoretical predictions based on probe-dipole model. At the same year, another publication illustrated the fact that this near field approach can be used for linear and nonlinear optical spectroscopy at nanoscale to derive chemical information of the sample[161].

D. Nowak et al[25] presented the ability of imaging nanoscale patterns of the individual chemical components of block copolymer films, shown in Figure 3.1.3. Point spectra were taken at locations over PS and P2VP domains[2], the two peaks associated with PS (point B and D of blue curve in Figure 3.1.3) and the two peaks of P2VP (point C and E of red curve in Figure 3.1.3) are clearly observed. By mapping the sample at different IR wavelengths, the different contrast between PS and P2VP is presented and a material other than PS and P2VP may be present in the sample.

Dispersive and dissipative lineshapes In some nanospectroscopic experiments mentioned later on, the obtained spectra are similar to the spectra obtained by classical far-field absorption spectroscopy. The lineshape in that case can be said to be *dissipative* as it relates with material absorption. On the other hand the lineshape obtained with SNOM are considered as more *dispersive* as the signal depends clearly on the real part of the dielectric function of the sample (although not only).

In the expression of the photoinduced force, it is also customary to distinguish between a dispersive contribution coming from the real part of the polarizability α' (when a polarizable dipole is involved). While a dissipative a dissipative part is related to the imaginary part of the polarizability α'', which is related to absorption.

The PTIR and PFIR[3] spectra typically exhibit dissipative lineshapes: these techniques rely on the photothermal expansion of the sample. In fact, similar dissipative spectra were

[1]Commercial PiFM from Molecular Vista Inc.[160]

[2]PS is polystyrene and P2VP is poly(2-vinylpyridine).

[3]PTIR is photothermal induced resonance and PFIR is infrared peak force microscopy. They are introduced in subsection 3.2.

also obtained in certain PiFM measurements. In this situation, PiFM was considered as possibly mostly sensitive to absorption because of the presence of thermal effect affecting the AFM, namely photoexpansion effect[162]. If we consider the force formula described in section 3.3 (Equation 3.3.11, Equation 3.3.12 and Equation 3.3.13), PiFM is sensitive to both α' and α'' and it would follow a dispersive spectrum when α' is larger than α''. Thus, there is a debate on the exact mechanism of PiFM[163, 164] and this would be a interesting point for us and will be discussed in the experimental part of this thesis.

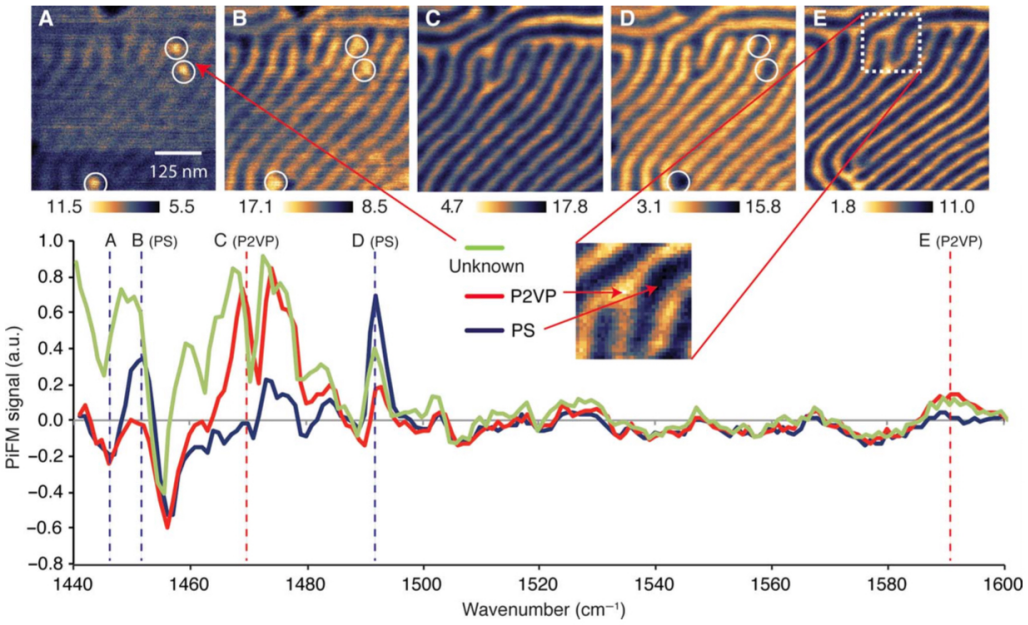

Figure 3.1.3.: Fingerprint region of PS-b-P2VP. (A to E) PiFM imaging at (A)1447cm−1, (B)1452cm−1, (C)1469cm−1, (D)1492cm−1, and (E)1589cm−1. The PiFM point spectra taken from the locations shown in (E) were normalized against a Si background. The different spectral response (green curve) of one of the three nodules clearly visible in (A) suggests that a material other than PS and P2VP may be present. From[25].

Previous achievements on PiFM

We mentioned that PiFM can also image the local field of nanostructures. Tumkur et al.[165]showed that the enhancement of photo-induced forces in gold disk dimers follows

the expected plasmonic field enhancements at 785nm (NIR). Shown in Figure 3.1.4, the experimentally measured photo-induced force intensity maps for two in-plane polarizations of incident light are in good agreement with the FDTD simulation of near-field electric field enhancements in our plasmonic structures. Recently Ambrosio et al.[166, 167] have reported PiFM image of plasmonic resonance in mid-IR range by imaging the phonon polaritons in hexagonal boron nitride.

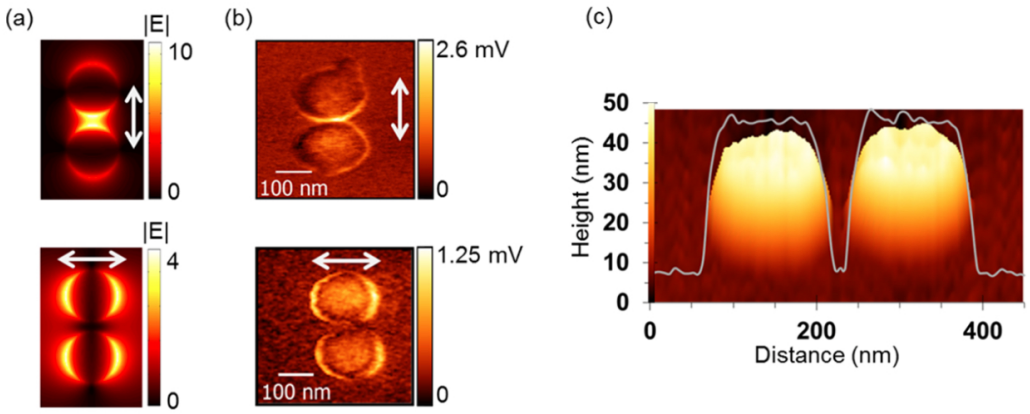

Figure 3.1.4.: Simulations and PiFM image of gold disk dimers: (a) FDTD simulations of the electric field (|E|) distribution on gold disk dimers (for disk radius = 150 nm, gap size = 30 nm, and height =35 nm) calculated for longitudinal (top panel) and transverse (bottom panel) polarizations, at the wavelength λ = 785 nm; (b) Measured photo-induced force intensity maps on the fabricated gold disk dimers with longitudinal (top panel) and transverse (bottom panel) polarizations at λ = 785 nm. The white arrows indicate the direction of the in-plane polarizations; (c) Representative AFM topography image of the same gold disk dimer shown in the bottom panel of (b), along with the height profile measured along the axis of the dimer (gray line). From[165].

As an emerging near field technique, PiFM is capable of local field imaging and nanoscopy for investigation of material properties, such as optical property and chemical property. Compared to other traditional methods, PiFM has some advantages. As a near field excitation it is able to work with low laser powers, which is helpful for studying molecules with high photo degradation. As a near field detection, there won't be much signal loss and it is background free. Since the force signal is detected by a lock-in amplifier, optical detector alignment procedure is not needed.

3.2. Comparison with other near-field spectroscopy techniques

The growing interest in plasmonic-like IR material is accompanied by a blooming of available characterization tools. They are indispensable in IR plasmonics study and help us understand the properties of the investigated sample, such as the morphology, chemical composition, optical response, etc. To observe the morphology of the sample, scanning electron microscope (SEM), atomic force microscope (AFM) can have a very high resolution and give us a view of the topography of the sample at nanoscale. For optical properties, spectroscopies, especially nano-spectroscopic imaging systems, can be a good choice to explore 2D or nano-structured polaritonic materials. In the following, these nano-spectroscopic methods are briefly presented for comparison purpose.

Besides PiFM, s-SNOM, introduced in the previous chapter, is a more familiar nanoscopic investigation tool for nanostructures and it is the technique used in nano-FTIR[168].

Photothermal Induced Resonance (PTIR)[24, 22, 23] is another related technique for vibrational analysis with scanning probe microscopy. PTIR, also known as AFM-IR (atomic force microscope infrared-spectroscopy) combines two instrumental techniques, infrared spectroscopy and scanning probe microscopy, and it provides a direct, and relatively unambiguous measurement of infrared absorption. Figure 3.2.1 shows the schematic of PTIR.

A pulsed tunable IR laser source is focused on a sample near the AFM tip and it can cause a rapid expansion which induces a oscillation of the AFM cantilever proportional to the IR absorption (shown in Figure 3.2.1 (B)). As the wavelength of the laser source scans, an absorption spectrum is obtained by measuring the cantilever oscillation amplitude (shown in Figure 3.2.1 (C)).

Standard PTIR is based on contact mode of AFM, while more recently a taping mode PTIR[125] has been developed to achieve a spatial resolution of 10 nm. BE mode and ENZ mode of plasmonic ENZ materials have been studied by PTIR[49]. AFM-IR spectrum is taken on a 100nm thick SiO_2 thin film on Si substrate with gold coated silicon probe for BE mode investigation and 2nm thick SiO_2 thin film for ENZ mode study. In AFM-IR spectra, absorption peak is observed for both modes at $\mathrm{Re}(\varepsilon) = 0$. For BE mode, the peak is weaker

than that corresponds to maximum Im(ε) of SiO_2 while for ENZ mode the result is inverse, the peak for ENZ mode is stronger.

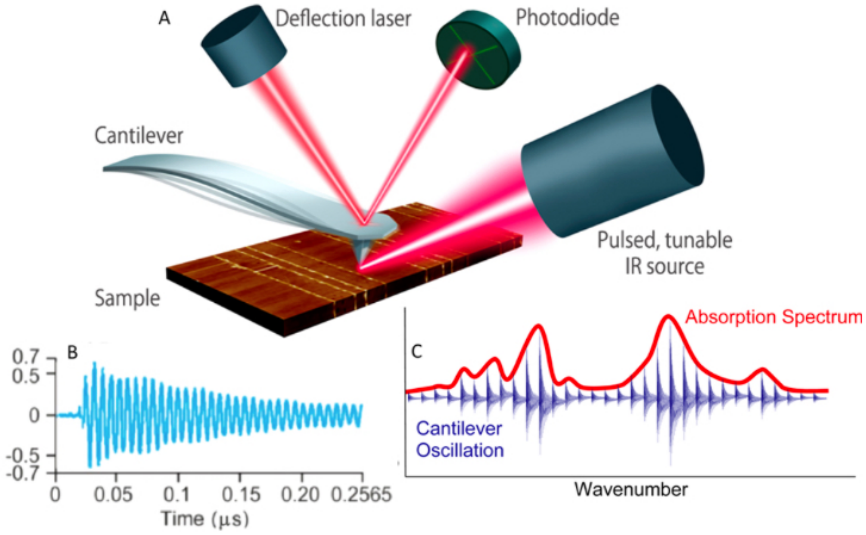

Figure 3.2.1.: Operational scheme of PTIR microscopy: (A) Schematic diagram of AFM-IR; (B) the sample's photothermal expansion induces a transient cantilever oscillation that is proportional to the IR absorption; (C) measuring the AFM cantilever oscillation amplitude as a function of wavelength (or wavenumber) results in a local absorption spectrum with nanoscale spatial resolution. From[22, 125].

Infrared Peak Force (PFIR) microscopy is a more recent scanning probe spectroscopic method is developed by Wang et al.[27]. Peak force (PF) tapping is a novel operation mode of AFM. Instead of working at the frequency of cantilever resonance, PF works at a non-resonant mode, which is at a frequency far below cantilever resonance. Also the principal of PFIR is similar with AFM-IR, this technique has a higher spatial resolution (∼10 nm) due to the PF tapping mode.

The operation scheme of PFIR is shown in Figure 3.2.2. The pulsed light is focused on the sample and tip and it is operated at a frequency synchronized with the peak force tapping frequency. The detector records time response of the cantilever with and without the laser pulse and the PFIR absorption spectrum is obtained by the subtraction between

the two signals. The difference of the peak force signal is owing to the thermal expansion caused by the infrared laser.

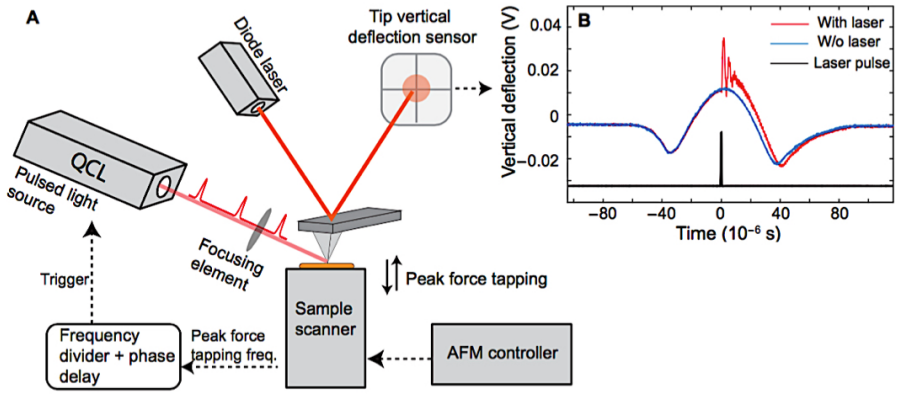

Figure 3.2.2.: Operational scheme of PFIR microscopy: (A) Operation diagram of PFIR; (B) Gate-averaged traces of vertical deflections of the cantilever with the laser interaction (red curve) and without the laser interaction (blue curve). The timing of the infrared laser pulse (black curve) is chosen to be within the contact regime of the peak force tapping cycle. Subtraction of the two vertical deflection traces (red and blue, with and without laser respectively) is used to obtain the PFIR trace. From[27].

These four techniques are all AFM-based near field optical spectroscopy. A coarse comparison of these four techniques are summarized in Table 3.1:

Technique	AFM operation mode	Signal measured	Sensitive to	Advantages	Drawbacks
s-SNOM	Tapping	Light scattered by the probe-sample system	Complex ε	• Optical phase information (with interferometry)	• Background issue • Complicated detection
PiFM	Tapping	Force induced by laser	model-dependent	• High resolution • AFM-based detection	• Probe with two well-behaved resonances • (Photothermal contribution?)
PTIR	Contact (tapping recently)	Force induced by thermal expansion	Imaginary part of ε	• Simple instrumentation design • Investigation of a greater depth into the sample (depend on requirement)	• Contact mode: smooth and clean sample • Relatively lower resolution
PFIR	Peak force mode (PFM)	Force induced by thermal expansion	Imaginary part of ε	• higher resolution than PTIR • PFM advantages	• Less sensitive to real permittivity

Table 3.1.: Tentative comparison of the four near-field spectroscopy techniques.

As high resolution spectroscopy techniques, they are all potentially good choice for material investigation. For us, since HDSC sample (Si n-doped InAsSb on GaSb substrate) is investigated near its plasma frequency, we are more interested in the change of real permittivity. Thus we use s-SNOM and PiFM in our work. The PiFM was acquired in our laboratory during this thesis.

3.3. Analytic approximation of photo-induced force

The photo-induced force (PiF) is initially presented as an optical force detected by an AFM metal probe in the presence of a molecule dipole underneath the tip. Hence, the basic principle of PiFM is to detect the force gradient existing between the optically driven molecular dipole and its mirror image in a metal coated AFM tip. Both illumination and detection are in the near field region. To understand the phenomena, two analytic approximations are used, a classical optical force calculation based on Maxwell's stress tensor and a dipole-dipole model. These two models are presented in this section. Some part of the following derivations are presented extensively in the PhD work of I. Rajapaksa[158].

3.3.1. Optical force calculation based on Maxwell's stress tensor

The general law for force in electromagnetic fields is based on the conservation law for linear momentum. We therefore derive this conservation law based on Maxwell's equations. According to the Lorentz force law, the total force of an integration volume V is then described as:

$$\mathbf{F}(r,t) = \int_V [\rho(r,t)\mathbf{E}(r,t) + j(r,t) \times \mathbf{B}(r,t)]\, dV \tag{3.3.1}$$

where ρ is the charge density and j is the current density. This expression applies to a distribution of charges and currents satisfying the charge conservation law $\nabla \cdot j + \frac{\partial \rho}{\partial t} = 0$. After some derivations by extended calculation of Maxwell's equations, the following formula is obtained:

$$\nabla \cdot \left[\varepsilon_0 EE - \mu_0 HH - \frac{1}{2}(\varepsilon_0 E^2 + \mu_0 H^2) \overleftrightarrow{I} \right] = \frac{d}{dt} \frac{1}{c^2} [E \times H] + \rho E + j \times B \tag{3.3.2}$$

The expression in brackets on the left side is called Maxwell's stress tensor in vacuum, usually denoted as $\overleftrightarrow{T}$ (Equation 3.3.3)[154]. It is usually used in classical electromagnetism to represent the interaction between electromagnetic forces and mechanical momentum, as will be presented in the following.

$$\overleftrightarrow{T} = \varepsilon_0 EE - \mu_0 HH - \frac{1}{2}(\varepsilon_0 E^2 + \mu_0 H^2) \overleftrightarrow{I} \tag{3.3.3}$$

After integration of Equation 3.3.2 over an arbitrary volume V which contains all the charge density and current density we obtain:

$$\int_V \nabla \cdot \overleftrightarrow{T}\, dV = \frac{d}{dt} \frac{1}{c^2} \int_V [E \times H]\, dV + \int_V [\rho E + j \times B]\, dV \tag{3.3.4}$$

The last term $\int_V [\rho E + j \times B]\, dV$ is recognized as the mechanical force (Equation 3.3.1). As it is well known, the volume integral can be transformed to a surface integral using Gauss's integration law. Equation 3.3.4 is re-expressed as

$$\int_V \nabla \cdot \overleftrightarrow{T}\, dV = \oint_S \overleftrightarrow{T}\, nda \tag{3.3.5}$$

where S is the surface of the volume V, n is the unit vector perpendicular to the surface and da is the infinitesimal surface element. Then we arrive at the conservation law for linear momentum:

$$\oint_S n \overleftrightarrow{T}\, da = \frac{d}{dt}(\mathbf{P}_{field} + \mathbf{P}_{mech}) \tag{3.3.6}$$

where $\mathbf{P}_{field}$ is the field momentum and $\mathbf{P}_{mech}$ is the mechanical momentum. Since the mechanical force can be presented as $\frac{d\mathbf{P}_{mech}}{dt}$, the field momentum is defined as:

$$\mathbf{P}_{field} = \frac{1}{c^2}\int_V [E \times H]\, dV \tag{3.3.7}$$

The field momentum is zero when it is averaged over one oscillation period $\frac{d}{dt}\langle \mathbf{P}_{field} \rangle = 0$, so the average mechanical force becomes:

$$\langle \mathbf{F} \rangle = \frac{d}{dt}(\langle \mathbf{P}_{mech} \rangle) = \oint_S \left\langle \overleftrightarrow{T} \right\rangle nda \tag{3.3.8}$$

Then the time averaged Maxwell's stress tensor is given by:

$$\left\langle \overleftrightarrow{T}_{i,j} \right\rangle = \varepsilon E_i E_j^* - \mu H_i H_j^* - \frac{1}{2}\delta_{ij}(\varepsilon E^2 + \mu H^2) \tag{3.3.9}$$

This Maxwell's stress tensor (MST) is usually used for numeric methods, such as FDTD and FEM. As is presented in the dissertation of I. Rajapaksa[158], they used a full vectorial 3D electromagnetic method[4] to calculate PiF. They expand Equation 3.3.9 in the field terms and then perform the surface integral to find this optical force (Equation 3.3.8).

Figure 3.3.1 is a simulated force versus distance curves of Nile Blue and Rhodamine[158]. The curves in this figure shows that PiF signal on the same molecule at different wavelengths is quite different. For Rhodamine, the signal increases about 3.5 times from 633 nm to 543 nm and the increase for Nile Blue is even larger.

[4]FEM method and FDTD simulation should also give the similar result.

With numerical method based on MST, the simulation can be done at the same sample probe distance at different wavelength, then a simulated PiFM spectrum could be generated and compared with experimental spectrum.

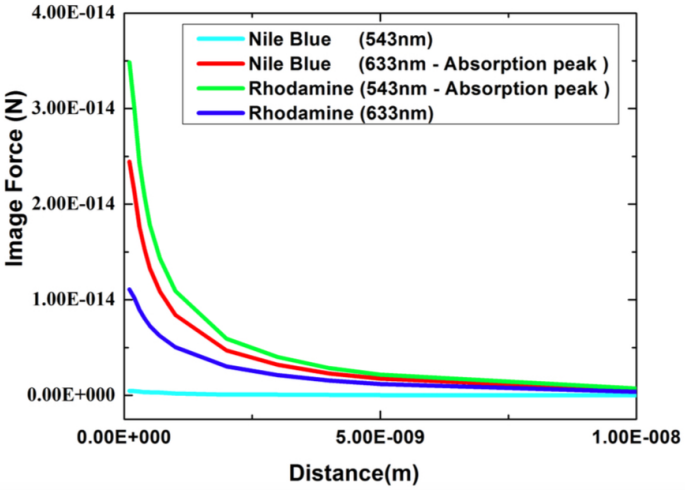

Figure 3.3.1.: Simulation of force vs distance relationship of photo-induced force, from[158].

3.3.2. Dipole-dipole approximation between probe and particle

Photo-induced force can be described as an interaction between tip and the sample when illuminated with laser, a system of two dipoles, a particle dipole and its image dipole in the probe, can be considered. Referring to Figure 3.3.2, a tip is interacting with a particle dipole on a substrate. In this case, the structure (molecule) is much smaller compared to the nanoprobe which is very different from the presented s-SNOM model. This representation will probably not be adapted in case of plasmonic or polaritonic material: even if they are structured, their dimensions is usually much larger than the tip apex.

However, this first PiFM model can work in other configurations and it can be described further. As previously, it is considered that the substrate acts as a mirror and we replace it with a mirror image of the tip plus the mirror image of the particle shown in Figure 3.3.2 (b). After multiple reflections in the tip and in the (usually) weaker tip mirror image[5],

[5]E.g. notably if we consider the image produced by a polymer, whose dielectric function is typically small and positive so that β is relatively weak.

several particle dipole/image dipole pairs appear as shown in Figure 3.3.2 (c). If we neglect the weak reflections, we can approximate the situation as a particle essentially interacting with its mirror image in the tip (Figure 3.3.2 (d)).

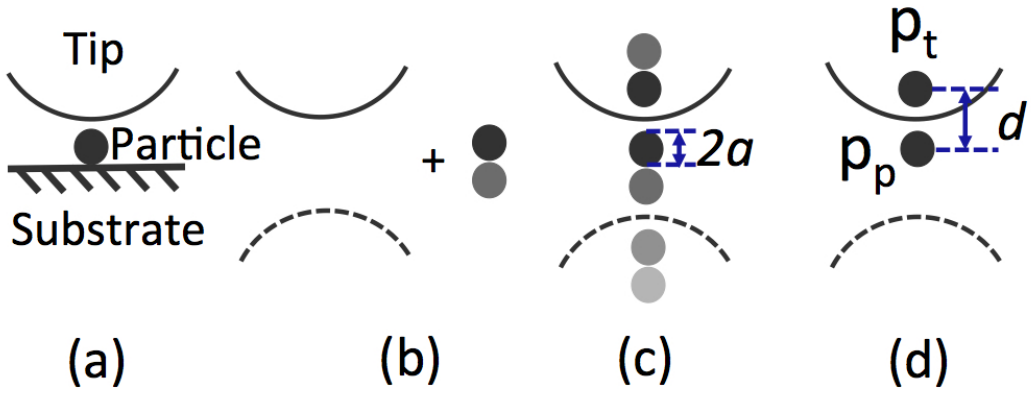

Figure 3.3.2.: The particle dipole model of the PiFM system, from[159].

Then we can use the relatively general time-averaged PiF described by Dholakia and Zemánek[169] and by Arias-González and Nieto-Vesperinas[170]:

$$\langle \mathbf{F} \rangle \propto Re \left\{ \sum_i P_i^*(r) \nabla E_i(r) \right\} \quad with \quad i = x,y,z \tag{3.3.10}$$

where $\mathbf{P}^*(r)$ is the optically induced polarization of the tip and $\mathbf{E}(r)$ is the optical electric field in the vicinity of the tip influenced by the polarization of the sample[6]. The time average force can be expressed as the sum of a localized force and a non-localized force:

$$\langle \mathbf{F} \rangle = \mathbf{F}_{loc} + \mathbf{F}_{nloc} \tag{3.3.11}$$

$\mathbf{F}_{loc}$ is the localized force which depends on the distance d between the tip and the sample. $\mathbf{F}_{nloc}$ is the non-localized force. The latter is independent of d[154, 169]. The expressions of these two forces are written as[171, 31]:

[6]The polarizability of the particle is used when the particle is considered as a dipole while the polarizability of the tip is considered for probe-dipole situation.

$$\mathbf{F}_{loc} \propto -\frac{1}{d^4} Re\left\{\alpha_p \alpha_t^*\right\} |E_z|^2 \tag{3.3.12}$$

$$\mathbf{F}_{nloc} \propto Im\left\{\alpha_t\right\} |E_x|^2 \tag{3.3.13}$$

where $\alpha_p$and α_t are the polarizability of the sample and tip, respectively and the expression of the polarizability is $\alpha = \alpha' + i\alpha''$. Here, E_z and E_x are the z and x components of the incident field. According to this model, a high spatial resolution in PiFM is expected as F_{loc} is proportional to $\frac{1}{d^4}$, which lead to the highly localized force sensitivity. On the other hand, the non-localized force lacks this spatial confinement.

In our case, the probe is much smaller compared with the sample. Considering probe dipole, only the polarizability in the formula changed:

$$\mathbf{F}_{loc} \propto -\frac{1}{d^4} Re\left\{\alpha_t \alpha_p^*\right\} |E_z|^2 \tag{3.3.14}$$

$$\mathbf{F}_{nloc} \propto Im\left\{\alpha_p\right\} |E_x|^2 \tag{3.3.15}$$

We now consider the case where only the z component of the total force that is detected by the AFM cantilever without nanoparticle. As we have mentioned in the background introduction of PiFM, F. Huang et al.[31] imaged laser distribution on a glass substrate without any particles. Time averaged $\mathbf{F}_z$ is expressed by the electrostatic approximation[154] derived from Equation 3.3.10:

$$\langle \mathbf{F}_z \rangle = Re(\mathbf{P}_{t,x}\frac{\partial \mathbf{E}_{t,z}}{\partial x} + \mathbf{P}_{t,y}\frac{\partial \mathbf{E}_{t,z}}{\partial y} + \mathbf{P}_{t,z}\frac{\partial \mathbf{E}_{t,z}}{\partial z}) \tag{3.3.16}$$

$\mathbf{P}_{t,x}$, $\mathbf{P}_{t,y}$, $\mathbf{P}_{t,z}$ are the dipole moment of the tip along x, y, z direction. $\mathbf{E}_{t,z}$ is the z component of the electric field on the AFM probe (refer to Equation 2.3.5, $\mathbf{E}_{self}$ in SNOM part). F. Huang et al.[31] considered the probe as an ellipse with short radius $l'$and long radius l. The distance between probe-dipole and its image dipole is d, shown in Figure 3.3.3.

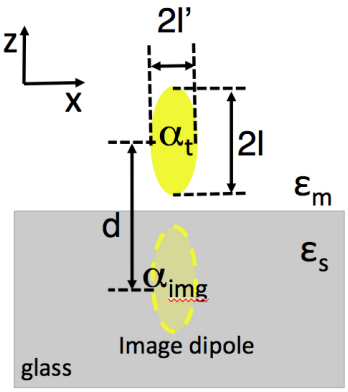

Figure 3.3.3.: The probe-dipole model of the PiFM system.

If we assume l, $l' \ll \lambda$, the optical force on the tip is given by:

$$F_z = \frac{24\pi\varepsilon_0\alpha'_{t,x}\alpha'_{img,x}d}{(d^2+l'^2)^{5/2}}|E_x|^2 + \frac{24\pi\varepsilon_0\alpha'_{t,y}\alpha'_{img,y}d}{(d^2+l'^2)^{5/2}}|E_y|^2 + \frac{8\pi\varepsilon_0\alpha'_{t,z}\alpha'_{img,z}(3d^2+l^2)}{(d^2-l'^2)^3}|E_z|^2 \tag{3.3.17}$$

where $\alpha'_{t,i}$ (i=x, y, z) is the real polarizability of the probe-dipole along x, y, z direction and $\alpha'_{img,i}$ (i=x, y, z) is the real polarizability of the image probe-dipole along x, y, z direction. $\alpha'_{img,i} \propto \beta\alpha'_{t,i}$ as defined in Equation 2.3.3. E_i (i=x, y, z) is the incident light.

This formula is for the calculation of PiF on a glass substrate. However, this model is not tested on plasmonic samples with nanostructures (dimension much larger than the tip apex).

3.3.3. Dyadic Green's function method for PiFM

In the recent work of Ladani and Potma[172], a dyadic Green's function formalism for PiFM is presented. They considered a gold probe in the vicinity of a pure glass substrate and a glass substrate covered by a 45 nm gold film. There is no nanoparticle on the sample. Expanded from Equation 3.3.10, the force can be represented as:

$$\langle \mathbf{F}(t) \rangle = \frac{\alpha'}{2}\sum_i Re\{E_i^* \nabla E_i\} + \frac{\alpha''}{2}\sum_i Im\{E_i^* \nabla E_i\} \tag{3.3.18}$$

In contrast with s-SNOM signal, in this assumption model for PiF, an *evanescent background field* (z field decay factor γ) is considered. The PiF along z direction, based on a dyadic Green's function formalism, can be written as:

$$\langle \mathbf{F}_z \rangle = \frac{1}{2} \sum_i \left| E_t^l \right|^2 (-\gamma \alpha_{t,i}^{l'} + \left| \alpha_{t,i}^l \right|^2 Re \left\{ \frac{1}{S_{t,i}^l} \frac{\partial G_{sc;t,i}^l}{\partial z} \right\}) \; with \, i = x, y, z \tag{3.3.19}$$

where E_t^l is the local electric field at the tip, $\alpha_{t,i}^l = \alpha_{t,i}^{l'} + i\alpha_{t,i}^{l''}$ is the complex tip's local polarizability and $\alpha_{t,i}^{l'}$ is the real part. $G_{sc;t,i}^l$ is the dyadic Green's functions (as described in Equation 2.3.27 in SNOM part) and $S_{t,i}^l = 1 - \alpha_{t,i}^l G_{sc;t,i}^l$ as a self interaction term.

Dispersive lineshape of PiF With the formula above, a calculation for PiF as a function of frequency and tip-substrate distance in two mentioned experimental geometries are presented in Figure 3.3.4. The real and imaginary parts of the tip's polarizability are indicated in Figure 3.3.4 (c). The dispersive and dissipative line shapes correspond to the real and imaginary polarizability respectively. We can see from Figures 3.3.4 (a) and (b), PiF on gold thin film (where exists a SPP excitation) is about 15 times larger and more localized compared to pure glass substrate. In addition, the distance dependence is more obviously on gold film. Consider the frequency dependence, from Figure 3.3.4 (b) we can observe a dispersive lineshape of PiF and its maximum value is near the plasmonic resonance of the tip.

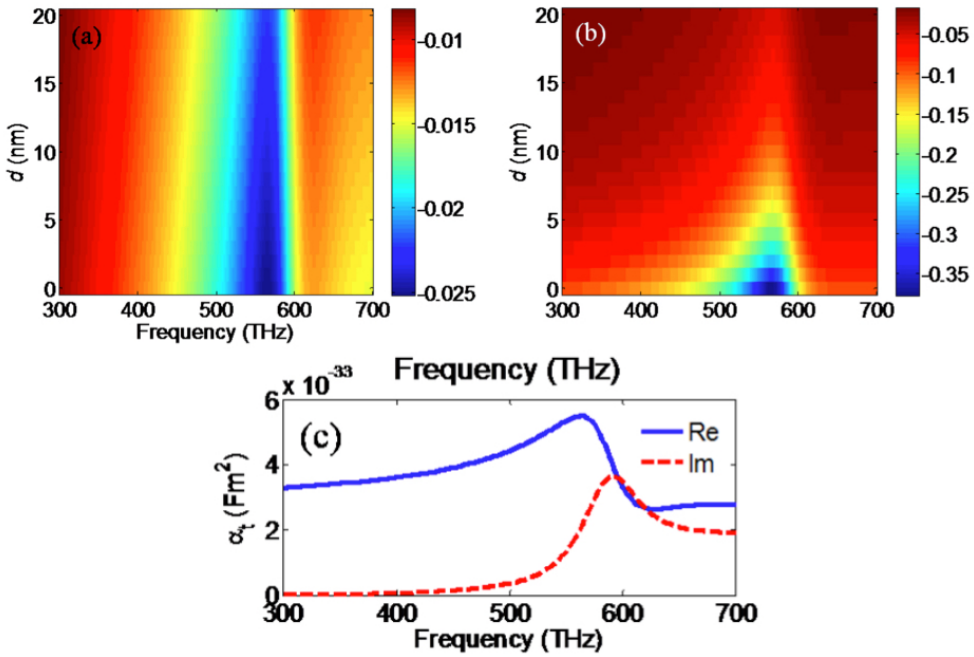

Figure 3.3.4.: Calculated $\langle \mathbf{F}_z \rangle$ on a gold tip as a function of frequency and tip-substrate distance d: (a) $\mathbf{F}_z$ calculated on a glass substrate; (b) $\mathbf{F}_z$ calculated on a glass substrate covered with a 45 nm gold film. Force is given in picoNewton (pN); (c) frequency dependence of the real (blue) and imaginary (red) parts of the tip's polarizability. From[172].

3.4. Conclusion

To conclude, we had introduced some fundamental aspects of PiFM. First the literature background of this novel technique was introduced and some recent research with PiFM were presented. Then we focused on the theoretical explanation (analytic approximations) of PiFM signal. First, we have derived the expression of the optical force based on Maxwell's stress tensor (MST). This expression is commonly used for optical force measurement analysis, using numerical methods such as FDTD. Then a particle-dipole model was presented considering a system including a small particle on the substrate and the probe. Another model based on probe-dipole without nanoparticle was also introduced[7].

[7]This model was used by the author for calculating the PiFM imaging of a focused red laser spot on a bare glass substrate, showing nice correspondence with experimental data.

Finally, a recent formula based on Green's function was introduced for SPP system (gold thin film on glass substrate). This model shows that the force is localized in the vicinity of thin film surface and predicts that the frequency dependent PiF spectrum can have a dispersive lineshape. As a potential characterization tool for material investigation, the nature of PiFM signal still has some debates and future explorations need to be conducted. In next chapter, experimental details including sample and instrument will be presented.

Part II.

Near field spectroscopic investigation

4. Experimental details

Contents

4.1 Investigated HDSC samples **76**

4.1.1 Fabrication procedure 76

4.1.2 HDSC 1D gratings 77

4.1.3 2D periodic rectangular nanoantenna array 83

4.2 Mid-IR nanoscopy: setups and experimental development **84**

4.2.1 s-SNOM 85

4.2.2 PiFM setup 95

4.3 Conclusion **106**

In this chapter, we first provide experimental details about the investigated HDSC samples, regarding their shape, size and dielectric function determined using FTIR. Then we provide information on the experimental setups that have been used and developed. Scattering-type SNOM and PiFM are both microscopic techniques based on an AFM system which are able to spectroscopically investigate the HDSC structures. Despite setup similarities, in the current version, the two systems are independent and they are operating with different probes. PiFM also typically requires specific, pulsed, sources that are not necessarily available or affordable. In this chapter we propose an experimental method to alleviate this issue.

4.1. Investigated HDSC samples

Mainly, two HDSC samples have been considered, made in the Nanomir group at IES[1] (Montpellier) in the framework of an ANR project led by T. Taliercio. They consist in (n-type) Si-doped InAsSb nanostructure on an nearly undoped GaSb substrate. For the first sample, the HDSC structures consist in a periodic array of submicronic ribbons (gratings). This sample is shown in Figure 4.1.2, and it will be investigated by both s-SNOM and PiFM in the next chapter. The second one is 2D periodic array which has been mostly investigated by s-SNOM. The general fabrication procedure is shortly described hereafter.

4.1.1. Fabrication procedure

The HDSC samples were fabricated at IES by F. Barho. Figure 4.1.1[33] schematizes the process flow of the fabrication[33, 34, 173]. The HDSC nanostructures were made through photolithography and chemical etching. The sample surfaces were first cleaned with organic solutions, blew dried with dry-N_2 and heated for 2 min at 120°C. The sample is then covered with positive photoresist (AZMIR-701) mask with grating patterns. The gratings and 2D array with constant periodicity were patterned by photolithography. For the 2D rectangular nanoantennas, a second exposure is performed by rotating the mask by $90°$[2].

Afterwards, wet etching was conducted with a citric acid ($C_6H_8O_7$) and hydrogen peroxide (H_2O_2) solution to define the grating and the ribbon width is controlled by the etching time. Finally, the photoresist is removed in acetone and the structure is then cleaned by isopropanol and dried. The submicronic ribbons present high verticality of the side walls and great structural quality as shown in Figure 4.1.2 (b). The 2D periodic nanoantenna arrays were fabricated following the same process with double lithographic exposure.

[1] IES: Institut d'Electronique du Sud.

[2] The two step exposure for 2D array fabrication is called "double lithographic exposure".

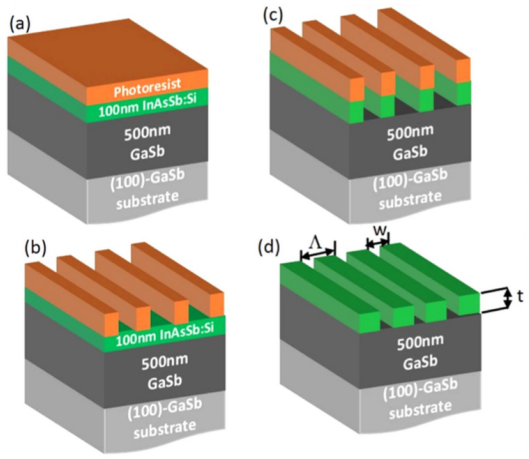

Figure 4.1.1.: Process flow for sample fabrication by photolithography and chemical etching: (a) Organic cleaning of surface; (b) UV photolithography and resist development; (c) Chemical wet etching; (d) Photoresist removal and surface cleaning. Figure adapted from[33].

4.1.2. HDSC 1D gratings

As can be seen on Figure 4.1.2, the thickness of the highly doped InAsSb is 100 nm, the width is 700 nm and the pitch is 1.6 μm.

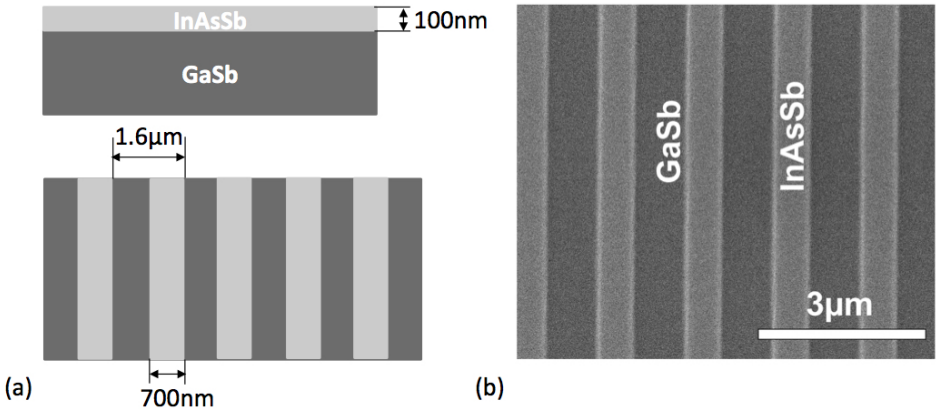

Figure 4.1.2.: HDSC gratings: (a) Scheme of the InAsSb gratings on GaSb substrate; (b) SEM image of HDSC.

Sample homogeneity

The structural inhomogeneity of the sample has been checked by X-ray diffraction. Figure 4.1.3 presents the high-resolution X-ray diffraction (HRXRD) of the InAsSb sample grown on GaSb substrate. The HR-XRD measurements were carried using a PANalytical X'Pert3 MRD equipped with a PIXcel1D linear detector, an X-ray tube delivering the CuK1 radiation and a four-bounce asymmetric Ge(220) monochromator. The simulation was estimated using HR-XRD simulated curves in the framework of the dynamical modeling from the X'pert epitaxy© software. The comparison between the simulation and the experimental pattern shows that there is no visible broadening of the layer. It demonstrates, without ambiguity, a homogeneous layer of 100 nm thick InAsSb with 90.8 % of As that represents a lattice mismatch of 0.037 %.

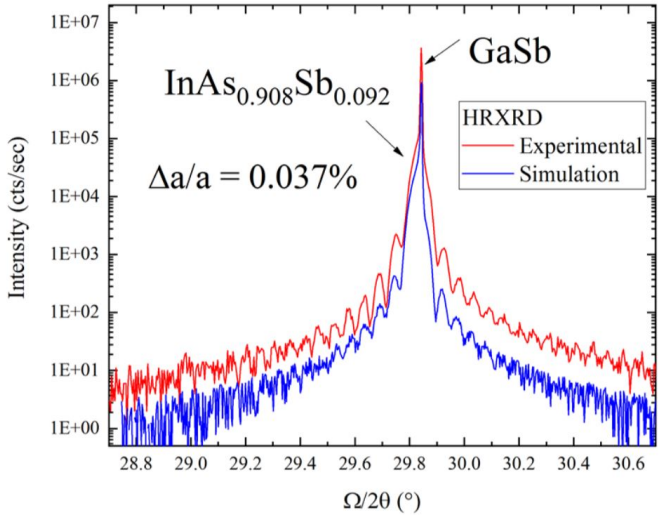

Figure 4.1.3.: High-resolution X-ray diffraction (HRXRD) of the InAsSb sample grown on GaSb substrate. Experiment data are in red whereas simulation data are in blue. The main XRD peak is from the GaSb substrate. The shoulder at a lower $\omega/2\vartheta$ angle of the GaSb peak is the $InAs_{0.908}Sb_{0.092}$ peak. $\Delta a/a$ corresponds to the lattice mismatch between GaSb and InAsSb.

Determination of the Drude model parameters

The dielectric function of the HDS was fitted before structuration from infrared reflectivity measurement. Figure 4.1.4shows the experimental data (scatter) and the model based on the transfer matrix method (red line). The model is in good agreement with the experimental data in the spectral range from 5 to 12.5 μm. The presence of a dip in the reflectivity gives access to the plasma frequency with a high precision as reported in the provided reference[34, 40].

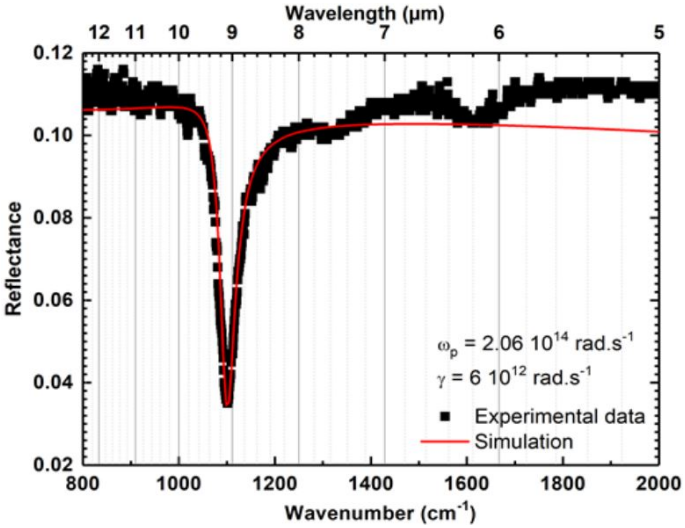

Figure 4.1.4.: The Brewster mode experiment corresponds to reflectance spectra in p-polarized light with an angle of incidence of 60°. The black scatters are the experimental data, the simulation (red line) is based on the transfer matrix method with the a Drude model to account for the InAsSb layer. The dip in the reflectance spectra is the Brewster mode which can be fitted to determine the plasma wavelength and the doping level via calibration experiments[40].

The dielectric permittivity $\varepsilon(\omega)$ of the HDSC gratings is well described by the Drude model (Equation 1.1.13) with $\varepsilon_\infty = 10.4$, which is weakly affected by doping. The parameters used for this simulation were a plasma frequency $\omega_p = (6.64 \pm 0.01) \times 10^{14}$ Hz (corresponds to a wavelength of 9.16 μm) directly obtained from the fitting of the Brewster mode measurements and a relaxation rate γ=$(6 \pm 2) \times 10^{12}\ s^{-1}$. The relaxation rate is

low compared to noble metal (few 10^{14} s^{-1}). The undoped GaSb substrate is satisfactorily accounted for by n_{GaSb}=3.77 on the investigated range.

Expected near-field signal

Figure 4.1.5 shows the real and imaginary part of the dielectric function given by Drude model. As can be seen, the imaginary part of the permittivity is small near the plasma frequency (about 0.24 at ω_p). The relatively good precision on ω_p and γ stems from the existence of the mentioned dip in the reflectivity spectrum for p-polarized wave at oblique incidence, corresponding to the Brewster mode occurring when ε is crossing zero. This leaky mode, which is clearly visible when the thickness is sufficient (here the thickness is 100nm), coincides with an absorption maxima that can be calculated from the retrieved ε, as also shown in Figure 4.1.5.

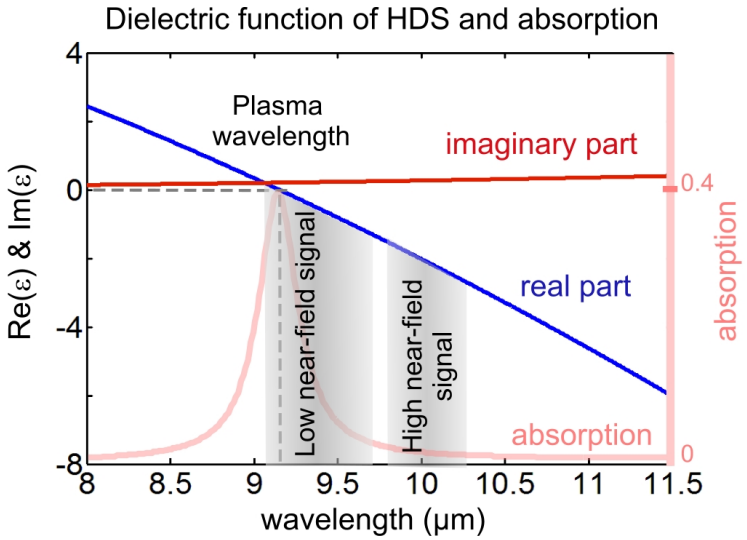

Figure 4.1.5.: Complex dielectric function ε(λ) of InAsSb obtained from IR reflectivity spectrum fitting, absorption of a thin NZE layer (t=100nm) determined from ε(λ) at p-polarized oblique incidence.

In Figure 4.1.5 we have indicate the low near field signal zone and high near field signal zone. As introduced in the previous chapter, the near field signal E_{scat} is proportional to the effective polarizability α_{eff} (Equation 2.3.9) which is function of the electrostatic Fresnel reflection coefficient β.

$$E_{scat} \propto \alpha_{eff\perp}(1+r_p)^2 E_0 \quad with\ \alpha_{eff\perp} = \frac{\alpha}{1-\frac{\alpha\beta K_c}{4h^3}}, \beta = \frac{\varepsilon_s - 1}{\varepsilon_s + 1} \tag{4.1.1}$$

- When the sample permittivity ε_s is near zero, r_p is close to -1: the reflected field is out of phase with the incident field. Thus there is no scattered signal at plasma wavelength and the near field signal is low.
- When ε_s reaches the small negative value (-1), then β is large and α_{eff} is near 0. Thus, near field signal is close to 0.
- When ε_s reaches the value where a LSPR mode could be excited (more negative), the local field is enhanced and the near field signal can be high.

Preliminary far-field analysis

A reflectance FTIR spectra of the HDSC gratings measured by the Nanomir team in Montpellier (IES) is shown in Figure 4.1.6. The Brewster mode appears clearly at 9.16 μm but the LSPR mode is hardly visible in this far field measurement. The dip related to the surface mode[3] is very shallow (less than 0.1% from the figure below). A very small peak can be guessed at 10.58 μm with an angle of incidence of 50°. In some other structures, notably more highly doped one, the simulated and experimental LSPR peak near plasma frequency is much more obvious (Figure 4.1.6 (b)), but they cannot be accessed by our current laser source. In Figure 4.1.6 (b), we can see a large peak at high wavelength, which corresponds to the surface mode at GaSb/HDSC interface (FDTD simulation is presented in the next chapter).

[3] $\omega_{SPP} = \frac{\omega_p}{\sqrt{\varepsilon_m + \frac{2}{\varepsilon_\infty}}}$, with ε_m is the permittivity of surrounding medium. $\varepsilon_m = 1$ for air and $\varepsilon_m = 3.77^2$ for GaSb.

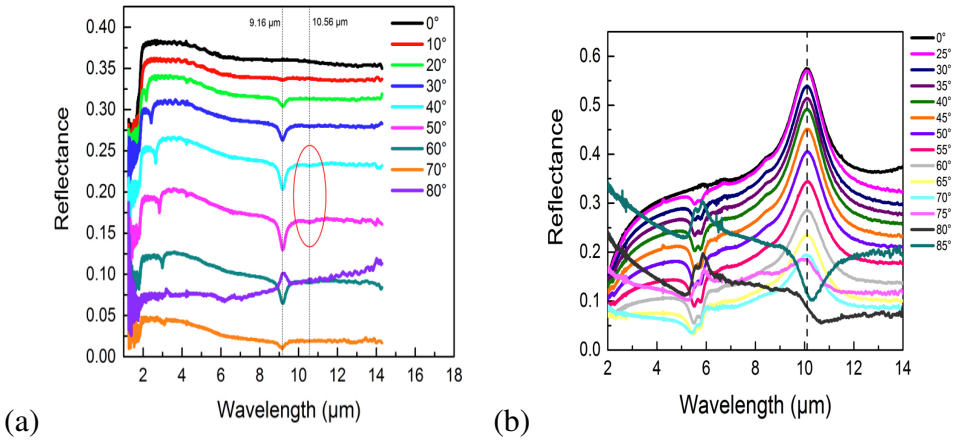

Figure 4.1.6.: Reflection FTIR spectra of HDSC gratings with different angles of incidence, provided by IES: (a) HDSC with ω_p=$(6.64 \pm 0.01) \times 10^{14}$ Hz; (b) HDSC grating with width 360 nm, pitch 500 nm and ω_p=$(1.2 \pm 0.01) \times 10^{15}$ Hz. For this second structure, the low energy LSPR peaks near 10 µm are located at the GaSb/HDSC interface (not directly accessible from air) .

FDTD simulation of reflectance and field distribution are presented in Figure 4.1.7. From the simulation we can see that the the field is confined at the top corners of the grating at 10 µm, the LSPR peak.

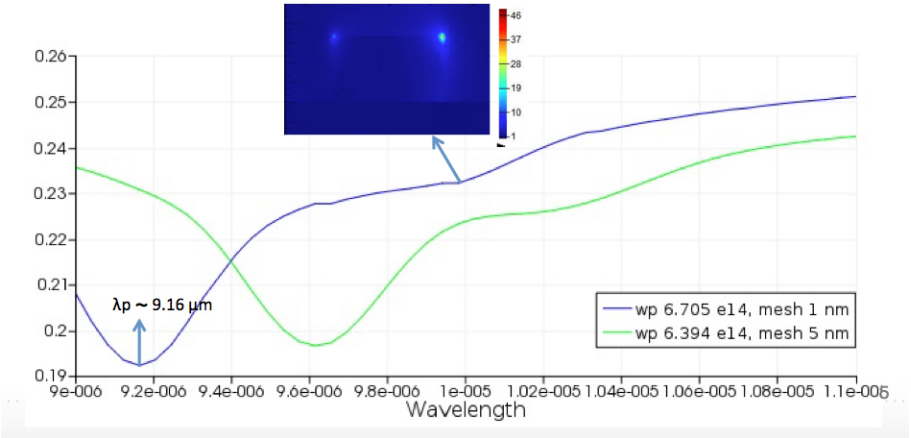

Figure 4.1.7.: FDTD simulation of the HDSC gratings reflectance. Different mesh sizes are tested to determine if the FDTD simulation converges. Inset: E field distribution at the LSPR mode frequency.

4.1.3. 2D periodic rectangular nanoantenna array

The 2D periodic rectangular nanoantenna array is shown in Figure 4.1.8. For this highly doped sample sample, the low energy LSPR mode occuring at the substrate/HDSC interface falls within the range of our tunable IR sources. The short axis of the rectangle is $400 \pm 30\,nm$ and long axis is $810 \pm 30\,nm$. The periodicity on short axis w_a is 1.4 μm and the periodicity on long axis w_b is 2 μm. We can see from the detail of the SEM image (Figure 4.1.8 (c)), that the corners of the rectangles are not sharp which made the rectangles to look like ellipses. The rounded corners are notably due to the proximity effects during the double lithographic exposure.

The dielectric function of this highly doped InAsSb 2D arrays can be modeled by Drude model (Equation 1.1.13) with parameters $\varepsilon_\infty = 10.4$, $\gamma = 1 \times 10^{13}\,s^{-1}$ and $\omega_p = 1.157 \times 10^{15}$ Hz (corresponds to a wavelength of 5.25 μm). A reflectance spectra of this sample is taken by a micro-FTIR shown in Figure 4.1.9. Compared with the spectra taken on the substrate GaSb plan, a weak reflectance peak at about 5.77 μm (1730 cm^{-1}) and a clear reflectance peak at about 11 μm (907.9 cm^{-1}) are observed under a detection polarization along short axis of the nanoantenna. This mode corresponds to the transverse LSPR mode associated with a field enhacement on both lateral sides of the nanoantenna. On the other hand, if the polarization of the incident light is along the long axis, the reflectance peak should be at longer wavelength[174].

LSPR modes can appear in two spectral regions. When the wavelength is near the plasma frequency, a high energy mode appear at the top corners of the structure, at the air/HDSC interface. Another resonance occurs at a lower frequency (low energy mode), where the LSPR is located mostly on the bottom corners, at GaSb/HDSC interface. The refraction index of GaSb is higher than that of air, from the expression of ω_{SPP} introduced in Chapter 1, this assignment is evident as the surface plasmon frequency is higher when refraction index of the surrounding medium is higher. More details on the field distribution is presented in the next chapter.

The reflectance spectrum shows that the low energy mode is located at about 11 μm, which is within the range of our laser source, thus the LSPR mode located at the bottoms corners can in principle be observed in s-SNOM images .

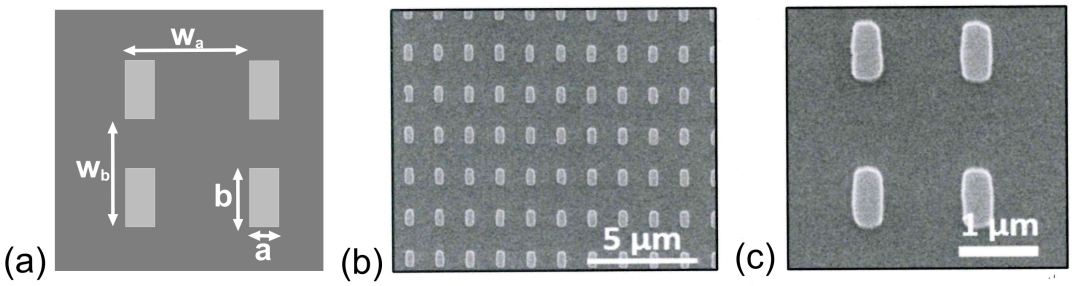

Figure 4.1.8.: 2D periodic nanoantenna array: (a) Scheme of the 2D array; (b) SEM image; (c) detail SEM image of (a), showing the round corners of the rectangular nanoantenna.[173]

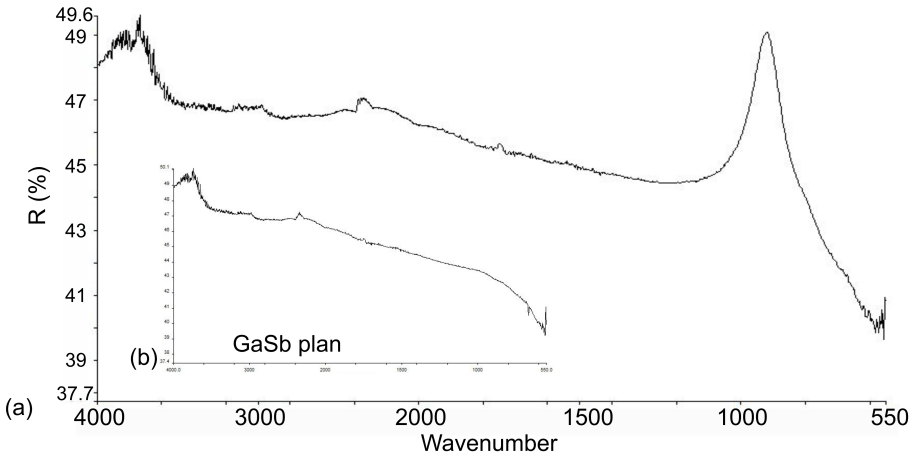

Figure 4.1.9.: (a)Micro-FTIR spectrum of the HDSC 2D array with polarization of detection along short axis; (b) Micro-FTIR on substrate GaSb plan.

4.2. Mid-IR nanoscopy: setups and experimental development

While information on samples can be obtained through near-field nanoscopy, using a known sample with a known dispersion (here provided by a Drude model) is also particularly interesting for comparing and benchmarking the near-field methods. When both

imaging and spectroscopy are performed, the recorded data are usually referred to as hyperspectral images, whatever the technique (PiFM, SNOM, or others). In our case, tunable infrared sources where used to perform the spectroscopic analysis. Theoretically, the two spectroscopic approaches both rely on the probe-sample interaction with light. Experimentally also, they are both based on atomic force microscope, typically operating in tapping mode. In order to achieve nanoscopic investigation of HDSC structures through near field imaging, specific setups must be used or built. In this section, we describe these optical systems.

4.2.1. s-SNOM

In our experiment, we used a home-built phase-sensitive mid-IR s-SNOM, mostly developed during the thesis of Z. Sedaghat, with the help of a CO_2 laser. Later on, a specific extraction method was also developed during the thesis work of A. Al Mohtar, and tunable infrared lasers were added. Few changes were also performed during our work. Mostly, a third QCL was added and we decided to use mid-IR fibers to convey the light to the microscope, in order to switch more easily between laser sources so as to obtain a spectrum from 9.1 µm to 11.4 µm. In the following, probe fabrication details are given and the general optical setup is presented including the phase-sensitive detection method.

4.2.1.1. Probe fabrication

Since s-SNOM investigates a nanoprobe-sample interaction, the size of the probe is the key factor. Obtaining a sharp probe is a very important starting point for the experiment. A priori, this is especially the case for tuning-fork based tapping mode, as in our case. Indeed, in such AFM mode, the probe amplitude is typically in the order of *few nanometers* only. To obtain a sufficient signal modulation, the confined light decay from the probe must be roughly of the same order, therefore probes with a radius bigger than 25 nm rarely provide any noticeable signal in our case.

An electrochemically etching method, the "double lamellae dropoff technique"[175], was used for probe fabrication. Z. Sedaghat has conducted a first parametric study in order to find the optimum conditions to obtain the required probe-diameter[149]. In this thesis

work, 125 µm diameter tungsten wires from Goodfellow are used for the etching. Before etching, the tungsten wire is cleaned with first acetone and then IPA and finally bathed in oxalic acid for a while to increase the uniformity during the reaction. Then a 2 cm long tungsten wire is glued to a commercial AFM tuning fork. The etching setup is sketched in Figure 4.2.1 (a).

A meniscus of NaOH solution is hold within a 5 mm gold ring that is horizontally fixed above the solution (2.5 mol/L NaOH) in the beaker. The tungsten wire goes through the center of the ring till it reaches the solution surface. The distance between the ring and the surface of the solution in the beaker is about 1.5 cm and about 5 mm of tungsten wire goes into the NaOH solution in the beaker. The amount of liquid inside the ring is an important factor because it affects the current for etching when the concentration of NaOH is fixed. The liquid inside the ring can be suck out with optical paper in order to set the correct starting current (about 3.0 mA), passing through the tungsten wire, in order to produce tips with thinest apex. For the considered ring size, the required voltage is about 8.0 V, the typical duration of the etching process is about 4 to 5 minutes. When the etching process is completed, the tungsten tip is formed and the bottom part of the wire is cut. The nice aspect of this setup is that the current automatically drops to zero as the circuit becomes open when wire is cut.

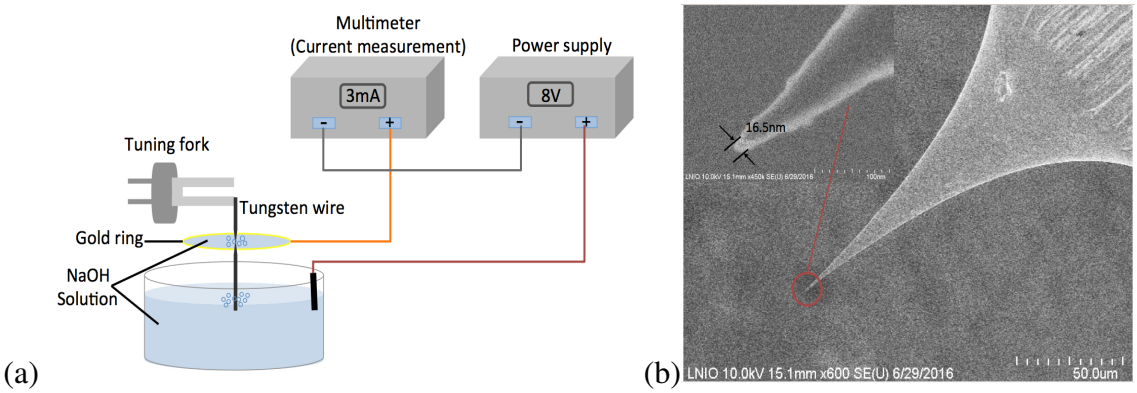

(a) (b)

Figure 4.2.1.: Probe fabrication: (a) Schematic diagram of electrochemical etching setup; (b) SEM images of etched probe.

This probe fabrication method is quite reproducible if well respected. Figure 4.2.1 (b) shows a SEM image of an etched probe. As we can see, the tip shape is symmetric and

the tip end diameter is less than 30 nm, and can be in the order of 10 nm (From SEM measurement) in the best cases. The absence of cantilever within the IR collection spot is useful to reduce eventual background light modulation and the ultra-small oscillation amplitudes (few nm) of the probe also filter further the background.

4.2.1.2. Generalized lock-in (GLIA) detection

As we mentioned before, the background signal is one of the major drawbacks in s-SNOM measurement. In our home-built s-SNOM, we use a special interferometric detection method called generalized lock-in (GLIA) detection. The method can extract amplitude and phase from an optical interferometer when an arbitrary periodic phase or frequency modulation is used. This approach has been applied to phase sensitive spectroscopy and near-field optical measurements[146].

The detection is based on a Michelson interferometer (Figure 4.2.2): the SNOM head including the mirror objective lens is inside the "signal" arm, while a phase modulation is created in the reference arm comprises a piezo-actuated mirror (in practice two piezo actuated piezo are used to reduce the spatial modulation and increase the speed).

If the signal arm is not modulated by the tuning fork, the reference field is modulated by the reference mirror and the phase of this signal is ϕ_R. The intensity of the interference signal is:

$$I_{det} \propto E_S^2 + E_R^2 + 2E_R E_S cos(\phi_S - \phi_R) \tag{4.2.1}$$

where the fringe contrast is considered to be 1 without loss of generality. To extract the phase and amplitude of the signal field, we multiply the detected signal with two orthogonal reference signals $cos\phi_R$ and $sin\phi_R$ in which ϕ_R is determined by the modulation function of the reference signal. Then we do an integral over a sufficient time and we get two terms that contain the information of E_S and ϕ_S .

$$X = \frac{1}{\Omega t_{int}} \int_0^{\Omega t_{int}} I_{det} cos\phi_R d\Omega t \propto E_S cos\phi_S \tag{4.2.2}$$

$$Y = \frac{1}{\Omega t_{int}} \int_0^{\Omega t_{int}} I_{det} sin\phi_R d\Omega t \propto E_S sin\phi_S \tag{4.2.3}$$

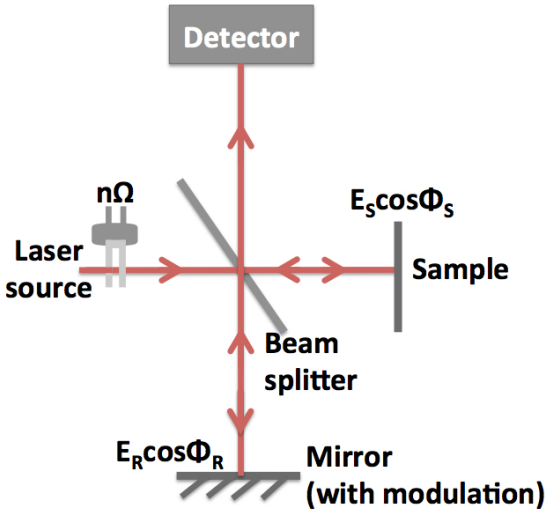

Figure 4.2.2.: Michelson interferometer system used for GLIA detection. In s-SNOM, the signal from the sample is modulated by the tip (glued on tuning fork) at its operating frequency $n\Omega$. A movable reference mirror is used for GLIA detection with a modulation frequency of Ω.

The modulation of the reference mirror is here sinusoidal $\phi_R = asin(\Omega t)$, where a is the modulation depth, because such signal can excite a piezo at a much higher fundamental frequency than a sawtooth signal (*serrodyne detection*), although the processing is more complex with a sine modulation. In our case, the amplitude of the signal field will be modulated at Ω_{probe} because of the dither of the AFM tuning fork probe. This frequency is usually more than 10 times the reference mirror frequency Ω , and we note $\Omega_{probe} = n\Omega$, where n is not an integer. Then the scattered signal will be represented as $\tilde{E}_S = \sqrt{2}E_S cos(\phi_S + \omega t)cos(n\Omega t)$. The detected intensity is then:

$$I_{det} = \tilde{E}_S^2 + E_R^2 + \tilde{E}_S^2 cos^2(n\Omega t) + 2E_R\tilde{E}_S cos(\phi_S - \phi_R)cos(n\Omega t) \tag{4.2.4}$$

As before, we multiply I_{det} by two orthogonal reference signals $C(t) = 2cos(n\Omega t)cos\Phi_R$ and $C(t) = 2cos(n\Omega t)sin\Phi_R$ and then integrate. After some algebra, Equation 4.2.2 and Equation 4.2.3 will turn to

$$X_{(n\Omega t \pm asin(\Omega t))}(I_{det}) = E_R E_S cos\phi_S (1 + J_{2n}(2a) + J_0(2a)) \tag{4.2.5}$$

$$Y_{(n\Omega t \pm asin(\Omega t))}(I_{det}) = E_R E_S sin\phi_S (1 + J_{2n}(2a) - J_0(2a)) \tag{4.2.6}$$

where $J_k(a)$ is the k-th order of Bessel function.

However, a (not modulated) background field coming from the collection spot is usually detected in addition to the modulated signal from the sharp probe. The background field, originating from the same spot than the signal, is interfering with the signal on the detector creating a modulated intensity term at the tip fundamental frequency or harmonics (harmonics are negligible if the amplitude is ultra small, so that the modulation is nearly a pure sine)[146, 176]. If we evaluate the contribution of this term by multiplying $C(t)$ and $S(t)$ and then integrating, we see that these two integrals are proportional to $J_{2n}(a) + J_0(a)$. As is known that $J_{2n}(a)$ and $J_{2n}(2a)$ are extremely small when n is large (it is usually about 30 in our case), these terms are relatively negligible. In addition, by setting the amplitude modulation of the reference signal a to a zero of 0^{th} Bessel function we can make sure that $J_0(a)$ is zero.

It is concluded that in order to efficiently suppress the unwanted background light with a GLIA method, it is important to choose the voltage of the reference modulation such that the phase modulation depth is $a = 2.4048\,rad$ (i.e. $J_0(a) = 0$). Then the X, and Y components of generalized lock-in detection are:

$$X_{(n\Omega t \pm asin(\Omega t))}(I_{det}) = k_X E_R E_S cos\phi_S \quad with \quad k_X = 1 + J_0(2a) \tag{4.2.7}$$

$$Y_{(n\Omega t \pm asin(\Omega t))}(I_{det}) = k_Y E_R E_S sin\phi_S \quad with \quad k_Y = 1 - J_0(2a) \tag{4.2.8}$$

From equation 4.2.7 and equation 4.2.8, the amplitude and the phase of the scattering signal can then be determined.

To go further, we must now consider that in our s-SNOM experiment, the amplitude of the signal is modulated as we mentioned above. This modulation is due to the tip oscillation at the frequency $n\Omega$ and we consider that it is proportional to $cos(n\Omega t)$. This function is related to the drive signal of the probe. However, usually a phase shift is existing between the drive signal and the actual motion of the probe excited near its mechanical resonance. To solve this issue, the first method is to measure the actual probe motion directly by the four quadrant photodiode for commercial cantilever AFM probes and then to replace the driving signal by this normalized signal in the calculation. Another approach called double GLIA can be performed for our home-built AFM head that uses tuning fork probe without quadrant photodiode. Simply speaking, double GLIA is adding a second reference $sin(n\Omega t)$ amplitude modulation to the standard GLIA reference $cos(n\Omega t)$.

We represent the full signal field which contains the near field information as $E_S(t) = E_S^{full}(t)cos(\omega t + \phi_S)$, where the general expression of the modulated amplitude is $E_S^{full}(t) = cte + E_S cos(n\Omega + \psi) + harmonics$. ψ is the phase shift between the driving signal in phase with $cos(n\Omega t)$ and the term $E_s cos(n\Omega t + \psi)$. Without knowing ψ, the double GLIA method can extract (E_S, φ_S) by applying twice the GLIA as follow:

$$X = \int_0^{t_{max}} I_{det} cos(n\Omega t) cos(\phi_R) dt \quad and \quad Y = \int_0^{t_{max}} I_{det} cos(n\Omega t) sin(\phi_R) dt \tag{4.2.9}$$

$$X' = \int_0^{t_{max}} I_{det} sin(n\Omega t) cos(\phi_R) dt \quad and \quad Y' = \int_0^{t_{max}} I_{det} sin(n\Omega t) sin(\phi_R) dt \tag{4.2.10}$$

After calculation of Equation 4.2.9 and Equation 4.2.10, we can obtain:

$$X = k_X E_R E_S cos(\psi) cos(\phi_S) \quad and \quad Y = k_Y E_R E_S cos(\psi) sin(\phi_S) \tag{4.2.11}$$

$$X' = -k_X E_R E_S sin(\psi) cos(\phi_S) \quad and \quad Y' = k_Y E_R E_S sin(\psi) sin(\phi_S) \tag{4.2.12}$$

Here, $k_X = 1 + J_{2n}(2a)$ and $k_Y = 1 - J_{2n}(2a)$. We choose a modulation $a = 2.4048 rad$ as explained above. With these four outputs, not only near field amplitude E_S and phase φ_S can be calculated, but also the phase shift ψ can be determined.

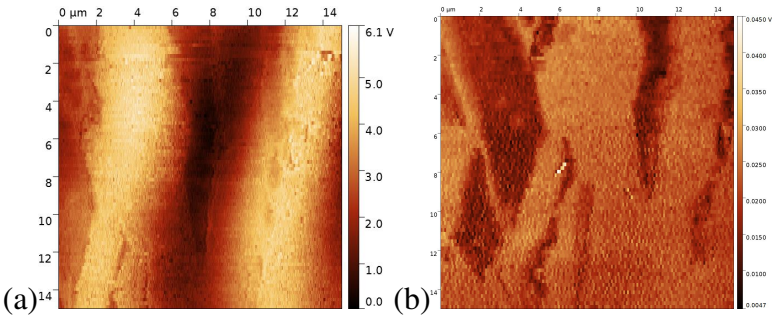

Figure 4.2.3.: Comparison of s-SNOM optical amplitude image of graphene using first harmonic lock-in detection and GLIA: (a) Lock-in detection at first probe harmonic, without interferometer; (b) double GLIA detection with interferometer. From these two images we can see the background suppression induced by the GLIA.

The double GLIA detection approach used in our s-SNOM experiment provides a higher signal to noise ratio and is useful in low signal SNOM experiments[146, 176]. This modified lock-in detection method can explore both field amplitude and phase information and suppress the background signal efficiently, as shown in Figure 4.2.3. The two images are the optical amplitude of broken flakes of single-layer graphene. We can see that with a standard lock-in amplifier without interferometry, the amplitude of graphene in Figure 4.2.3 (a) is buried in the background. The presence of a background light is obvious from the presence of vertical fringes. This background fringes have been discussed elsewhere in the case of s-SNOM operating in visible or NIR wavelength. Their orientation and pitch depend on the illumination and collection direction and can be easily simulated[177]. On the other hand, with the double GLIA detection (Figure 4.2.3 (b)), the amplitude image is more evident and background free.

Approach curves are taken at different probe oscillation amplitudes shown in Figure 4.2.4(a). These approach curves were taken at 11 µm with the fabricated probe[4] above HDSC gratings. The probe oscillation amplitude is stronger with higher drive voltage of

[4] A tungsten probe glued on tuning fork was used. The diameter of the probe apex is about 40 nm.

the tuning fork. The noise level of the optical amplitude is about 0.002 which is caused by the amplifier of the detector. The near field signal rises exponentially when the probe is engaged on the sample. The strongest signal increase is found at a drive voltage of 20 mV, the signal increase about 10 times and this exponential rise happens only when the probe is engaged, which indicates that the signal comes from a modulated near field scattering.

A reconstructed approach curve[178] was previously obtained on a similar setup on polymer/gold gratings[5]. This signal level is expected from the dipole model, neglecting probe modulation and lock-in detection (otherwise constant signal should be 0 far from the sample). To explain this behavior, the external field must have a mostly linear variation (not constant as we consider usually, or evanescent as consider by others e.g. in PiFM).

[5]The refractive index of the polymer is close to 1 at the considered wavelength. The diameter of the tungsten probe is about 40 nm.

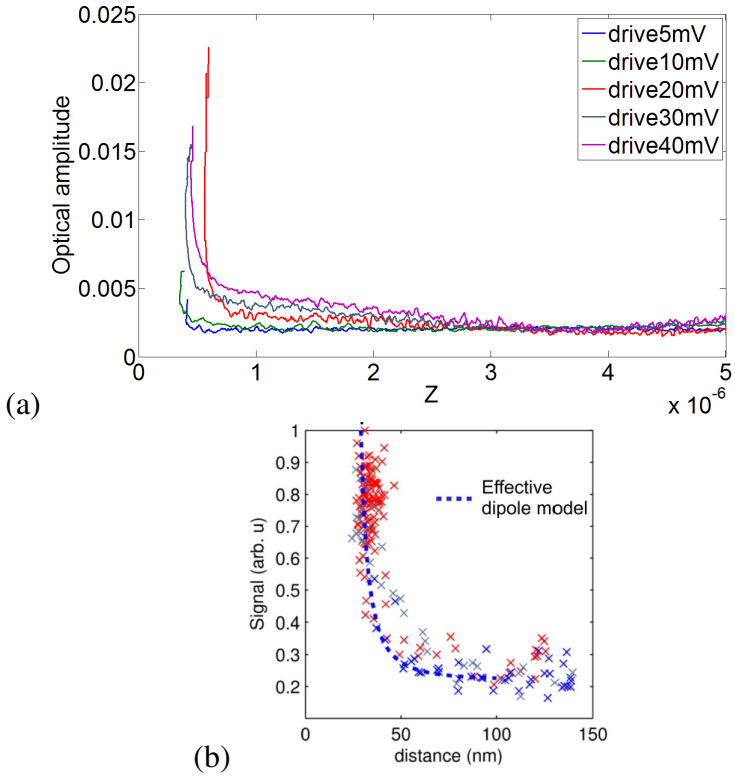

Figure 4.2.4.: Approach curve of s-SNOM: (a) Approach curve of s-SNOM at different probe oscillation amplitude, taken at 11 μm with probe above HDSC gratings; (b) Reconstructed approach curve on polymer/gold grating, adapted from[178].

4.2.1.3. Optical setup of the s-SNOM

Figure 4.2.6 shows our home-built s-SNOM system. The setup is operated in mid-IR range, while for practical reasons we use a He-Ne laser coupled into a single mode fiber to do a first alignment. We use a protected silver reflective collimator which is suitable for wavelengths ranging from 450 nm to 20 μm, therefore, the mid-IR laser out of the collimator goes through the same path as the 633 nm red laser. For our spectroscopic experiments, three tunable Quantum Cascade Lasers (QCL) from Daylight Solutions are used (shown in Figure 4.2.5). The spectral range of the three QCLs are 9.05 μm to 9.69 μm, 9.48 μm to 10.47 μm and 10.4 μm to 11.51 μm respectively. As is known that QCLs are extremely

sensitive to optical feedback, the mid-IR beam passes through an added optical isolator before being coupled into the mid-IR hollow fiber.

Figure 4.2.5.: A photo of mid-IR laser sources used in s-SNOM.

A half-wave plate is also positioned after the hollow fiber to get a laser polarization mostly along the probe axis. The waveplate can also be placed before the fiber coupler. A visible camera is necessary for aligning the red laser focused on the sample at the apex of the tip. The objective[6] is used to focus light on the sample and to collect the back-scattered fields. Our AFM head can be freely rotated to change the incident angle. In our experiment the mean incident angle can be typically varied from 45º to about 60º from the normal. The power of the source out of the fiber is about 7mW.

The probe we are using is our home etched tungsten tip (details are given in subsection 4.2.1.1) attached on commercial AFM tuning fork. To excite the probe, an electric excitation is supplied by a phase-locked loop (from Nanonis inc.) and an additional feedback loop enables to keep a constant amplitude. To scan the sample during the measurement, 3D-piezoelectric actuators are used with respect to the tip which is fixed in the focus point of the objective. As mentioned already, we are working on AFM tapping mode based on a tuning fork (no cantilever).

[6]Reflective Microscope Objective (reverse Casegrain) is used in the setup[179].

A liquid nitrogen cooled HgCdTe detector (from Teledyne Judson Inc.) is used to detect the signal and to send the photocurrent to an acquisition card. The double GLIA detection (details in subsection 4.2.1.2) is realized by a Labview code to extract the amplitude and phase from the scattered signal. Both topography and optical amplitude and phase images are obtained simultaneously during the scan.

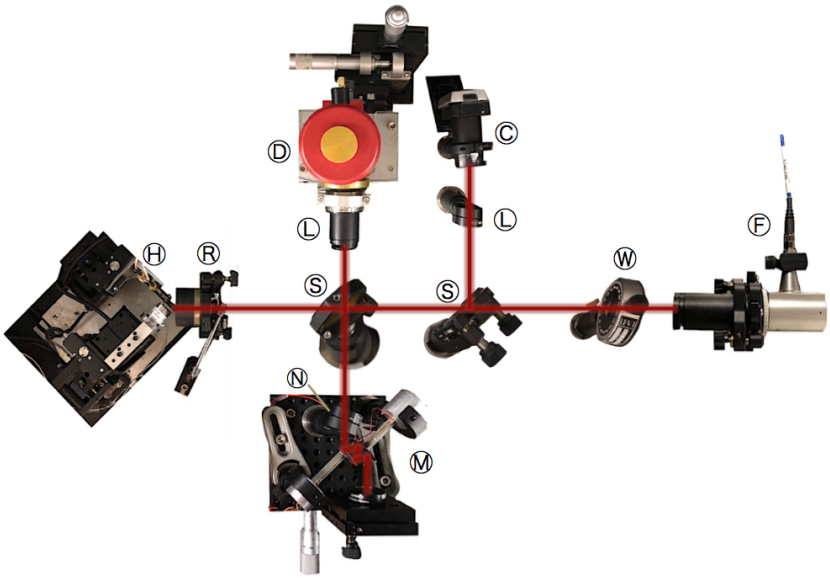

Figure 4.2.6.: s-SNOM home-built setup: F: Mid-IR fiber with collimator; W: Half wave-plate; C: visible camera; L: Lens; S: beam splitter; D: HgCdTe detector; R: Reflective objective; H: Tuning-fork based AFM head comprising motors and piezos stages; ND: Neutral density filter; M: Mirror mounted on piezo-actuators.

4.2.2. PiFM setup

To measure the photo-induced force with a probe, PiFM uses near-field mechanical detection. As a commercial system, AFM cantilever probes are used. Because we do not have pulsed laser source, the PiFM shares the same laser source with the s-SNOM presented before. In the following, the general optical setup of PiFM is experimentally.

4.2.2.1. PiFM detection mechanism

We have a commercial PiFM system[160] which use two separate lock-in amplifiers to collect the data of topography at f_m and the data of the photo-induced force gradient at f_0 simultaneously. In order to prevent less-local scattering forces to impact the PiFM signal, we usually work with the side-band coupling mode[25] of PiFM, as detailed hereafter.

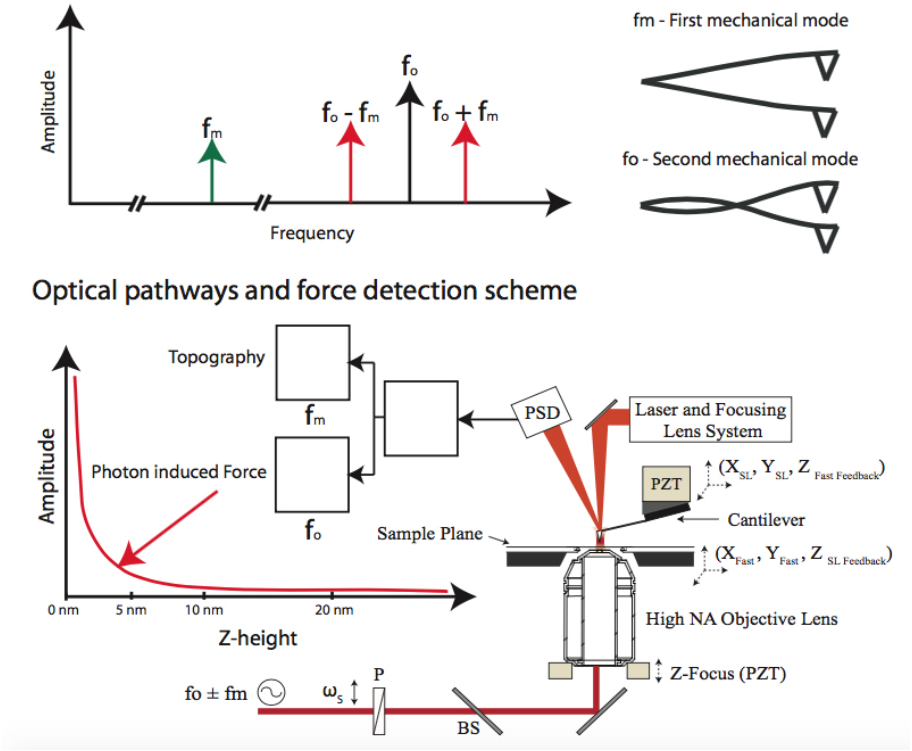

Figure 4.2.7.: PiFM force detection schema (adapted from[160]).

The side-band coupling mode described in[25] was used in PiFM measurement (shown in Figure 4.2.7). The AFM cantilever probe has more than one mechanical resonance, here we use the first mechanical resonance f_m and the second mechanical resonance f_0 (about 6 times of f_m). The resonance of the cantilever f_m is around 300 kHz and its second mechanical resonance f_0 is around 1.8 MHz. In our experiment, AFM is working on tapping mode at the the second mechanical resonance frequency f_0. The light pulses are triggered at a frequency of $f = f_0 - f_m$ instead of a direct excitation at f_m. Then, due to the influence of the interaction between sample and probe, the photo-induced force can be detected at the

frequency of f_m. The selection of this laser modulation frequency is to take advantage of the quality factor Q of the cantilever, in order to enhance the sensitivity to the optical force.

Another direct detection mode is also available for PiFM measurement, which use a direct excitation of the light and detection at the same frequency. In our experiment, we use the second mechanical mode for topography. The higher spring constant for the second mode allows for a lower dither amplitude providing the cantilever more time to measure the short range PiFM signal. Moreover, using the softer 1st mechanical mode the cantilever creates a more sensitive condition for the PiFM detection.

4.2.2.2. Home-made setup for laser modulation

For PiFM, a strong and high frequency modulation of the laser intensity is necessary. Thus, the use of a tunable pulsed laser is recommended. For mid-IR spectroscopy, the VistaScope from Molecular Vista Inc. can be coupled with a widely tunable pulsed (power-modulated) Mid-Infrared Quantum Cascade Laser source from Block-engineering ranging from 5.4 μm to about 12.8 μm. An average laser power of 1 mW is used at the sample surface.

However, we do not have such unique pulsed mid-IR source in our laboratory, only tunable continuous-wave QCLs that are more widely spread in laboratories, typically for gas spectroscopy. For such QCL (from Daylight solution), the intensity can however be modulated by a current modulation. It is found however, that at frequency beyond 100kHz, the modulation depth is really too small for PiFM measurement, less than 5%. While the required modulation frequency of the laser is about 300 kHz if we work with direct detection mode because of the resonance (around 300 kHz) of the used cantilever[7].

To solve this issue, we decided to add a strongly unbalanced interferometer just before the optical isolator. In that way, a minute change in wavelength entails a clear phase-shift, between the two arms. This effect can be used to modulated on and off the intensity by passing from constructive to destructive interferences.

The two setups (unbalanced interferometers) developed in this thesis are schematically shown in Figure 4.2.8. They consist in a horizontal interferometer and a vertical one. The two orientations were chosen to optimize the intensity ratio between the two arms, depending on the laser polarization direction.

[7]NCH-Au 300 kHz noncontact cantilevers from Nanosensors is used in our experiment.

Given the extremely limited wavelength change, a large path difference as big than about one meter is actually needed for the biggest achievable current modulation. Because, our IR detector cut the DC frequency, an optical chopper was added to determine unambiguously the actual modulation depth achieved with such interferometer. As we can see from Figure 4.2.8 (c), after the interferometer system, the modulation depth rate can be increased to about 80% when the modulation frequency of the laser reaches 200 kHz. Modulation depth at 300 kHz could not be checked with the oscilloscope because the detected signal of HgCdTe detector is limited to 200 kHz. However, the intensity modulation depth variation from 100 kHz to 200 kHz was relatively small (about 5%). So we assumed that modulation up to 300 kHz is achievable with our system required for the PiFM measurement.

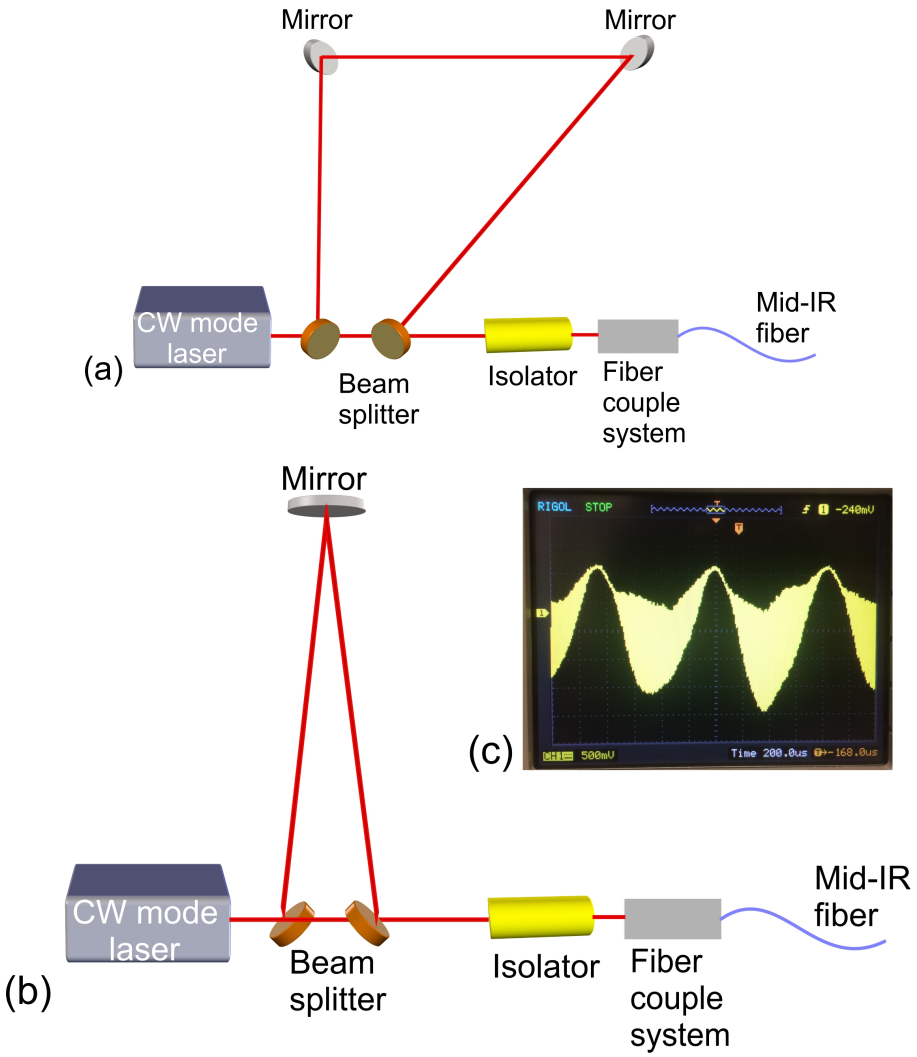

Figure 4.2.8.: Scheme of the two interferometer systems added to the laser: (a) scheme of the horizontal system (the mirrors are in the plane of the horizontal breadboard); (b) scheme of the vertical system (the upper mirror is at height of about 50 cm above the optical breadboard); (c) modulation depth of the laser intensity after the mid-IR fiber.

Both configurations are used in our PiFM measurement, shown in Figure 4.2.9. The horizontal system which is on the optical breadboard is more stable compared to the vertical system but it occupies larger space on the table which makes it not practical when the space

is limited. This configuration allows us to use CW mode laser to have a decent modulation to do PiFM experiments without purchasing another expensive pulsed laser.

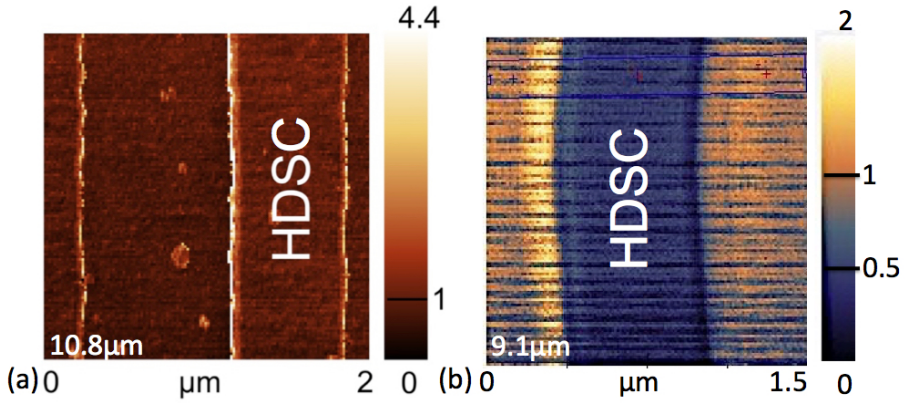

Figure 4.2.9.: PiFM image with modified laser system: (a) PiFM image with horizontal system at 10.8 µm (modified CW mode QCL ranging from 10.4 µm to 11.51 µm); (b) PiFM image with vertical system at 9.1 µm (modified CW mode QCL ranging from 9.05 µm to 9.69 µm).

4.2.2.3. Experimental setup

PiFM can be used to image transparent samples by bottom illumination as well as opaque samples by top illumination. The similar part between s-SNOM and PiFM is that, in both techniques, we need to focus light on the apex of the probe. So for different samples, the excitation source was focused either by a parabolic mirror or by an objective lens, shown in Figure 4.2.10. The two optical paths allow PiFM to work on two modes: transmission mode and reflection mode.

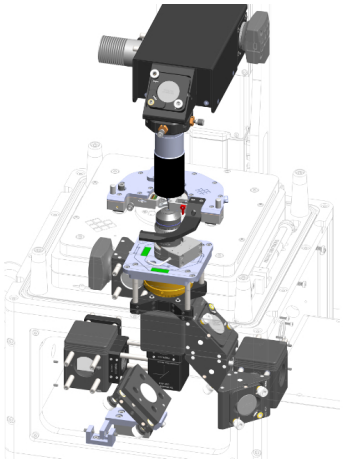

Figure 4.2.10.: Drawing of focusing path of PiFM (adapted from[160]).

Transmission mode (first tests)

When a transparent sample is studied by PiFM, the laser can be focused through a high NA objective (both dry objective and oil immersion objective can be used). The alignment of optical path in PiFM is as critical as s-SNOM. Similarly, the most important step is to put the tip apex exactly in the focused laser spot. Using a thin slide cover glass, we are able to image the focused laser spot with PiFM, as we mentioned in chapter 3.

A 3D scanning stage for the objective lens is used to image the laser spot by PiFM, shown in Figure 4.2.11 (a). It allows high speed scan to find the focusing position and the risk of tip damage during the probe alignment is low. As shown in Figure 4.2.11 (b), the laser spot can be imaged by PiFM. Here, we use a fiber-pigtailed laser diodes (wavelength 633 nm from Thorlabs) focused on a thin slide cover glass by a 1.45 NA oil immersion objective lens.

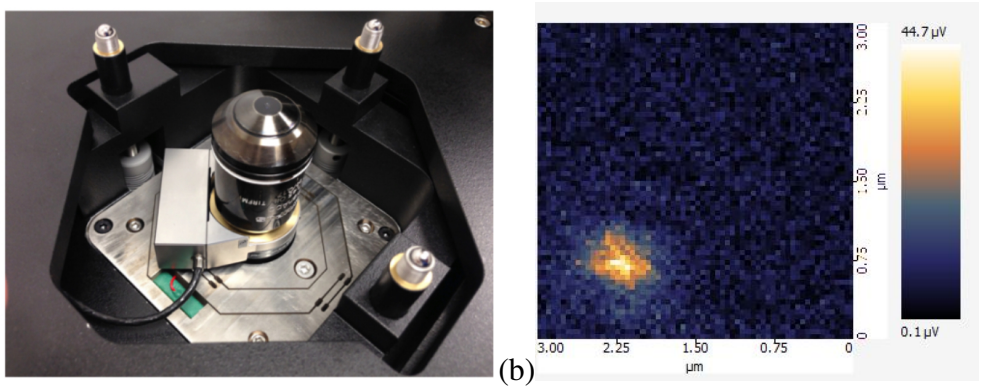

Figure 4.2.11.: Visible PiFM with objective scan: (a) inverted objective lens with 3D scanning stage; (b) laser spot imaging with PiFM.

With a high quality probe and a well-polarized laser, we can observe the z component of the laser spot, shown in Figure 4.2.12. When the polarization of the laser is rotated by 90°, the direction of the z lobe[8] of the PiFM image rotate along with polarization (Figures 4.2.12 (a-b)). Since photo-induced force is proportional to d^4 between the tip and the sample, it is better for the probe to have a small dither amplitude and to stay very close to the sample.

The quality of the tip also influences the signal of photo-induced force. Usually a tip with strong second mechanical resonance exhibits more signal. With force versus distance plotting (approach curve), we can clearly see the relationship between photo-induced force and the distance between tip and sample (Figure 4.2.12 (e)). In the force versus distance curve, x axis shows the movement of the tip while y axis is the PiFM signal. The tip goes down 5 *nm* from its current position (engaged position with 85% setpoint) and then goes up until 20 *nm* higher than the current position. From the approach curve we can tell that the signal increases rapidly when the tip is approached to the sample surface.

Then we did two series of scans. Series A is taken when the tip is 8 nm higher than the original engaged position (Figures 4.2.12 (a) and (b)), while series B is taken when the tip is 3 nm lower than the original engaged position (Figures 4.2.12 (c) and (d)). As can be seen, the signal in series B is about 12 times stronger than that of the series A, which shows that the distance between sample and probe markedly affects the PiF signal.

[8] z lobe is the shape of z component of E field distribution of a tightly focused (by objective lens) laser spot.

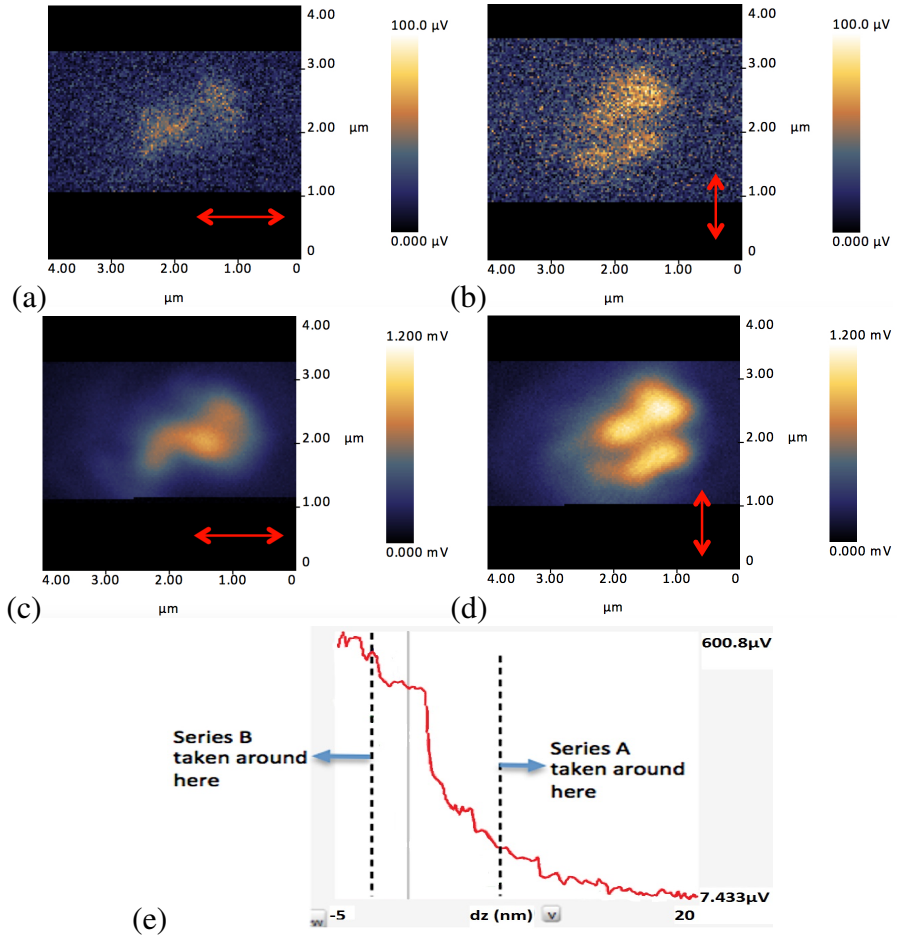

Figure 4.2.12.: z component imaging of the laser spot in PiFM: (a-b) series A, laser polarization horizontal and vertical respectively; (c-d) series B, laser polarization horizontal and vertical respectively; (e) force vs. distance curve. The laser wavelength is 642 nm, using side-band detection mode. This measurement is helpful for PiFM alignment.

The alignment of PiFM in transmission mode is relatively direct owing to the bottom camera view. After obtaining the best focused laser spot image by adjusting the distance between the objective lens and the sample, we transfer the objective lens to the center of the spot where the PiF is the strongest. Then, a transparent sample can be installed and a normal AFM scan in tapping mode can be started. The laser spot (from objective lens) and the tip stay fixed and the sample scanner moves to complete the scan to obtain the PiF image.

As shown in Figure 4.2.13, a transparent sample of gold nanoplates (diameter of 130 nm and height of 30 nm) is imaged by PiFM transmission mode. The gold nanoplates are randomly distributed on the glass substrate. The absorption resonance of the LSPP (Localized surface plasmon polaritons) sample is around 647 nm and relatively monodispersed.

The PiFM images (Figures 4.2.13 (b) and (e)) are obtained in transmission mode while the s-SNOM is collected by a photodetector in the side illumination optical system through the parabolic mirror beside the probe and the s-SNOM images (Figures 4.2.13 (c) and (f)) are obtained without interferometry but via a lock-in amplifier at second harmonic of the probe. These first simultaneous SNOM/PiFM measurement were made during a few months stay at Molecular Vista, just before the PiFM acquisition.

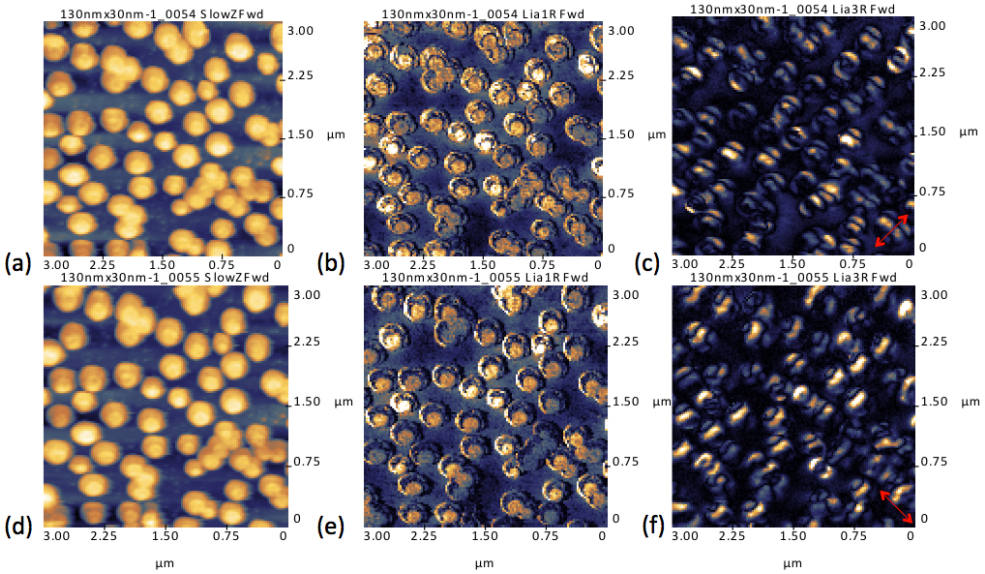

Figure 4.2.13.: PiFM images by transmission mode and s-SNOM signal collection from top: (a)(d) topography; (b)(e) scattered signal collection from the top; (c)(f) PiFM image; (a)-(c) and (b)-(f) have different polarizations indicated by the red arrows.

The PiFM images shows bright nanoplates with a bright ring form at the edge of the plate, which is similar as the PiFM image shown in Figure 3.1.4. With the rotation of the polarization, PiFM images does not show significant differences as much as expected from literature like Tumkur et al.[165]. We suppose the reason is that the scanning probe is not “super sharp” so that the nanodisks appear to be bigger in the topography than its real

size. Similarly, the probe size may affect the sensitivity of the PiF signal. Furthermore, the nanoplates are gathered together and the the sizes of the plates still have some dispersions.

Reflection mode

Transmission mode is not very versatile for near field investigation because many samples are opaque. In order to use PiFM on opaque samples, side illumination optical system is designed by attaching a parabolic mirror in the AFM head (Figure 4.2.14 (b)). This reflection mode can be used to do s-SNOM as well when an extra detector is added (Figure 4.2.14 (a)). In our mid-IR experiment, we mainly use reflection mode as it is achromatic.

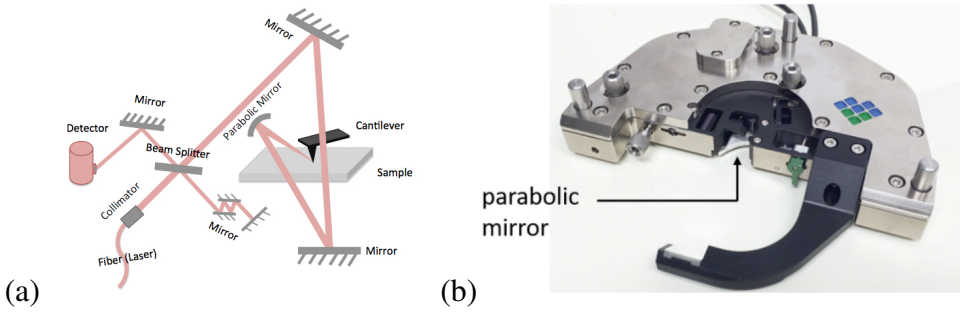

(a) (b)

Figure 4.2.14.: Side illumination system used for reflection mode: (a) Illumination scheme; (b)AFM head with integrated parabolic mirror.

The parabolic mirror is used for both focusing light on the sample and collecting light reflected from the sample.There is a 3D piezo stage attached on the parabolic mirror in order to adjust the focusing position. As the 3D scanning stage of the objective lens in the bottom, a parabolic mirror scan is available to achieve a more accurate alignment since the position of the focusing spot is quite critical.

Alignment procedure

Since our sources are in the mid-IR, it is not possible to have a direct vision of the whole optical path with our eyes. Usually a guide laser (visible light, here we use 633 nm laser) is used to help with the initial alignment. The focused red spot is seen by the camera shown as Figure 4.2.15 (a). With parabolic mirror scan we can get a PiFM image in Figure 4.2.15 (b). After seeing the laser spot of the guide laser, we can install the sample and mid-IR

laser. If a large parabolic mirror scan is implemented, we are supposed to see a mid-IR laser spot as is shown in Figure 4.2.15 (c). The alignment of PiFM in reflection mode is completed when the parabolic mirror is placed at the brightest spot.

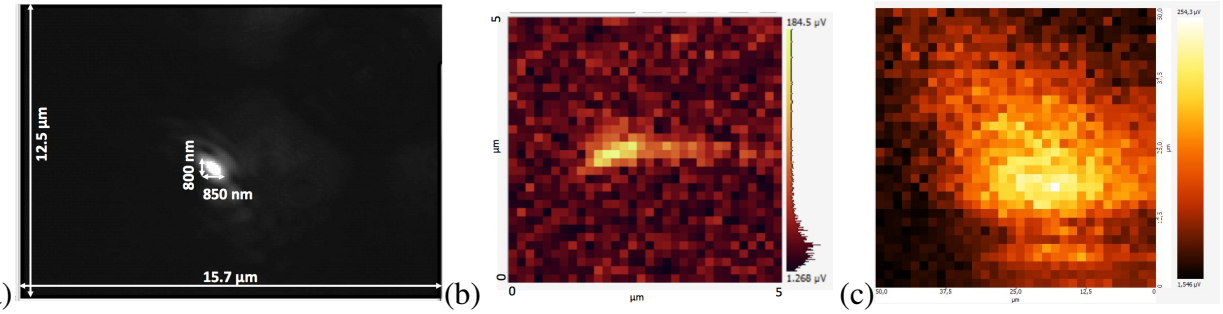

Figure 4.2.15.: Laser spot imaging in reflection mode: (a) camera view of the focused spot by parabolic mirror (633 nm); (b) PiFM image (633 nm); (c) PiFM image (5780 nm, image from MolecularVista).

4.3. Conclusion

In conclusion, details of the experiments were presented in this chapter. First the details of the HDSC samples investigated were listed. The parameters of the two samples were given and SEM images and reflectance spectra made by FTIR (far field measurement) were presented. Brewster mode was clearly observed but the LSPR mode did not obviously appeared in the far field measurement. Both samples were designed to have a LSPR mode within the range of our mid-IR laser source so as to be investigated by near field measurement.

In our near field study, two techniques were used for mid-IR nanoscopy investigation of HDSC samples. The optical system of these two instruments were presented in detail. For the phase-sensitive mid-IR s-SNOM, we described the probe fabrication procedure and the GLIA detection method. Besides, we presented briefly the optical setup of the home-built s-SNOM and its operation procedure.

For the commercial PiFM, the mechanical detection mechanism was also presented. For PiFM operation, an unbalanced interferometer was added in the illumination path

to achieve a hgh-speed amplitude modulation when the laser wavelength is current-modulated. Focused laser spot imaging at both working modes (transmission mode and reflection mode) were presented because this is a necessary step in PiFM alignment. It can be noted that, with some modifications of the optical system, the commercial instrument should be able to perform PiFM and s-SNOM simultaneously. PiFM measurement with visible light was also tested in these preliminary test and a first comparison with SNOM signal was achieved in this range.

5. Experimental results and discussions

Contents

5.1 Nano-spectroscopic imaging of the HDSC submicronic ribbons **109**

5.1.1 s-SNOM images and spectra 109

5.1.2 PiFM images and spectra 119

5.2 Near-field optical images of 2D periodic nanoantenna array **127**

5.3 Conclusion **130**

In this chapter, we carry out the near-field characterizations of the HDSC structures with both s-SNOM and PiFM. The benefice of such crossed analysis is twofold. In principle, having two characterization tools may provide more information on the sample, but it can also provide an interesting comparison between the two techniques, notably regarding the question of the dispersive or the dissipative nature of the experimental lineshapes. Herein, 1D gratings and 2D arrays of HDSC nanostructures are spectroscopically investigated. The first structures (submicronic ribbons) are investigated in the vicinity of the plasma frequency and below and compared with dipole models that have been mostly introduced in chapter 2 and 3. Experimental and simulated spectra are discussed in this context. Then, we present the s-SNOM images of 2D periodic nanoantenna array where LSPR signature is observed. Then we focus on the investigation of HDSC gratings. The optical images and spectra made by both tools are presented respectively. Both analytical simulation and FDTD simulation are made and detailed explanations are given for the experimental results of the gratings.

5.1. Nano-spectroscopic imaging of the HDSC submicronic ribbons

Near-field study was conducted on HDSC gratings to investigate the LSPR mode of the sample ($\varepsilon < -1$), as well as determining the sample response in the vicinity of the surface mode ($\varepsilon = -1$) and in the vicinity of the plasma frequency ($\varepsilon = 0$). It should be noted that no diffraction order is here present due to the small pitch of the grating array compared to the wavelengths. Electromagnetic simulation and pitch dependent response, also show that the submicronic ribbons are too far from each other to be noticeably coupled. This can be understood given the high confinement of the LSPR on the structure edges. Hereafter, we start with the s-SNOM imaging performed using the tungsten probes and the 3 CW mode QCLs presented in chapter 4.

5.1.1. s-SNOM images and spectra

In our s-SNOM experiment, we use tungsten probes to investigate the sample response. In infrared spectroscopic near-field experiments, the dispersion of non-polar material such as silicon probes or metal probes can be ignored. Therefore the probe polarizability α is regarded as constant ($\tilde{\alpha} = 1$ is a good approximation for a metal sphere in the infrared, cf. Equation 2.3.9) and only the dispersion of the sample $\varepsilon(\lambda)$ is probed. It is then instructive to express the power scattered by the probe-sample system as a function of sample permittivity only (cf. Equation 2.3.17 and Equation 2.3.19).

Images at selected wavelengths and interpretation

We obtained a series of optical amplitude and phase images at different wavelengths within the range of the QCLs. Selected images are shown in Figure 5.1.1. Figures 5.1.1 (a) and (b) are the AFM topography image and profile of the grating, the detailed parameters of the gratings are presented in section 4.1. The incident beam polarization was set along the tip axis to obtain the maximum backscattered signal. The obtained images are characterized by a wavelength dependent contrast between the two materials which is found to be rather well accounted for by the mentioned dipole-image dipole model. First, we note that on

each of the two materials, the s-SNOM signal is spatially homogeneous except when the probe-sample interaction becomes more complex near the edges, where a marked drop in the signal is observed (permittivity spectrum is shown in Figure 4.1.5).

- At 9.3 μm ($\varepsilon \approx -1$), where we approach the ENZ region, the HDSC surface is dark compared to the substrate (Figure 5.1.1 (d), top).
- At 10 μm, on the contrary, for smaller permittivity value, the near field signal on the HDSC is maximal and a clear positive material contrast between HDSC and the GaSb substrate is observed.
- At 11 μm, finally bright edges are observed that can be associated with hyper confined localized surface plasmon resonance (LSPR). The phase signals on these two opposite bright edges are relatively out of phase (about 1.4 rad phase difference on Figure 5.1.1 (e), bottom). The asymmetry observed on the amplitude image between the two edges are due to the side illumination condition, which is well reproduced by electromagnetic simulation (cf. FDTD calculation on figure Figure 5.1.1 (c)).

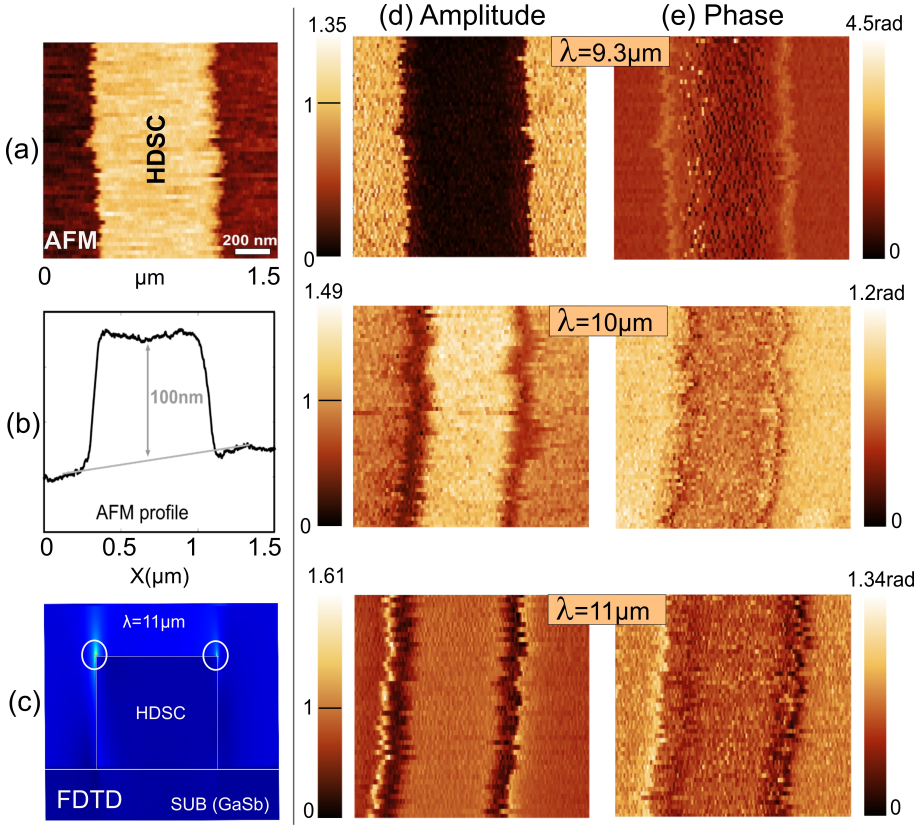

Figure 5.1.1.: Zoomed s-SNOM images of HDSC gratings: (a) Topography; (b) Profile of topography; (c) FDTD simulation of HDS grating at 11 μm wavelength; (d) Optical amplitude images at 9.3 μm, 10 μm, 11 μm wavelength (the signal is normalized by the optical amplitude on GaSb substrate); (e): Optical phase images at 9.3 μm, 10 μm, 11 μm wavelength.

To analytically explain the observed phenomenon above, we plot the scattering cross section of a vertically polarized dipole following the expression given by Equation 2.3.17 and Equation 2.3.19, shown in Figure 5.1.2. The observed maximum corresponds to the sample-induced resonance which is positioned near $\varepsilon \approx -1.66$ when the spherical probe is in contact with the semi-infinite surface. In addition, we see that the scattering cross section can have two minima near $\varepsilon_s = -1$ and $\varepsilon_s = 0$.

- The first minimum (SPP mode) has its origin in the effective polarizability that drops as $\beta = \frac{\varepsilon_s - 1}{\varepsilon_s + 1}$ becomes very large . This decay is obviously much less visible if ε_s has a larger imaginary part.

- The second has nothing to do with the self-field but comes from the fact that all the waves impinging on the surface when $\varepsilon_s \approx 0$ are out of phase with the incident field, resulting in a vanishing of the perpendicular field component.

The second assertion can be easily checked by calculating the value of $r_p(\theta)$. For any value of the polar angle θ, we see that $r_p \to -1$ (or $+1$ depending on polarization orientation convention) so that $d\sigma_\perp$ given by Equation 2.3.17 drops for all the angle. This behavior holds not only for the radiation waves but also for the p-polarized evanescent waves. This is also indicated by the electrostatic limit of r_p since $\varepsilon_s \approx 0$ entails $\beta \approx -1$. Thus it is hardly possible to illuminate the surface of ENZ material with any p-polarized field: the ENZ surface is black. Consequently the p-polarized emission of a near-field emitter like a fluorophore or a near-field tip should be efficiently quenched in the surface vicinity. Accordingly, the local density of states (LDOS) of a p-polarized emitter can also drop to zero as the external field composed of the illuminating field E_i and self-field induced by image dipole E_{self} cancels out. This is a limit case though as the existence of losses can lead to LDOS resonance in the vicinity of the ENZ material.

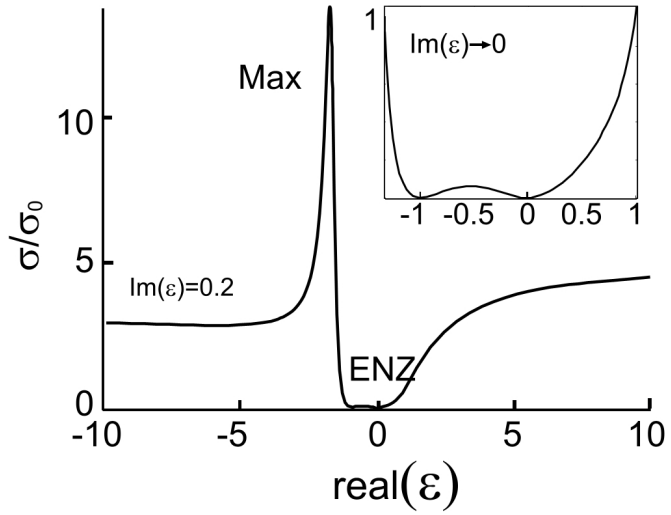

Figure 5.1.2.: Scattering cross section of a vertically polarized dipole above a surface normalized with the free space scattering cross section. For the solid line, the imaginary part is fixed to an arbitrarily small value of 0.2. Right: Zoom on the two minima.

We can note that the LSPR edge mode at air/HDSC interface is actually expected at $\varepsilon_s = -3$ according to theoretical prediction[51] for a 90° edge (c.f. Equation 1.1.24). In Figure 5.1.1, it is observed near $\varepsilon_s \approx -4.2$. The noticeable red shift can be attributed to the non ideal shape of the structure, residual coupling with the second edge formed by HDSC ribbon and the substrate, as well as a strong coupling between tip and sample. An explanation of this red shift is presented in the following using FDTD simulation.

LSPR Simulation Numerical simulations (cf. Figure 5.1.1) were carried out by solving the Maxwell equations by finite-difference time-domain (FDTD) method (Lumerical FDTD Solutions 8.12.631 from Lumerical Solutions Inc.) as reported before[34] using the dielectric function. The LSPR occurring at the top corners of the HDSC ribbon is observed at slightly negative value of ε (The LSPR at the two bottom corners with the substrate appear at higher wavelengths, beyond the range of our source).

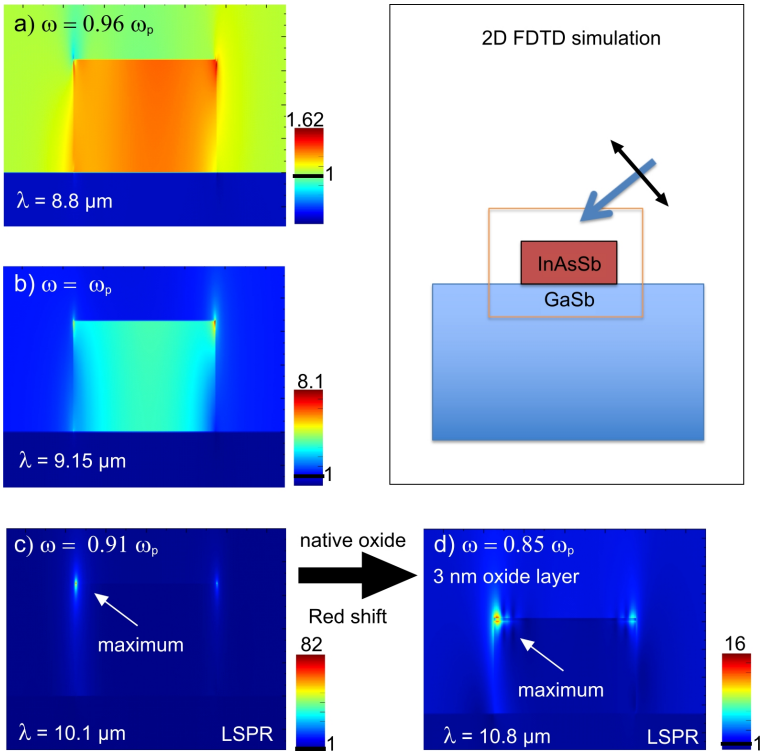

Figure 5.1.3.: Map of the electric field amplitude for selected wavelengths using 2D FDTD simulation: a) above the plasma frequency; b) at the plasma frequency; c) at the LSPR frequency ($\omega < \omega_p$); d) The presence of dielectric thin layer (3nm thick with a mesh size of 0.2 nm, and an arbitrary refractive index of 2.8) shifts the resonance to 10.8μm.

FDTD simulation of the structures with realistic dimensions are reported in Figure 5.1.3, where the light is coming from the left (reversed compared to Figure 5.1.1). From this simulation, we see that the maximum field maxima could in fact be obtained for $\varepsilon_s = -2$ ($\lambda \approx 10.1$ μm), and that the local resonance is rather sharp and intense although the signature of the resonance on the reflectivity spectrum is nearly invisible (not shown here). The spectral position of this LSPR is found to be nearly unaffected by relatively large changes in the HDSC thickness, width or by rounding the edge. However the position of the resonance is strongly affected by a change in their immediate environment, such as a contamination layer (or eventually a probe). For example, a native oxide layer (such as In_2O_3) of 2 or 3 nm will shift considerably the resonance toward 11 μm (red shift), while damping

it noticeably. The presence of thin native oxide layers on the same type of structure is reported in article[180].

s-SNOM amplitude spectrum

To generate the HDSC spectra, we normalize each point of the signal, by the response on the nearly undoped GaSb substrate ($n_{GaSb} = 3.77$). The spectrum is shown in Figure 5.1.4 (a). The relative s-SNOM signal on HDSC, A_{HDSC}/A_{SUB} is fitted using $A = \sqrt{\sigma_{\perp}(\theta)}\left|1 + r_p(\theta)\right|$, with $\sigma_{\perp}(\theta)$ the differential scattering cross section of a vertically polarizable nano-sphere. This signal is proportional to $|\alpha_{eff,z}|$, as described in the Equation 2.3.9 and the factor $\left|1 + r_p(\theta)\right|$ is accounting for the illumination field which is considered as mostly reflected by the surface.

The s-SNOM fit was obtained considering a distance of 2 nm between the s-SNOM probe apex and the sample, and the polarizability of a tungsten probe multiplied by a complex factor $(1.2 + 0.68i)$. From Figure 5.1.4 (a) we can see that the s-SNOM amplitude, a signal proportional to $|\alpha_{eff,z}|^2$, fits rather well the observed signal.

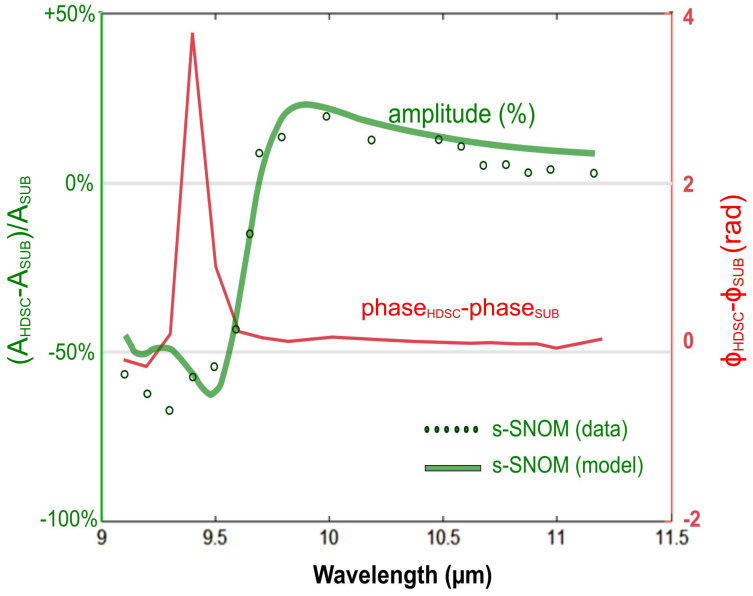

(a)

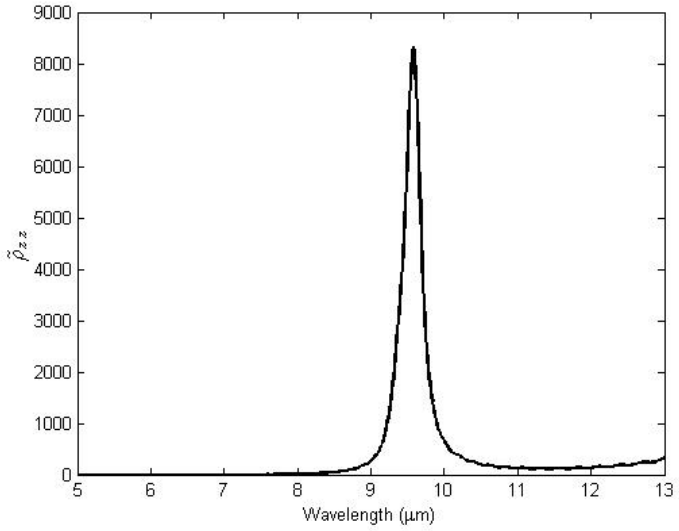

(b)

Figure 5.1.4.: Near-field spectra on HDSC relative to the substrate signal obtained with s-SNOM (tungsten probe): (a) Red curve: phase difference between the HDS and the substrate. Circles and green line: experimental s-SNOM signal and simulation respectively; (b) Normalized LDOS in vacuum in z direction as a function of the infrared wavelength calculated at 100 nm from the upper HDSC surface (simulation generated by Remi Vincent).

To study the influence of the thickness of HDSC on near-field signal, with the theoretical analysis model (Equation 2.3.14) described in chapter 2, analytical spectra on different thickness of HDSC (normalized by the substrate, all the other parameters remains the same) can be obtained, as shown in Figure 5.1.5. The shape of the spectrum have the same trend while the signal difference near plasma frequency is larger when the HDSC is thinner. The observed changes are due to the change in far-field reflection coefficient r_p. Here, the minimum positioned at larger wavelength near $\varepsilon = -1$ (larger wavelength) remains mostly unaffected. However, for smaller thickness it should be noted that the surface mode will progressively shift toward ω_p (i.e. from $\varepsilon = -1$ to $\varepsilon = 0$) as the so-called ENZ mode appears. This effect can be ignored as long as the confined field of the dipole probe does not feel the presence of the second interface (which depends on probe size and distance), otherwise the electrostatic reflection coefficient β needs to be modified as detailed elsewhere[164].

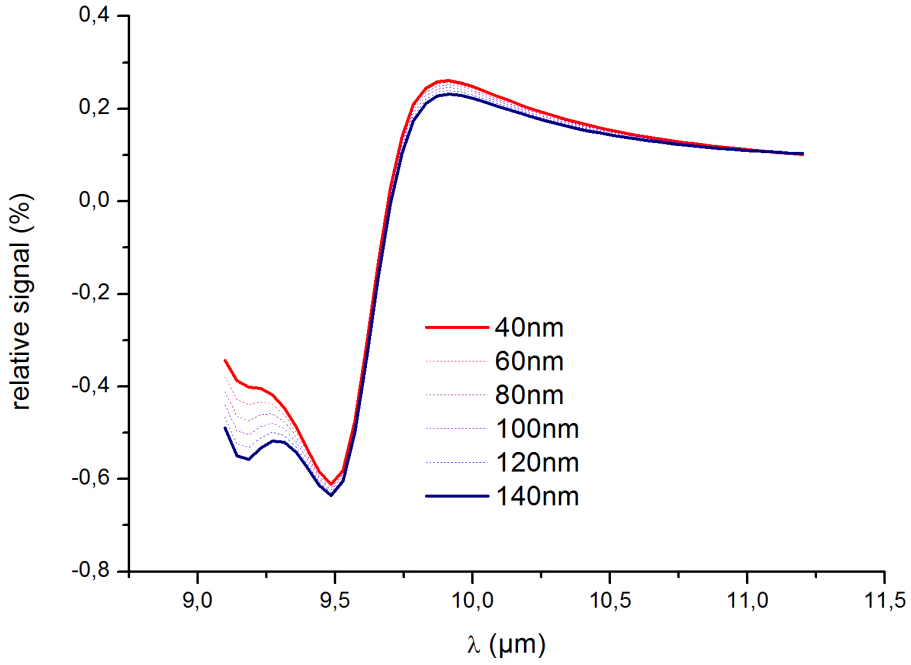

Figure 5.1.5.: Relative near field signal on HDSC for different thickness.

s-SNOM phase spectrum

Considering the phase spectrum, we notice a qualitative correspondence with the *partial LDOS*. Under certain assumptions, a proportionality link between the local density of optical states (LDOS) and optical phase has already been derived in a recent theoretical paper considering phase information resolved with s-SNOM for a dielectric probe[28]. The partial LDOS in the z-direction normalized by the total LDOS in vacuum is plotted as function of infrared wavelength from 5 μm to 13 μm in Figure 5.1.4(b)[1]. Using FDTD method under Lumerical software, we calculate the vacuum-normalized LDOS at the center position localized at 100 nm from the HDSC upper interface, which is defined by:

$$\widetilde{\rho}_{zz}(\mathbf{r},\omega) = \frac{\rho_{zz}(\mathbf{r},\omega)}{\rho_0}$$

where $\rho_{zz}(\mathbf{r},\omega)$ is the LDOS for a vertical dipole-like emitter (z direction) at the position $\mathbf{r}$ and at the frequency ω, and ρ_0 is the LDOS in the vacuum defined by $\rho_0 = \omega^2\pi^2c^3$. We simulate the periodic structure, using a 3D calculation of several HDSC grating periods on GaSb substrate, up to convergence.

Comparing LDOS curve (Figure 5.1.4(b)) and optical phase spectrum (Figure 5.1.4(a)), we see that the shape of the two curves are similar. Such spectrum could *experimentally* demonstrate the correlation between LDOS and optical phase. Discrepancies may mostly comes from the fact that the probe emission pattern is different from a dipole radiation pattern and the metal nature of the probe.

Investigation on a less doped InAsSb sample

The optical amplitude spectrum of a second HDSC grating sample is shown in Figure 5.1.6. This HDSC grating has a lower plasma frequency which corresponds to a wavelength of 9.4 μm. The sample dimensions are presented in Figure 5.1.6 (a), the width of the InAsSb grating is 3 μm and the periodicity is 6 μm. Here, a similar spectral study is conducted on this sample with much more wavelength points. The probe provided less signal in this case, which is the case when the home-made probe is relatively big compared to the probe

[1]The LDOS simulation is generated by Remi Vincent from our lab.

oscillation amplitude. Despite the noise, the form of the fitting spectrum is globally as expected, i.e. slightly red shifted compared to the previous spectrum. The dip near the plasma frequency (located before maxima value of the optical amplitude) is less obvious. Seeing Figure 5.1.5, the finite thickness explain the smoother dip in this second HDSC grating sample.

As we have introduced in the first chapter, Brewster/BE mode appears at thin film and ENZ mode appears at ultra thin film. From this simulation we can also say that s-SNOM spectrum can observe and distinguish the two ENZ material modes.

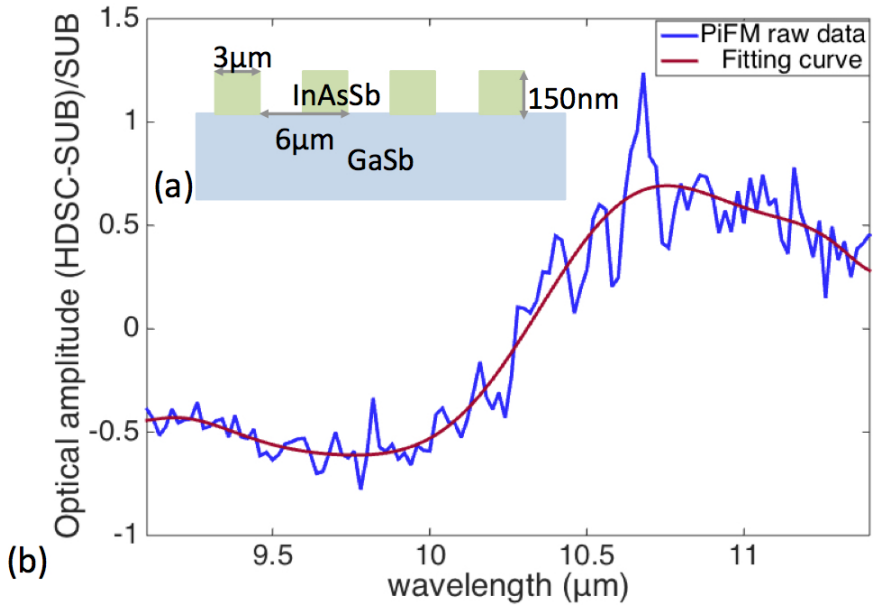

Figure 5.1.6.: HDSC Gratings with lower plasma frequency (corresponding wavelength 9.4 µm): (a) Scheme of sample; (b) Optical amplitude spectrum: blue curve is raw experimental data and red curve is a fitting curve showing the form of the raw data.

5.1.2. PiFM images and spectra

Similar images were made with PiFM as shown on Figure5.1.7 at selected wavelengths with a cantilever-based AFM from Molecular Vista inc. operating with gold coated silicon probes. In this experiment, the time-averaged photoinduced force induced by a pulsed laser source is measured at the first mechanical resonant frequency of the cantilever, while the

AFM feedback is operated in tapping mode on the amplitude of the second mechanical resonance. The side-band coupling mode described in subsection 4.2.2.1 was used for obtaining the PiFM images and spectra. In Figures 5.1.7 (a) and (b), just as for the s-SNOM images, we observe a sample-induced resonance, where the PiFM signal goes from small value in the ENZ region to a maximum value for more negative value of ε. We note that the strongly confined LSPR signature can also be observed near 11 μm as shown in the high resolution image on Figure 5.1.7 (c).

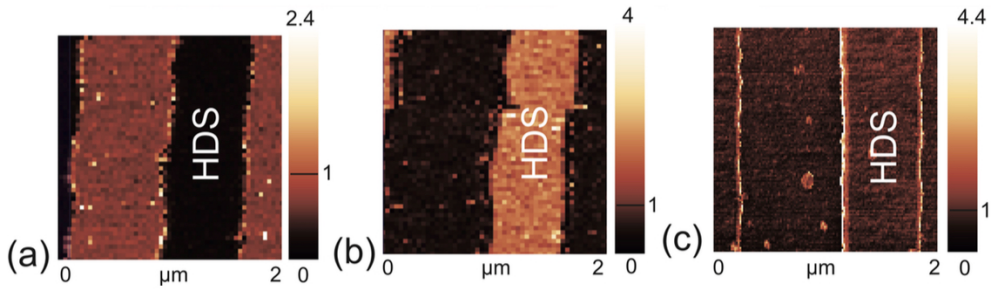

Figure 5.1.7.: PiFM images of HDSC gratings: (a)-(c): PiFM images at 9.02 μm, 10.53 μm, and 10.8 μm wavelength (the colorbar scale is normalized by the optical amplitude on GaSb substrate).

PiFM spectra[2] normalized by the PiFM response of GaSb substrate and theoretical simulations are shown in Figure 5.1.9. Typically, the model described in section 3.3.2 is intended to be used when the probe is bigger than the particle (sample) so that the particle is regarded as a dipole, or alternately another model was presented where the external (illumination) field is supposed to be exponentially decreasing. It doesn't fit our PiFM spectra because in our case, the nano-source generated by the probe is much smaller compared to the sample, and we also consider that our illumination field is relatively homogeneous considering the large free space wavelength we use. Therefore an alternative dipole-model is here proposed for PiFM which regard the probe as a dipole as for the s-SNOM case.

[2]The PiFM spectrum with large bandwidth were performed using another pulsed source at MVI (MolecularVista Inc.). In Figure 5.1.7, (a) and (b) are generated in MVI and (c) is imaged by modified QCL (with horizontal interferometer).

Probe-dipole model for PiFM

When the size of the probe is much smaller compared with the sample, time-averaged optical force exerted on a dipole scatterer inside a spatially inhomogeneous field has the following expression[172, 154]:

$$< F >= \sum_{l=x,y,z} \frac{1}{2} p_l \nabla E_l \tag{5.1.1}$$

where $E = (E_x, E_y, E_z)$ is the local field experienced by the probe, and where $p = \alpha E = \alpha_{eff} E_i$ as described in Equation 2.3.8. The latter expression $\frac{\alpha_{eff}}{\alpha} E_i$ allows us to substitute the local field by the external (illumination) field. In the following, as previously, we consider only the vertical direction, along which the local field is inhomogeneous:

$$< F_z >= \frac{1}{2\alpha} p_z \nabla(\alpha_{eff,z} E_{i,z}) \tag{5.1.2}$$

For qualitative descriptions, the external field appearing in this equation may be considered to be exponentially decreasing: in that case the force can be expanded in two terms, one being proportional to the local field E, the other being proportional to the gradient field. Such approach is relevant if a structure small compared to the nanoprobe is investigated. In our case, the sample beneath the tip is flat and much larger than the nano-probe (except on the grating edge, where the description fails), the external field is considered as spatially homogeneous in the surface near-field, typically consisting in the sum of the incident field and its reflection on the surface in the absence of the probe. Therefore, the fast z dependence of the local field is accounted by the effective polarizability only. In that case the net force is simply:

$$< F_z >= \frac{3K_c |E_{i,z}|^2}{2h^4} |\alpha_{eff}|^2 Re(\beta \alpha_{eff}) \tag{5.1.3}$$

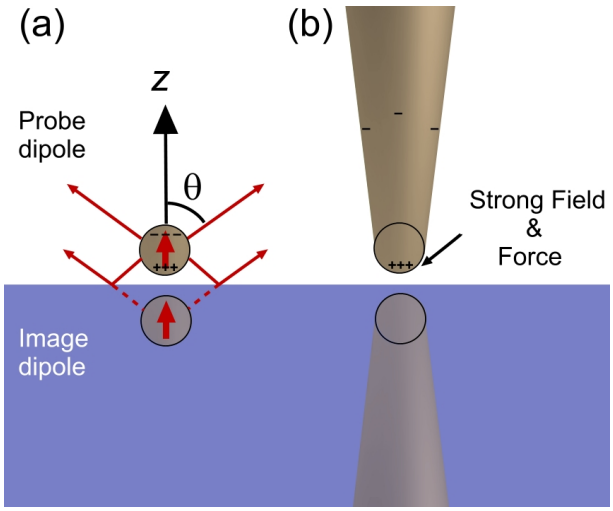

Figure 5.1.8.: Representation of dipole-image dipole model of PiFM: (a) considering probe as a sphere dipole; (b)considering geometry of a real probe.

However, such expression does not satisfactorily accounts for the experimental spectrum, which is found to be more faithfully described by a force proportional to $|\alpha_{eff}|^2$. A marked discrepancy is not necessarily surprising given the flaws of the point dipole model[13]. The substantial interest of such model is to offer a simple analytical expression for the PiFM signal. However, in the described model, the field inside the sphere is homogeneous and evaluated at the center position. It means that we are considering two symmetric charge distributions accumulated on each top and bottom side of the sphere (cf. Figure 5.1.8(a)). These two charge distributions are described as two opposite charges which produce two opposite forces at the origin of the field gradient in Equation 5.1.1. While this dipolar model can capture many features of the near-field signal scattered by tip apex, it is clear that a real probe exhibits a strongly asymmetric charge distribution (cf. Figure 5.1.8(b)), with a higher charge density near the very apex. So, on the contrary, we will now assume that a single force $qE(t)$ is exerted on the charge at the bottom of probe, where the field is stronger and the charge distribution more concentrated.

In that case, we consider that the net average force is simply provided by:

$$< F_z >= \frac{1}{2} Re(\frac{p_z^*}{a} E_{l,z}) \tag{5.1.4}$$

where p_z^*/a serves to accounts for a single charge fluctuation at the very apex of radius a. Substituting again the local field for the external field, we obtain straightforwardly the simple following expression:

$$< F_z >= C|\alpha_{eff}|^2 \tag{5.1.5}$$

where the proportionality factor is given by $C = \frac{1}{2a}|E_{i,z}|^2 Re(\frac{1}{\alpha})$.

Depending on the considered operation mode of the PiFM (sideband detection, cf. subsection 4.2.2.1), it was pointed out that the detected signal might be sensitive to the derivative of $< F_z >$ with respect to z. If this is correct, this contribution could then be provided by:

$$< F_z >'_z = \frac{6K_c}{h^4} < F_z > Re(\beta\alpha_{eff}^*\alpha) \tag{5.1.6}$$

The latter expression is very similar to the force expected for a small, finite, scatterer, as described by Equation 5.1.3.

In Figure 5.1.9 we can see that the force signal can be correctly fitted with the probe dipole model we proposed. As detailed in Equation 5.1.5, the expression of the time-averaged force $< F_z > \propto |\alpha_{eff,z}|^2$ considers the interaction between the local field described through $\alpha_{eff,z}$ and a unique apex charge proportional to the induced dipole moment p also proportional to $\alpha_{eff,z}$. The analytic PiFM data were fitted using a negligible distance between the probe apex and the polarizability of a Si sphere multiplied by a complex factor $1.89 + 0.45i$. For the PiFM, the force signal is correctly fitted with dipole approximation without resorting to induced photoexpansion.

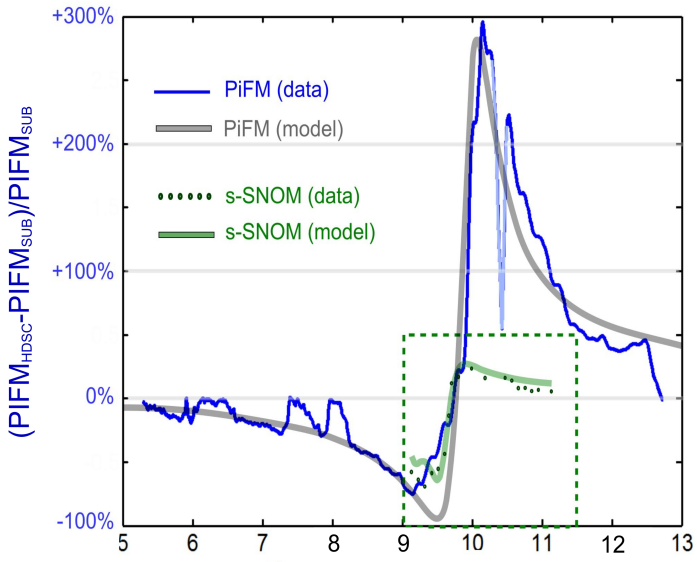

Figure 5.1.9.: Near-field spectra on HDSC relative to the substrate signal obtained with PiFM (gold-coated silicon probe): Blue and gray curves: experimental PiFM signal and analytic simulation respectively; Circles and green line: experimental s-SNOM signal and simulation respectively.

FDTD modeling for PiFM

As mentioned in section 3.3.1, FDTD simulation can also be used to calculate optical force. In Lumerical FDTD Solutions, an analysis box called "optical force MST[3]" can be used to calculate photo-induced force (PiF) on the probe. This method presents some limitation though because the box must entirely enclose the scattering probe, which also prevent realistic probe to be considered given the needed computational resources in this case. To make some qualitative comparison with dipole model, we placed a small sphere above the sample to mimic the probe. The FDTD simulation system is drawn in Figure 5.1.10. The distance between sample and probe d is changed and the probe material is changed in the simulation. The mesh size between probe and sample surface is 1 nm.

[3]MST: Maxwell Stress Tensor.

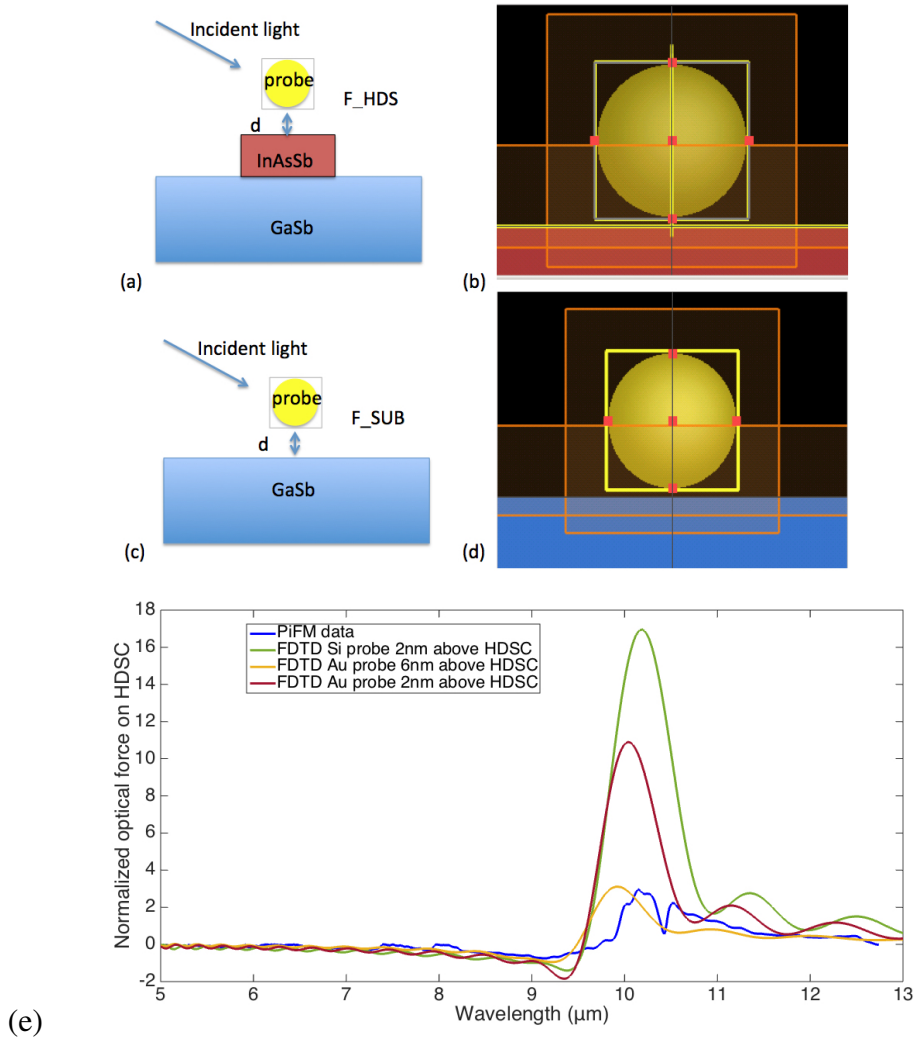

Figure 5.1.10.: FDTD simulation system of optical force: (a) and (b) are sketch figure and diagram of zoomed FDTD XZ plan, they describe the probe on HDSC grating system; (c) and (d) are the probe on substrate system, which is used as the normalization reference (we use a Si and Au sphere to mimic the probe response); (e) FDTD simulation of PiF compared with experimental data. Blue curve: experimental PiFM signal; green, red and orange curves: FDTD simulations.

Both F_z on HDSC and substrate are obtained and after normalization we can see the three curves from Figure 5.1.10 (e). When a Si probe is placed 2 nm above the sample, the maximum signal of FDTD simulation is bigger than that of experimental data. If we

replace Si with Au probe. the maximum value is smaller but still much bigger than that of experimental data and blue shifted compared to the PiFM spectra. The dip is more obvious but slightly blue shifted compared to the PiFM spectra. The dip near plasma frequency ω_p of FDTD calculation is more obvious than that of Si probe.

Obviously the probe is seen as a small particle in FDTD which is not the real case, but this prevents divergence problem and leads to more reasonable calculation time. Second, in FDTD simulation, the permittivity of the probe is set according to the material properties (Si or gold in the mid-IR). It should be noted that in the analytical model we used a complex *arbitrary* polarizability to account for the experimental spectrum. This phenomenological approach is an ersatz to account for the semi-infinite probe response. The imaginary part of this polarizability is damping the calculated optical force. Similar approach could be undertaken here, but the simulation times makes fitting approach difficult with FDTD.

If we place the gold probe 6nm above the sample, the maximum value is comparable but an obvious blue is observed because there is less interaction between sample and probe (a shift is also observed with the analytical model, not shown here).The analytical simulation is better fitted with the experimental data than the FDTD simulation. But it can still provide a clue of PiFM signal detected by the probe.

Summary for s-SNOM and PiFM spectra

For both PiFM and s-SNOM modeling, the general signal line shape accounted by $|\alpha_{eff}|^2$ contains both a dispersive and dissipative contributions. Their respective weights strongly depend on the sample response $\beta = \frac{\varepsilon-1}{\varepsilon+1}$ on HDSC, which is included inside α_{eff}. Here, this sample response is fixed by the dielectric function values given by Equation 1.1.13, independently and precisely determined by FTIR measurement (cf. section 4.1.2). Beside the β value which is the main non adjustable ingredient leading to the observed shape, the fitting parameters for both spectra were the probe-sample distance, and the complex polarizability of the model sphere $\alpha_\perp$.

We note that the agreement between these simple analytical models and the experimental spectra tends to diverge in the ENZ region. Such divergence is not so surprising given the simplified, phenomenological, description provided by a vertically polarizable sphere.

Notably, the contribution of non vertical fields and forces become relatively stronger near ω_p since the signal for the p-polarized light tends to vanish.

Also, in our analytical modal, we assumed that the self-field generated by the probe is only coming from the HDSC layer (we neglects its finite size[4]). We know that for very thin layer (e.g. few tenth of nm at these wavelengths), the so called ENZ mode appears and that this mode corresponds to a shift of the SPP mode from $\varepsilon = -1$ to $\varepsilon \approx 0$. Experimentally our response since indeed a bit blue shifted as the PiFM and s-SNOM minima occurs at permittivity slightly higher than $\varepsilon = -1$.

Regarding PiFM, it was notably pointed out that the side-band detection should induce a contribution proportional to the derivative of the force along z. Adding such contribution could allow a better description in the ENZ region where the field confinement can strongly vary, however additional damping mechanism must then be considered to avoid nonphysical results.

As for s-SNOM, the lock-in amplifier detection can be relatively straightforwardly taken into account, but did not lead to a better description, leading us to the conclusion that additional simulation effort, when required, should rely on finer description of the lightning rod effect as in[13] where flaws of analytical dipole model are detailed. While ENZ materials described by a known dielectric function appear as excellent samples to determine the response of the near-field probes, a better modeling of the experimental near-field interaction will certainly be achieved by going one step further and combining information such as PiFM and s-SNOM signals within the same setup.

5.2. Near-field optical images of 2D periodic nanoantenna array

The LSPR mode of 2D periodic nanoantenna array is investigated by s-SNOM. We did optical imaging of the rectangular sample with illumination polarization along short axis of the rectangular shown in Figure 5.2.1. From the topography image we can see that the corner of the rectangular are rounded. The nanoantenna is more like ellipse. The plasma

[4]This hypothesis is only for calculating the self field (via $\beta = \frac{\varepsilon-1}{\varepsilon+1}$), on the other hand the radiation can take into consideration the finite size of the thin layer through the far-field reflection coefficient.

frequency of the array corresponds to a wavelength of 5.25 μm as mentioned in the previous chapter, section 4.1.3.

Around 10.8 μm, we observed clearly the LSPR mode on the edge of the nanoantenna. The signal is confined and enhanced at the edge, as shown in Figures 5.2.1 (b) and (c). In Figure 5.2.1 (c), the double bright edge is because the probe is nor tracking perfectly when it went across the nanostructure. As for the asymmetry observed on the infinite ribbon at the LSPR wavelength, here an asymmetry is also observed on the two edges of the nanoantenna because of the angle of the incident illumination. The FDTD simulation, Figure 5.2.1 (e), produces the same effect.

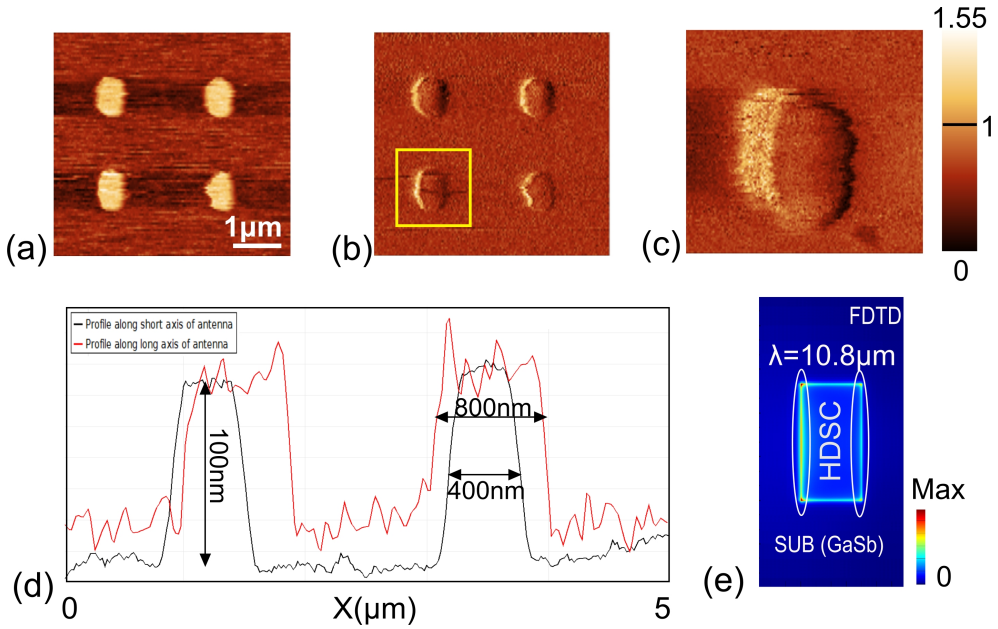

Figure 5.2.1.: s-SNOM image of 2D array: (a) Topography of the sample; (b) Optical amplitude of the sample; (c) Optical amplitude zoom of one nanoantenna (inside yellow box in (b)); (d) Profile of topography, black curve is along short axis and red curve is along long axis; (e) FDTD simulation of field distribution (XY plan).

Five images are taken at 5 wavelengths, from 10.6 μm to 11 μm, shown in Figure 5.2.2. The optical amplitude at 10.9 μm showed a better contrast. The LSPR mode is actually localized at the bottom corners of the rectangles, as demonstrated by FDTD simulation (Figure 5.2.4 (b)).

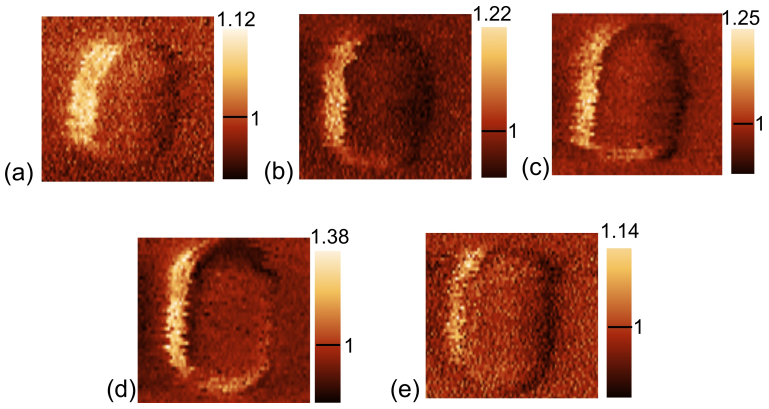

Figure 5.2.2.: s-SNOM optical image of 2D array at different wavelengths: (a) 10.6 μm ; (b) 10.7 μm; (c) 10.8 μm; (d) 10.9 μm; (e)11 μm.

The FDTD simulation of 2D array was carried out considering a polarization of the incident light along short axis X which, as it is mostly the case in our experiment. The reflectance is also shown in Figure 5.2.3. We can see that there are several peaks in the reflectance spectrum, two close and small peaks at 5.5 μm, 5.7 μm and a large peak at 11.1 μm. The first peak at 5.5 μm corresponds to the Brewster mode of the sample[173]. To see the two LSPR modes, the E field distribution images[5] is presented in Figure 5.2.4.

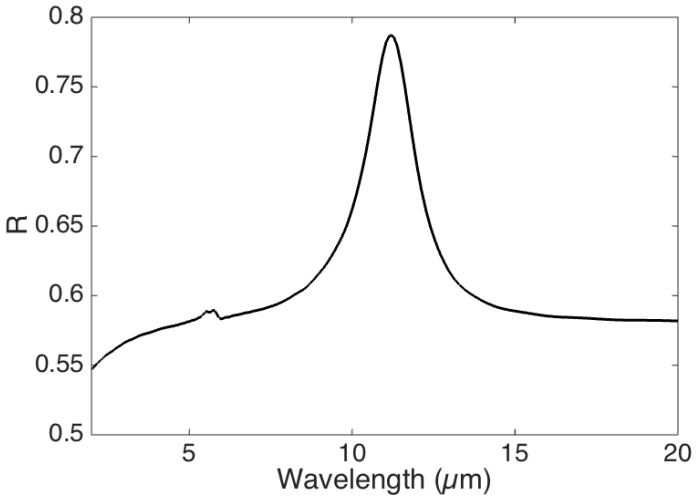

Figure 5.2.3.: FDTD simulation reflectance of 2D array

[5]We take the E field on XZ plan (X is along the short axis of the rectangular and Z is the height).

We can see that at 5.7 μm, the enhanced E is at the top corners of the structure where LSPR mode is observed between HDSC structure and air. We can note this high energy frequency ω_{top} which is as expected close to $\varepsilon = -1$. Owing to a higher refractive index of the substrate GaSb (compared with air), the enhanced E field at bottom corners are observed in a longer wavelength 11.1 μm. And the reflectance is much stronger and the enhanced confined field is stronger. We note this low energy frequency ω_{bottom}.

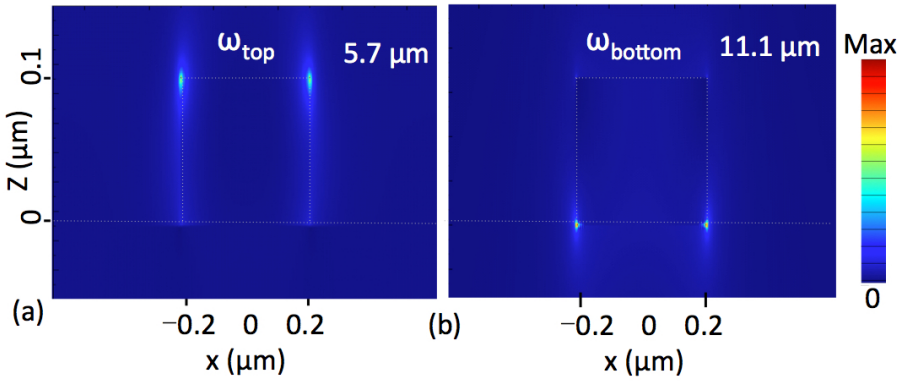

Figure 5.2.4.: FDTD E field simulation of 2D array at different wavelength (XZ plan).

5.3. Conclusion

To conclude, both HDSC samples were studied by near field nanoscopy. Results of the two samples were presented and discussion were provided based on theoretical simulations. First, on HDSC gratings, both s-SNOM and PiFM were used for spectroscopic study in vicinity of plasma frequency of the sample. With s-SNOM, both optical amplitude and phase images were taken at different wavelengths and normalized amplitude and phase spectra of the HDSC were obtained. The amplitude signal can accounted for by an analytic simulation based on dipole approximation model. Moreover, by comparing experimental phase spectra with LDOS simulation curve, we find a correspondence between phase spectra and LDOS. With PiFM, local field images were taken and similar response of HDSC were obtained. The force spectra show also a relatively good correspondence with analytic simulations based on dipole approximation. Then optical images were taken for HDSC 2D

array with s-SNOM. The LSPR mode at the substrate/HDSC interface was clearly showed in the near field images. Reflectance simulated by FDTD and E field distribution corresponding to LSPR at different interface were presented.

Conclusion and perspectives

In conclusion, spectroscopic phase-sensitive s-SNOM and PiFM imaging in side-coupling mode were performed on HDSC samples having a known dielectric function. With two near field techniques, both information on the local field distribution and complex permittivity were obtained.

In contrast with a previous PTIR study[49] on polaritonic material near Berreman modes, the PiFM exhibited essentially a non-dissipative lineshape like for s-SNOM. In both cases, a phenomenological point-dipole model based on the effective polarizability of the probe coupled to the substrate accounts relatively well for the observed lineshapes. From an experimental point of view, we have also developed an interferometric system in order to use CW mode IR laser for PiFM measurement instead of pulsed laser.

In addition, signatures of LSPR on the structure edges were also observed with both techniques, although slightly shifted with respect to the simulations performed on ideal square shaped structures without probe. The latter results also indicate the possibility to reveal infrared plasmonic modes with PiFM. In our study, in contrast with PTIR measurement, photo-expansion effect needs not to be taken into account for describing the signal on ENZ samples. With the near-field probes used in these experiments (tungsten s-SNOM probes and gold coated Si for PiFM probes), PiFM exhibited a better sensitivity to the dielectric function in the ENZ region. Therefore, as for s-SNOM, PiFM technique should effectively probe the impact of influence quantities on LO frequency such as stress or temperature, or fluctuation in the doping quantity near the material plasma frequency.

For HDSC 2D array, s-SNOM images were obtained and the local field enhancement at the edge of the nanoantenna were clearly showed on these images, which is the LSPR mode at the substrate/HDSC interface.

In a near-future, carrying out simultaneous PiFM and s-SNOM measurements with the same probe should make it possible to compare the spectroscopic signals more quantitatively and more particularly to evaluate whether the proposed or more advanced phenomenological models can account for PiFM and s-SNOM signals by using an identical probe polarizability.

Finally, as for s-SNOM, the carried work shows the relevance of PiFM approach for the characterization of polaritonic materials, but also lossless photonic devices since the photoinduced force is found to be independent from the sample absorption. This analysis should trigger additional nanospectroscopic investigations using combination of optomechanical and scattering-type methods.

Chapter 1 generally presented IR plasmonics and HDSC. First, we presented the dielectric function and Drude model that describes the permittivity of metals and doped semiconductors. Several potentials IR plasmonic materials were mentioned in order to introduce the highly doped III-V semiconductors investigated in this thesis. Then the notion of ENZ material was briefly presented. The existence of BE and ENZ modes was outlined.

Chapter 2 introduced the fundamental aspects of s-SNOM. Historical overview of the technique was presented. The nature of s-SNOM signal was presented by a dipole approximation model expressed in term of a dyadic function. Then a more complete electromagnetic model based on the Green dyadic function was presented. Furthermore, a recent interpretation, lightning rod model, was mentioned as it can consider more realistic geometry of the probe.

Chapter 3 presented the fundamental aspects of PiFM. The development background of PiFM was introduced through a brief state of art. Then, the two main PiFM models found in literature were presented: the optical force expression based on Maxwell's stress tensor (MST) and the dipole models. For the dipole model of PiFM, both systems of nanoparticle-dipole and probe-dipole were used. A recent probe-dipole model based explicitly on the Green dyadic function was finally introduced.

Chapter 4 provided the experimental details of the our investigation. Sample information were listed including the size, shape and permittivity parameters. Both SEM images and FTIR reflectance spectrum were given and Brewster mode and LSPR mode were observed. Then the details of the two experimental setup were introduced. For the phase-sensitive

mid-IR s-SNOM, we described the home-built setup as well as probe fabrication procedure and GLIA detection method. For the commercial PiFM, the detection mechanism is presented and working modes were introduced. The setup developed to carry out PiFM measurement with CW laser source was described.

Chapter 5 presented the experimental results and discussions. For HDSC gratings, both s-SNOM and PiFM images were presented and relatively similar spectroscopic responses were obtained in vicinity of plasma frequency and below. Normalized SNOM and PiFM spectra of the HDSC were shown, where dipole-based analytical simulations can be used to fit the spectra. The model developed to fit the PiFM data was presented. Moreover, a correlation between phase spectrum and LDOS were demonstrated experimentally. Then optical images of HDSC 2D array with s-SNOM clearly showed confined LSPR mode at the bottom edges.

Perspectives

Regarding perspectives, both samples and characterization tools can be investigated and developed. Many future works can be conducted for application of plasmonics and sensing as well as development of characterization instrumentation. While we did not worked on the sample development and application, the biosensing is indeed a major perspective for Infrared plasmonic and additional information are provided below. A possible application for nanoscopic tools is also given.

Biosensing

The HDSC can be used for SPR or LSPR-based sensing such as surface-enhanced infrared absorption (SEIRA)[181, 34, 182]. Because of the enhancement of the local field, when molecules are placed near the resonators, the interaction between light and molecules increases. Intense LSPR is needed for the SEIRA technique that can be used for biosensing in mid-IR. Such work is presented in the dissertation of Franziska Barho[173].

Both HDSC ribbons and 2D array are shown to provide an enhancement of electric field and increased sensitivity on refractive index[181, 34]. In a recently published article[181],

the vibrational line intensity of infrared-active absorption features of vanillin is increased 5.7 times with HDSC 2D array.

To improve further the absorption, more advanced designs needs to be developed. Nevertheless, the investigated HDSC semiconductor holds great potential to be used for biosensing device.

Temperature mapping

Regarding the instrument development, first attempts to determine temperature were tried at the end of the thesis (not reported here). The idea is to monitor near-field spectrum change as the temperature increases and to relate this information to a local temperature. While a broadening of the spectrum may have been obtained, the investigated HDSC is entirely degenerated at room temperature, therefore a clear shift was not observed. Investigation using surface phonon-polariton should provide higher sensitivity.

In these experiments, an extra laser was used for sample heating. If temperature maps can be obtained, this approach would open perspectives for determining thermal conductivity, following the approach demonstrated by Balandin et al.[183, 184] known as Optothermal Raman Technique (ORT).

Résumé étendu

Nous donnons ici un résumé étendu en français de ce travail. Ce résumé reprend succinctement les différents travaux réalisés. Pour plus détails, il convient de se rapporter au manuscrit de thèse proprement dit.

1. Aspects fondamentaux

Dans cette partie du résumé décrivant les aspects plus fondamentaux, nous nous interessons à la plasmonique IR et aux semiconducteurs fortement dopés. Nous présentons ensuite le modèle analytique permettant d'appréhender le signal en nanoscopie de champ proche optique.

Plasmonique infrarouge et semi-conducteurs fortement dopés

La réponse d'un matériau à un champ électrique externe est principalement déterminée par le vecteur de polarisation, qui est relié au champ électrique par l'intermédiaire de la permittivité ou de la fonction diélectrique ε. Pour les champs harmoniques allant de l'UV au THz, la fonction diélectrique a typiquement une forte dépendance fréquentielle et est commodément traitée comme une fonction complexe de la fréquence angulaire lumineuse ω:

$$\varepsilon(\omega) = \varepsilon'(\omega) + i\varepsilon''(\omega) \tag{1.1}$$

La fonction diélectrique est le paramètre clé décrivant les propriétés électriques et optiques d'un matériau. Pour des charges libres, en dessous de la fréquence du plasma ω_p, la partie réelle de la permittivité ε' devient négative pour rendre compte des oscillations collectives

de ces porteurs dans le matériau[37], condition requise pour l'excitation d'une surface plasmonique ou d'un mode localisé. La partie imaginaire ε'' est liée aux pertes associées à la diffusion des électrons de conduction par les défauts, les états de surface et les vibrations du réseau[38].

Le modèle de Drude

Le modèle de conduction électrique Drude permet d'exprimer la fonction diélectrique associée aux porteurs libres ou quasi-libres. Le modèle de Drude permet ainsi de décrire l'influence des électrons quasi-libres sur les propriétés optiques d'un métal ou de semiconducteurs fortement dopés (HDSC). Ce modèle considère les électrons comme un gaz de porteurs de charge parcourant un milieu d'ions positifs uniformément réparti. L'expression de la fonction diélectrique basée sur le modèle de Drude est :

$$\varepsilon(\omega) = \varepsilon_\infty + i\frac{\sigma(\omega)}{\omega\varepsilon_0} = \varepsilon_\infty\left(1 - \frac{\omega_p^2}{\omega^2 + i\gamma\omega}\right) = \varepsilon'(\omega) + i\varepsilon''(\omega). \tag{1.2}$$

A partir de l'équation d'onde, nous savons que l'indice de réfraction complexe $n = n_r + i\kappa$ est directement lié à ε par la relation $\varepsilon = n^2$. La réflectivité $R(\theta)$ est déterminée par des indices de réfraction du matériau complexe à l'aide des coefficients de Fresnel. Pour une incidence normale sur un matériau massif, la réflexion est donnée par :

$$R = \left|\frac{n-1}{n+1}\right| = \frac{(n_r-1)^2 + \kappa^2}{(n_r+1)^2 + \kappa^2} \tag{1.3}$$

En pratique, un spectromètre infrarouge à transformée de Fourier (FTIR)[41] permet de mesurer R, potentiellement sous différent angles, et peut ainsi être utilisé pour caractériser les HDSC. On peut voir sur la Figure1.1 que la réflectivité augmente à mesure que la permittivité réelle passe du positif au négatif. Les réponses comparées d'un film de HDSC à perte élevées et à pertes faible pour une épaisseur de100nm, montre une chûte de réflectance marquée à la fréquence du plasma. (Pour les pertes élevées, la partie imaginaire de la permittivité est arbitrairement multipliée p²ar cinq.) Ensuite, si on diminue l'épaisseur du film à 10 nm, la pente de la réflectivité sera beaucoup moins évidente (cf. Figure 1.1 (a)).

D'autre part, le signal de champ proche montre une forte variation quand epsilon est proche de zéro (c.f Figure 1.1 (b)).

(a)

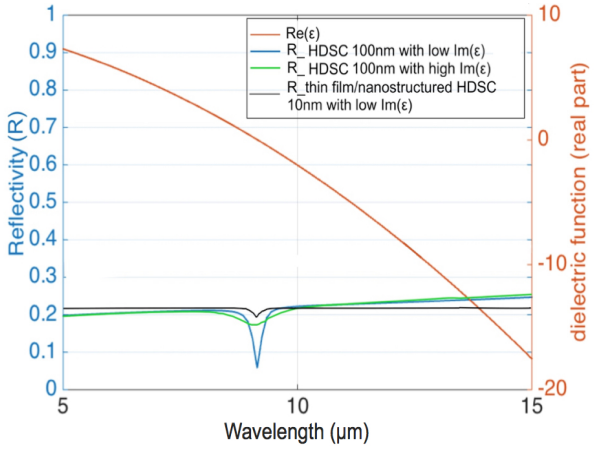

(b)

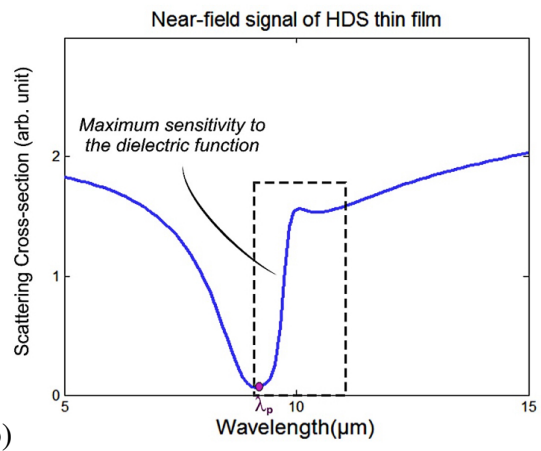

(c)

Simulation of R with Drude model	Thickness of InAsSb	Incident angle	Refractive index of substrate GaSb	The relaxation rate γ of InAsSb	ε_∞ (InAsSb)	Plasma frequency of InAsSb	Imaginary part of dielectric function InAsSb
Bulk HDSC with low loss	100nm	45°	3.77	$3.8*10^{12}$	10.4	$6.64*10^{14}$	Im (ε)_Drude
Bulk HDSC with high loss	100nm						5*Im (ε)_Drude
Thin film HDSC	10nm						Im (ε)_Drude

Figure 1.1.: Simulation du signal en champ lointain du film mince HDSC: (a) Réflectivité du champ lointain de HDSC; (b) Signal de champ proche d'un film mince HDSC de 10 nm; (c)Paramètres utilisés pour la simulation de R.

Mode Plasmon-Polariton de surface dans un métal ou un HDSC

En se propageant dans la matière, le photon interagit avec les charges et cette nouvelle quasi-particule, couplée, est appelée polariton chaque fois que la signature d'un couplage fort existe. Pour un métal ou un semi-conducteur dopé, le polariton correspondant est nommé plasmon-polariton. Suivant le modèle de Drude, l'existence d'un fort couplage entre plasma et lumière est évidente lorsque l'on se rapproche de la fréquence du plasma.

Les matériaux polaritoniques, comme les métaux, les semi-conducteurs dopés ou simplement les matériau polaires (dans ce cas le polariton est phononique), peuvent supporter un mode de surface électromagnétique, dans la mesure où la prie réelle peut être négative. Habituellement, la surface est l'interface séparant le matériau polaritonique d'un autre milieu tel que l'air ou un matériau diélectrique avec une permittivité positive.

Le mode de surface est caractérisé par un confinement lumineux à l'interface: la lumière présente une décroissance exponentielle des deux côtés de l'interface. Ce comportement est rendu possible lorsque ε est principalement réel et négatif sur une plage donnée, ce qui ce produit en deça de la fréquence plasma ou dans la Reststrahlen band pour les phonons polaritons dans les milieux polaires. A proximité de la fréquence plasma, cela conduit à un fort couplage entre l'onde lumineuse et le plasma à l'interface. Ce mode de surface est appelé Surface Plasmon Polariton (SPP).

Pour des nanoparticules métalliques dans un milieu diélectrique, des résonances lumineuses localisées (LSPR: localized SPR) sont excitées par la lumière. Ils présentent une amplitude de champ proche améliorée à la longueur d'onde de résonance. Ce champ est fortement localisé en surface de la nanoparticule et s'atténue rapidement dans le diélectrique à mesure qu'on s'éloigne de l'interface nanoparticule-diélectrique .

Dans le cas d'une couche mince polaritonique (e.g. HDSC), on rencontre deux modes résonants au voisinage $\varepsilon = 0$. Les caractéristiques des ces deux modes résonants sont les suivantes:

- **Mode de Brewster (Berreman)**[40, 47, 48, 49]**.** Alors que la condition de Brewster est en principe toujours rencontrée à une incidence normale près de $\varepsilon = 0$, le caractère résonnant du mode de rayonnement Brewter devient progressivement très fort à mesure que l'épaisseur diminue. Ce mode, qui rayonne hors du slab, peut alors être excité efficacement pour une incidende avec un angle. Ce mode est appelé mode Berreman, pour décrire les mêmes phénomènes mais dans le cas d'un matériau polaritonique lié aux phonons LO (longitudinal optique) plutôt qu'au plasma électronique. En raison de son caractère résonant, un pic d'absorption du mode de Brewster / Berreman peut être observé dans les spectres IR de champ lointain (en polarisation TM, avec un angle) bien que l'absorption au voisinage de ω_p (ou ω_{LO}) soit faible.

- **Mode ENZ confiné**[47, 48, 49]**.** Par rapport au mode Brewster, le mode ENZ ne peut pas être excitée par une onde rayonnée, car elle se trouve sous le cône de lumière. Ce mode nécessite une épaisseur extrêmement faible et peut présenter alors une courbe de dispersion quasi-plate (e.g. $\lambda_p/50$ ou moins).

Matériaux potentiels pour la plasmonique IR

Les métaux nobles (par exemple or ou argent) ont certains inconvénients pour les applications plasmoniques IR, en raison de leur pertes. Néanmoins, il existe d'autres matériaux à plus faibles pertes, pour la plasmonique IR, tels que les semiconducteurs dopés, les oxydes conducteurs transparents (TCO), le graphène, etc. On s'intéresse à la gamme IR moyenne et les semi-conducteurs III-V comme InAsSb présentent dans ce domaine une grande mobilité et de faibles pertes[58].

Les semiconducteurs III-V, tels que InAs, GaAs, InP et GaN, offrent un potentiel pour la plasmonique IR et leur utilisation ont été étudiées et peuvent être trouvées dans de nombreux articles[69, 70, 71]. L'InAs peut être dopé davantage que le n-GaAs et des LSPR à base d'InAs fortement dopés ont été démontrées autour d'une longueur d'onde de 9 μm[37]. Les pertes dans l'InAs sont faibles, les porteurs présentent une faible masse effective et il peut être fortement dopé (type n) jusqu'à quelques $10^{20} cm^{-3}$[76].

Concernant le choix du substrat support (GaSb), il faut noter l'écart important en énergie des bandes de conduction entre InAs et GaSb (1 eV), ce qui évite le transfert de charge de la couche InAs vers GaSb lorsque InAs est fortement dopé[80]. La constante de réseau de InAs est proche de celle de GaSb et l'incorporation de 9% de Sb avec InAs permet d'adapter le paramètre de maille à GaSb[78, 32]. De plus, l'InAsSb fortement dopé, proche de ω_p, possède naturellement des propriétés epsilon-near-zero (faible partie imaginaire) dans la gamme mid-IR qui peuvent être utilisées pour concevoir un comportement plasmonique spécifique[82].

Interaction sonde-échantillon

Dans cette thèse, un modèle analytique est introduit de manière détaillée afin d'appréhender "physiquement" le rôle des différents paramètres intervenant dans l'expérience de s-SNOM

et de PiFM. Nous reprenons dans une large mesure cette introduction théorique avant de présenter plus succinctement les points développés dans le corps du manuscrit.

s-SNOM

De nombreuses méthodes électromagnétiques ont été utilisées pour comprendre qualitativement les phénomènes. Parmi ces méthodes, les modèles analytiques basés sur l'approximation dipolaire s'avèrent très instructifs pour comprendre l'interaction sonde-échantillon survenant dans une expérience s-SNOM.

Nous considérons un dipôle électromagnétique oscillant à une fréquence de ω dans un milieu homogène ε_m. Le champ complexe rayonné au point d'observation est[150] :

$$E(r) = K(r)\left\{\frac{k^2}{r}(u_r \times p)\times u_r - \frac{ik}{r^2}\left[3\,u_r(u_r\cdot p) - p\right] + \frac{1}{r^3}\left[3\,u_r(u_r\cdot p) - p\right]\right\} = S(r_2, r_1)p \qquad (1.4)$$

où $K(r) = K_c e^{ikr}$ et k ($k = \sqrt{\varepsilon_m}k_0$) est le vecteur d'onde dans le milieu. De l'équation 1.4, on peut voir que la fonction dyadique de Green $S(r_2, r_1)$ qui lie E et p contient trois termes contributifs :

$$S(r_2, r_1) = S^{ff} + S^{if} + S^{nf} \qquad (1.5)$$

Dans une expérience s-SNOM typique, le dipôle sonde est proche de la surface de l'échantillon et illuminé par un champ externe E_i, le moment dipolaire induit est décrit par $p = \alpha E_i$. Pour une petite sphère isotrope, la polarisabilité α est un nombre complexe. Lorsque la distance entre la sonde et l'échantillon est très faible, une partie de la lumière est réfléchie depuis la surface vers la sonde, comme indiqué sur Figure 1.2. Ce champ auto-induit ("self-field") supplémentaire modifie le moment dipolaire et le rayonnement du dipôle sonde. Pour calculer ce champ auto-induit, la théorie électrostatique des charges images peut être utilisée, en supposant que la sonde sphérique est très petite par rapport à la longueur d'onde et que la distance sonde-échantillon est de l'ordre du diamètre de la sonde.

Avec cette théorie de la charge d'image, le moment dipolaire de l'image p_{im}[151, 152] induit par l'influence est exprimée comme :

$$p_{im} = \beta \begin{pmatrix} -1 & 0 & 0 \\ 0 & -1 & 0 \\ 0 & 0 & 1 \end{pmatrix} p \quad avec \quad \beta = \frac{\varepsilon_s - \varepsilon_m}{\varepsilon_s + \varepsilon_m} \tag{1.6}$$

où β est le coefficient de réflexion de Fresnel dans la limite électrostatique. ε_s et ε_m sont les fonctions diélectriques de l'échantillon et du milieu externe. Les signes négatifs ou positifs dans la matrice indique l'orientation parallèle ou anti-parallèle du dipôle image par rapport au dipôle sonde.

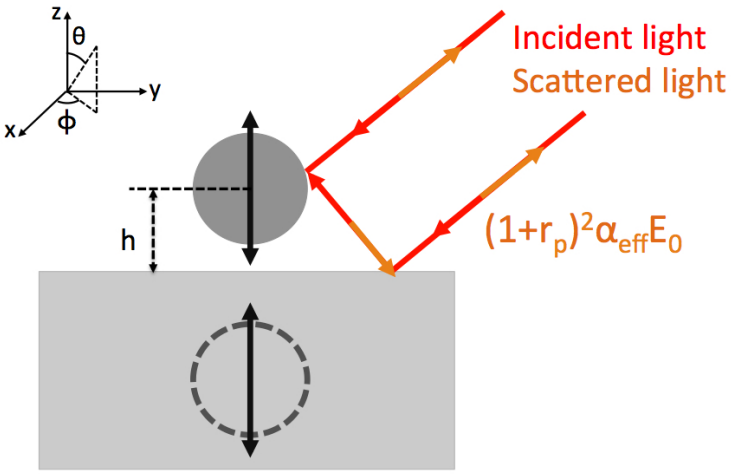

Figure 1.2.: La sphère polarisable correspondant au dipôle sonde est éclairé par un champ TM externe E_0 et un champ réfléchi $r_p E_0$. Le champ rétrodiffusé inclut également une contribution directe et une contribution réfléchie.

Le champ auto-induit quasi-statique induit par ce dipôle image à la position de la sonde peut être exprimé en utilisant le tenseur dyadique electrostatique valable en champ proche :

$$E_{self} = S^{nf}(r_p, r_{im}) p_{im} \tag{1.7}$$

où r_{im} et r_p sont la position de p_{im} et p respectivement. En considérant le self-field, le champ externe à la position de la sonde est maintenant :

$$E_{local} = E_i + E_{self} = E_i + S^{nf}_{self}(r_p, r_p)p \tag{1.8}$$

et

$$p = \alpha E_{local} = \alpha_{eff} E_0 \tag{1.9}$$

Le tenseur de "polarisabilité effective" α_{eff} a deux composantes distinctes :

$$\alpha_{eff} = \begin{pmatrix} \alpha_{eff\parallel} & 0 & 0 \\ 0 & \alpha_{eff\parallel} & 0 \\ 0 & 0 & \alpha_{eff\perp} \end{pmatrix} \text{ avec } \alpha_{eff\parallel} = \frac{\alpha}{1 - \frac{\alpha\beta K_c}{8h^3}} \text{ et } \alpha_{eff\perp} = \frac{\alpha}{1 - \frac{\alpha\beta K_c}{4h^3}} \tag{1.10}$$

Dans l'expérience s-SNOM, la détection se produit généralement en un champ lointain. Sur la Figure 1.2, il y a deux contributions de rayonnement en champ lointain de ce dipôle dans une direction (θ, φ) de l'espace homogène au-dessus de la surface, une contribution directe E_d et une partie réfléchie E_r :

$$E_{scat}(\theta, \varphi) = E_d(\theta, \varphi) + E_r(\theta, \varphi) \tag{1.11}$$

En s-SNOM, la polarisation de la sonde est typiquement le long de la direction z, donnée par le vecteur unitaireu_z, pour bénéficier d'un exaltation par effet de pointe au niveau de l'apex de la sonde. En effet, la polarisabilité verticale est plus forte selon la direction de l'axe de la sonde pointe et habituellement, seule la composante verticale du champ est considérée dans les expressions que nous avons données, bien que la polarisation ne soit pas purement verticale .

Pour un dipôle orienté verticalement, le champ diffusé détecté est par suite considéré comme approximativement égal à :

$$E_{scat}(\theta_0) \approx E_0 K(r) \frac{k^2}{r} e^{i\omega t} \sin(\theta_0) \alpha_{eff\perp} (1 + r_p(\theta_0))^2 u_\theta. \tag{1.12}$$

La section efficace de diffusion totale de la particule pour les deux polarisations perpendiculaires sont données par:

$$\sigma_{\perp} = \int_{2\pi} d\sigma_{\perp} \propto \frac{\alpha_t^2}{(1-\frac{\alpha_t \beta K_c}{4h^3})^2} \tag{1.13}$$

et

$$\sigma_{\parallel} = \int_{2\pi} d\sigma_{\parallel} \propto \frac{\alpha_t^2}{(1-\frac{\alpha_t \beta K_c}{8h})^2}. \tag{1.14}$$

PiFM

La force photo-induite (PiF) est une force optique détectée par la sonde AFM. Le principe initial de base est de détecter la force optique existant entre le dipôle moléculaire optiquement excité et son image miroir dans une sonde AFM recouverte de métal. L'illumination et la force résultante sont ainsi toutes deux dans la région champ proche.

L'expression de la force dans les champs électromagnétiques suppose la conservation du moment linéaire. Nous pouvons exprimer cette loi de conservation basée sur les équations de Maxwell. A partir de la force de Lorentz, la force totale intégrée sur un volume V est décrite comme :

$$F(r,t) = \int_V [\rho(r,t)E(r,t) + j(r,t) \times B(r,t)]\, dV \tag{1.15}$$

où ρ est la densité de charge et j est la densité de courant. Par suite, on peut obtenir la formule suivante :

$$\nabla \cdot \left[\varepsilon_0 EE - \mu_0 HH - \frac{1}{2}(\varepsilon_0 E^2 + \mu_0 H^2) \overleftrightarrow{I} \right] = \frac{d}{dt} \frac{1}{c^2} [E \times H] + \rho E + j \times B \tag{1.16}$$

L'expression entre parenthèses sur le côté gauche s'appelle le tenseur de contrainte de Maxwell dans le vide, habituellement noté $\overleftrightarrow{T}$[154]. Il est habituellement utilisé dans l'électromagnétisme classique pour représenter l'interaction entre les forces électromagnétiques et le moment mécanique, comme cela sera présenté dans ce qui suit :

$$\overleftrightarrow{T} = \varepsilon_0 EE - \mu_0 HH - \frac{1}{2}(\varepsilon_0 E^2 + \mu_0 H^2) \overleftrightarrow{I} \tag{1.17}$$

La moyenne temporelle du tenseur de contrainte de Maxwell (MST) est donnée par :

$$\left\langle \overleftrightarrow{T}_{i,j} \right\rangle = \varepsilon E_i E_j^* - \mu H_i H_j^* - \frac{1}{2}\delta_{ij}(\varepsilon E^2 + \mu H^2) \tag{1.18}$$

Ce tenseur MST est généralement utilisé pour les méthodes numériques, telles que FDTD et FEM. La force mécanique moyenne devient alors:

$$\langle F \rangle = \oint\!\!\!\!\!\!\int_S \left\langle \overleftrightarrow{T} \right\rangle n da \tag{1.19}$$

Nous considérons maintenant un système constitué d'une particule dipôlaire sur un substrat qui interagit avec une sonde (c.f. Figure 1.3).

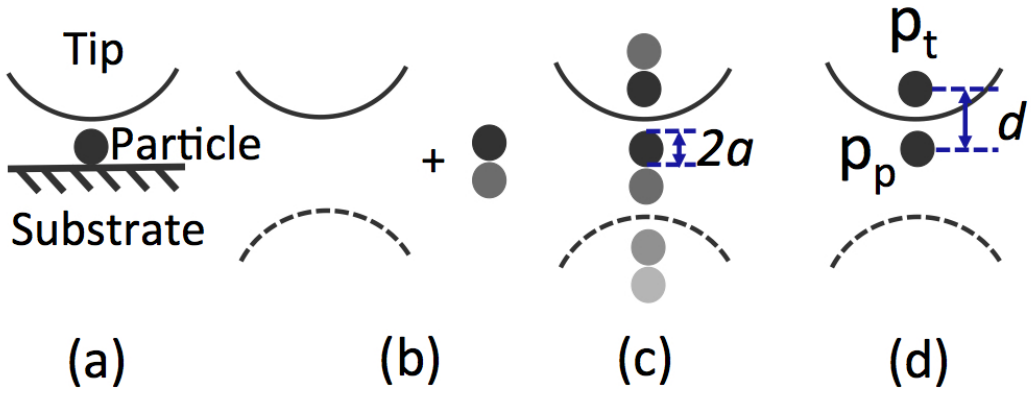

Figure 1.3.: Modèle dipôlaire initial dans un dispositif PiFM. Adapté de[159]

La PiF moyennée dans le temps s'écrit dans ce cas[170, 169] :

$$\langle F \rangle \propto Re\left\{ \sum_i P_i^*(r) \nabla E_i(r) \right\} \quad with \quad i = x, y, z, \tag{1.20}$$

où $P^*(r)$ est la polarisation optiquement induite de la pointe et $E(r)$ est le champ électrique optique au voisinage de la pointe influencée par la polarisation de l'échantillon. Le champ externe est considéré comme décroissant exponentiellement et la force comprend deux termes, une force localisée et une force non localisée. La force moyenne dans le temps peut être exprimée comme:

$$\langle F \rangle = F_{loc} + F_{nloc}. \tag{1.21}$$

F_{loc} est la force localisée. Elle dépend de la distance d entre la pointe et l'échantillon. F_{nloc} est la force non localisée, indépendante de d. Les expressions de ces deux forces s'écrivent :

$$F_{loc} \propto -\frac{1}{d^4} Re\left\{\alpha_p \alpha_t^*\right\} |E_z|^2, \tag{1.22}$$

$$F_{nloc} \propto Im\left\{\alpha_t\right\} |E_x|^2, \tag{1.23}$$

où α_p et α_t sont les polarisabilités de l'échantillon et de la pointe, respectivement et l'expression de la polarisabilité est $\alpha = \alpha' + i\alpha''$. Ici, E_z et $E_x$sont les composantes z et x du champ incident. La raison de la haute résolution spatiale de PiFM est que F_{loc} est proportionnelle à $\frac{1}{d^4}$, ce qui conduit au comportement de la force très localisée en PiFM. A l'inverse, la force non localisée est beaucoup moins confinée spatialement.

2. Partie expérimentale

Dans cette partie du résumé décrivant la partie expérimentale, nous décrivons succinctement les échantillons étudiés, les dispositifs expérimentaux, et nous présentons quelques résultats principaux.

Détails expérimentaux

Nous avons étudié des échantillons HDSC avec s-SNOM et PiFM, qui sont deux techniques de nanoscopie optique basées sur un système AFM. L'imagerie en champ proche et la spectroscopie peuvent être réalisées par ces deux systèmes.

Echantillons HDSC étudiés

Dans ce travail, deux échantillons HDSC, consistant en des nanostructures InAsSb de type n dopées au Si sur un substrat GaSb non dopé, sont étudiés. Les nanostructures HDSC

ont été réalisées par photolithographie et gravure chimique dans le groupe Nanomir[1] par F. Barho.

Le premier échantillon est un réseau sub-longueur d'onde HDSC. A partir de la Figure 2.1, représentant l'image MEB des réseaux HDSC, on peut voir que l'épaisseur de InAsSb fortement dopée est de 100 nm, la largeur de 700 nm et le pas de 1.6 μm.

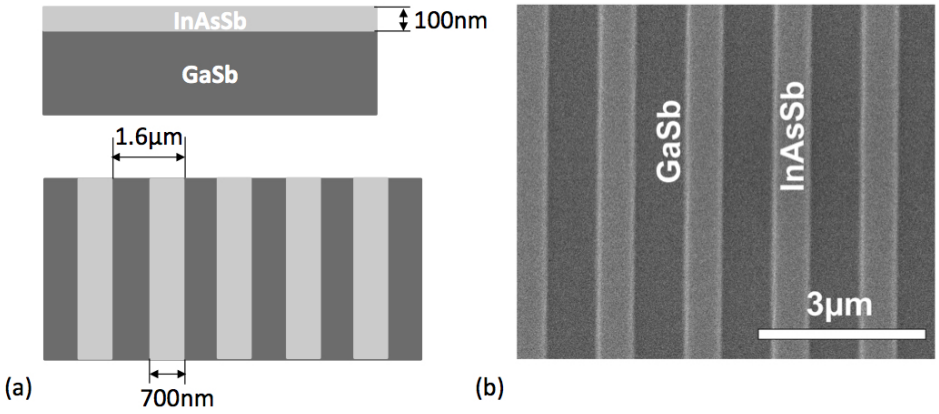

Figure 2.1.: Échantillon: rubans de HDSC: (a) Schéma du réseau; (b) Image MEB.

La dispersion $\varepsilon(\omega)$ des rubans HDSC considérés est bien décrite par le modèle Drude dans la gamme IR étudiée avec $\varepsilon_\infty = 10.4$ la permittivité relative du matériau, et où les deux autres paramètres ω_p et γ sont fonctions de la concentration de dopants et déterminés expérimentalement en modélisant les spectres de réflectivité IR des films minces HDSC[40] (mode de Brewster). La fréquence du plasma ainsi déterminée est ω_p=$(6.64 \pm 0.01) \times 10^{14}$Hz, ce qui correspond à une longueur d'onde de 9.16 μm et le taux de relaxation γ est $(6 \pm 2) \times 10^{12}\ s^{-1}$.

Le second échantillon est formé de nanoantennes rectangulaires périodiques 2D représentées sur la Figure 2.2. Le coté court a du rectangle vaut $400 \pm 30nm$ et le coté long b est de $810 \pm 30nm$. La périodicité selon l'axe court w_a est de 1.4 μm et selon l'axe long la péridode w_b est de 2 μm. Les paramètres de la fonction diélectrique sont $\varepsilon_\infty = 10.4$, $\gamma = 1 \times 10^{13} s^{-1}$ et $\omega_p = 1.157 \times 10^{15}$Hz, ce qui correspond à une longueur d'onde de 5,25 μm.

[1]IES, Montpellier

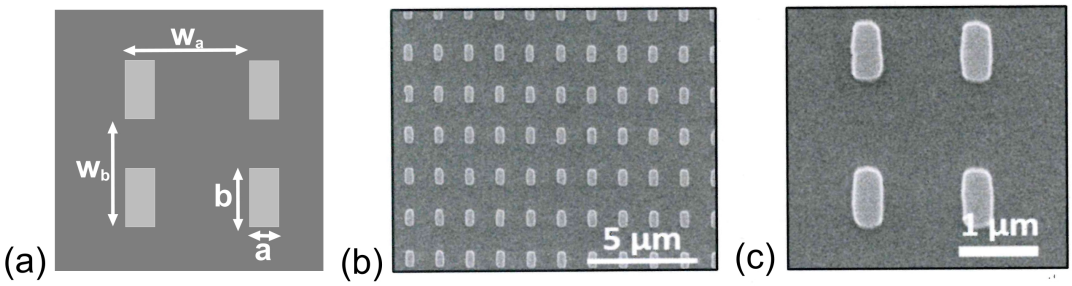

Figure 2.2.: Schéma des nanoantennes 2D: (a) Nanoantennes rectangulaires périodiques 2D; (b) Image SEM; (c) Détail de l'image SEM (a) montrant les coins arrondis des nanoantennes rectangulaires.[173]

Dispositif s-SNOM (microscopie de champ proche optique à sonde diffusante)

Pour l'étude des propriétés plasmonique de nos échantillons fortement dopés, on utilise un s-SNOM interférométrique développé au laboratoire, notamment aux travers des thèses de Z. Sedagath et A. Al Mohtar. Le système sonde-échantillon est placé dans le bras d'un interféromètre de Michelson, et une modulation sinusoidale de phase est réalisée dans le bras de référence. Nous utilisons maintenant des fibres monomodes dans l'IR moyen pour faciliter l'utilisation de différents lasers et nous pouvons réaliser un spectre allant de 9,1 µm à 11,4 µm. La sonde est fabriquée par une méthode de gravure électrochimique, "double lamellae dropoff technique". Les détails de cette fabrication et du dispositif peuvent être trouvés dans le manuscrit. Une méthode électronique d'extraction appelée détection GLIA (Generalized Lock-In Amplifier) est utilisée dans l'expérience afin d'extraire l'amplitude et la phase du signal optique diffusé en champ proche. La configuration s-SNOM expérimentale est détaillée dans la section 2.3.

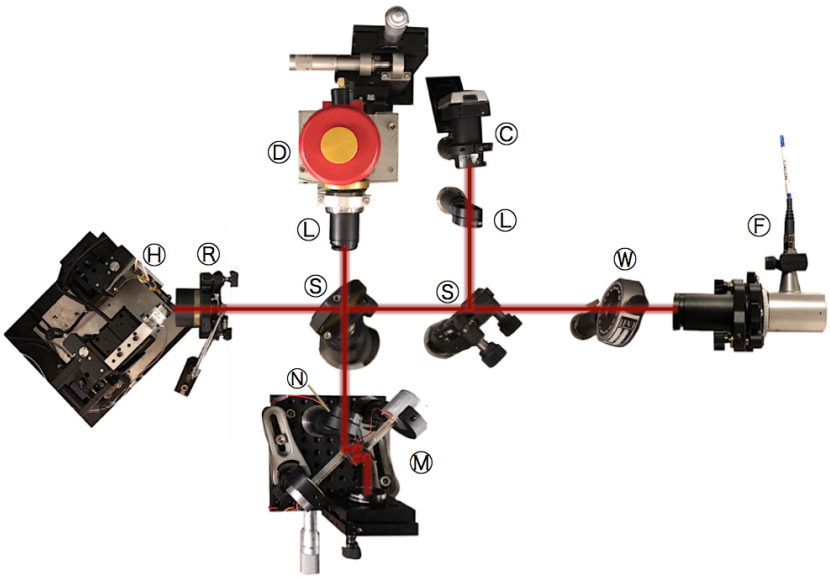

Figure 2.3.: Configuration s-SNOM: F: fibre mid-IR avec collimateur, W: lame demi-onde, C: caméra visible, L: lentille, S: diviseur de faisceau, D: détecteur HgCdTe, R: objectif réfléchissant, H: Tête AFM comprenant des étages moteurs et piézos. ND: Filtre de densité neutre, M: Miroir monté sur des piézoélectriques.

PiFM system (Photo-induced force microscope)

Le PiFM commercial de Molecular Vista, Inc est utilisé dans cette étude (montré sur la Figure 2.4). Le système dispose de deux détections synchrones qui collectent les données de topographie à la fréquence f_m (première résonance mécanique de la sonde) et la force de gradient photo-induite à f_0 (seconde résonance mécanique de la sonde) simultanément. Pour tirer parti du facteur de qualité Q du levier AFM et améliorer la sensibilité, on choisi la valeur $f_m \pm f_0$ comme fréquence de modulation du laser externe éclairant la nanosonde pour que la force de gradient se situe à f_0.

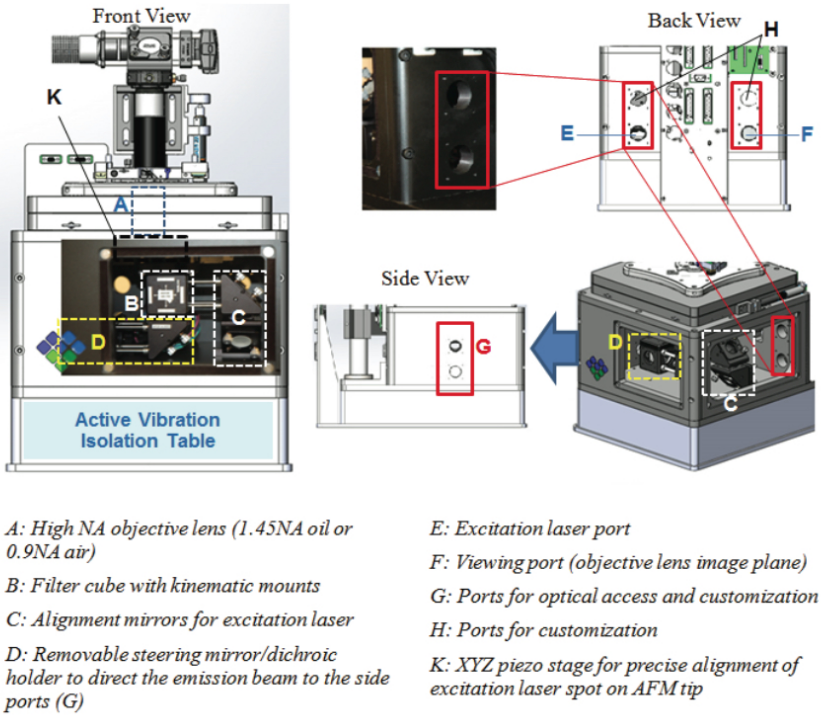

Figure 2.4.: Système PiFM: schéma des différentes vues de PiFM (adapté de[160])

Le PiFM peut être utilisé pour imager des échantillons transparents par une illumination en transmission (i.e. à travers l'échantillon), et des échantillons opaques par illumination supérieure en réflexion. Sur le dispositif expérimental, deux chemins optiques permettent en effet au PiFM de travailler sur ces deux modes : le mode transmission et le mode réflexion. Selon le cas, la source d'excitation est focalisée soit par un miroir parabolique situé sur le coté (en réflexion), soit par un objectif (en transmission).

Caractérisation champ proche et analyse

Les images optiques et les spectres réalisés par les deux outils sont ici présentés, accompagnés de simulations analytiques et FDTD afin d'interpréter et de comparer la nature du signal obtenu sur les deux systèmes. Nous présentons une série d'images d'amplitude et de phase optiques à différentes longueurs d'onde dans la gamme des lasers QCL. Les images sélectionnées sont représentées sur la figure 2.5. Les Figures 2.5 (a) et (b) représentent

l'image de topographie AFM et le profil du réseau respectivement. La polarisation du faisceau incident est fixée le long de l'axe de la pointe pour obtenir un signal rétrodiffusé maximal.

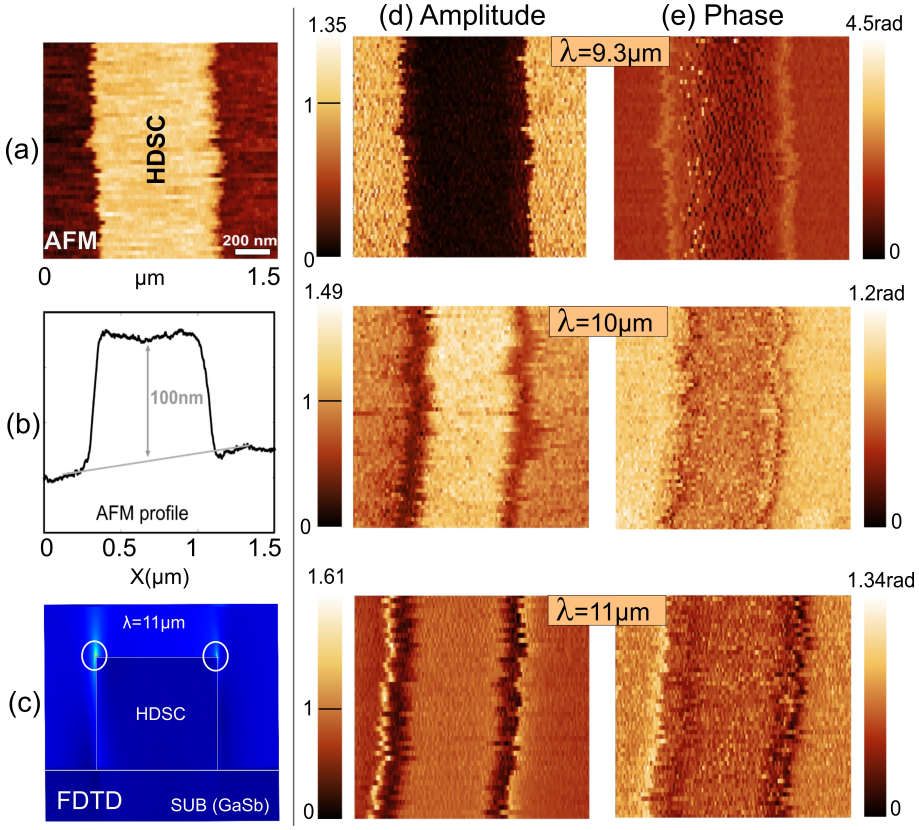

Figure 2.5.: Images s-SNOM des réseaux HDSC. (a) Topographie (b) Profil de la topographie; (c) simulation FDTD du réseau HDS à une longueur d'onde de 11 µm; (d) images d'amplitude optique à une longueur d'onde de 9,3 µm, 10 µm, et 11 µm (l'échelle des barres de couleur est normalisée par l'amplitude optique sur le substrat GaSb); (e): Images de phase optique à 9,3 µm, 10 µm, 11 µm de longueur d'onde.

- À 9.3 µm, où nous approchons de la région ENZ, la surface HDSC est sombre par rapport au substrat (Figure 2.5 (d), en haut).

- À10 µm, au contraire, pour une valeur de permittivité légèrement plus faible, le signal de champ proche sur le HDSC est maximal produisant un contraste opposé entre le HDSC et le substrat de GaSb.

- À 11 μm, on observe enfin des bords brillants pouvant être associés à une résonance plasmonique de surface localisée extrêmement-confinée (LSPR). La dissymétrie observée sur l'image d'amplitude entre les deux bords est due à la condition d'éclairement latéral, qui est bien reproduite par simulation électromagnétique.

Pour générer le spectre des réseaux HDSC (Figure 2.6), on normalise chaque point du signal, tant en amplitude qu'en phase, par la réponse sur le substrat GaSb non dopé. Le signal s-SNOM relatif sur HDSC, A_{HDSC}/A_{SUB} est modélisé en utilisant $A = \sqrt{\sigma_{\perp}(\theta)}\left|1+r_p(\theta)\right|$, avec $\sigma_{\perp}(\theta)$ la section efficace de diffusion différentielle d'une nano-sphère polarisable verticalement. Ce signal est proportionnel à $|\alpha_{eff,z}|$ et le facteur $\left|1+r_p(\theta)\right|$ est lié à la prise en compte du champ d'illumination qui se réfléchit également sur la surface considérée. A partir de la Figure 2.6(a) nous pouvons voir que pour l'intensité s-SNOM, un signal proportionnel à $|\alpha_{eff,z}|^2$, correspond bien au signal observé.

Un lien entre LDOS et phase optique a également été prédit dans un article récent sur l'information contenue dans le signal de phase diffusé par des sondes diélectriques. Expérimentalement, nous pouvons effectivement observer une certaine correspondance entre le spectre de phase mesuré et la LDOS partielle attendue. En utilisant la méthode FDTD sous le logiciel Lumerical, nous calculons la LDOS au centre du réseau (hauteur de 100 nm) par rapport à la LDOS du vide, le résultat est représenté sur la Figure 2.6(b).

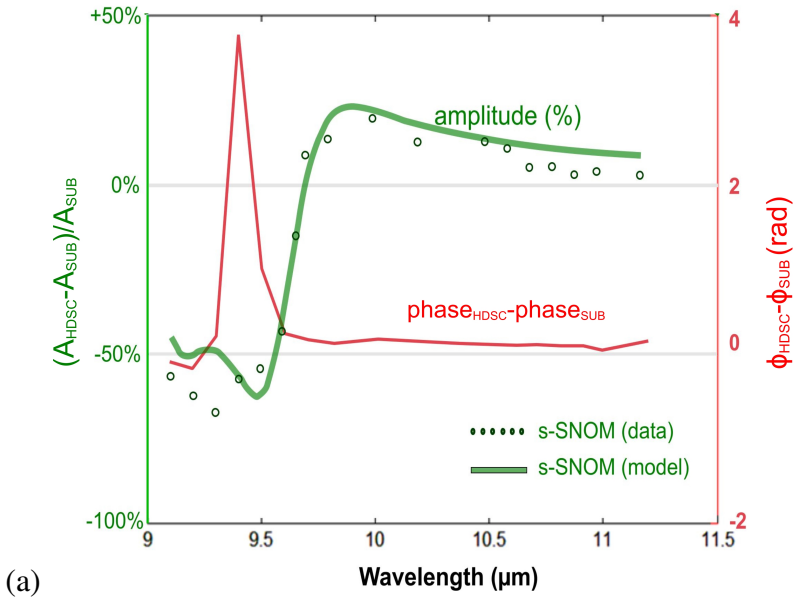

(a)

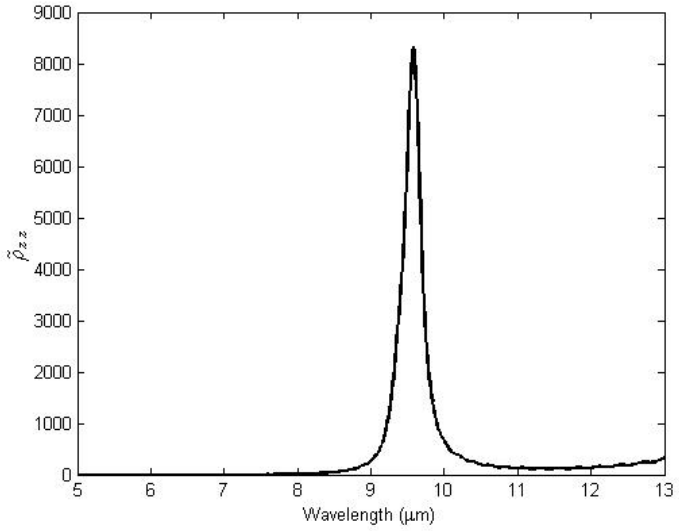

(b)

Figure 2.6.: Spectres de champ proche s-SNOM sur le HDSC par rapport au signal du substrat (obtenu avec une sonde de tungstène). (a) Courbe rouge: différence de phase entre le HDSC et le substrat. Cercles et ligne verte: signal expérimental s-SNOM et simulation respectivement; (b) LDOS normalisée.

Des images assez similaires aux images s-SNOM d'amplitude sont obtenues par PiFM, comme représenté sur la figure2.7 pour des longueurs d'onde sélectionnées. Ce signal PiFM est obtenu en utilisant des sondes AFM de type cantilever en silicium, métalisées

avec de l'or. Tout comme pour les images s-SNOM, nous observons effectivement une résonance induite par l'échantillon où le signal PiFM passe d'une valeur faible dans la région ENZ à une valeur beaucoup plus grande pour une valeur légèrement négative de ε sur la figure 2.7 (a) and (b). Nous notons la signature d'une résonance localisée (LSPR), associée à un champ très confiné, au voisinage de 11 µm comme le montre l'image haute résolution sur la figure 2.7 (c).

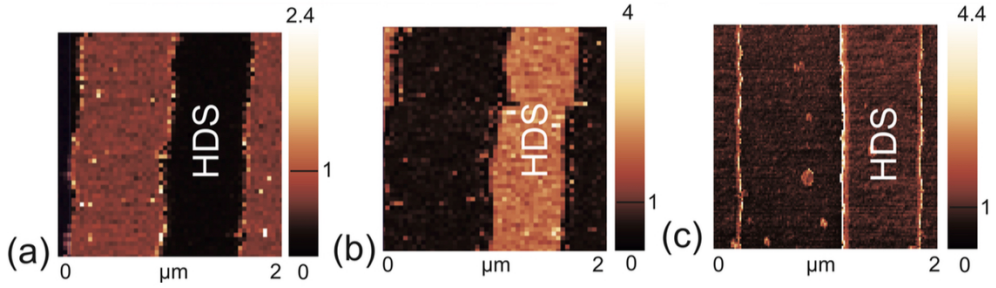

Figure 2.7.: Images PiFM de réseaux HDSC. (a) - (c): images PiFM à 9,02 µm, 10,53 µm et 10,8 µm (l'échelle de la gamme de couleurs est normalisée par l'amplitude optique sur le substrat GaSb).

Le spectre PiFM normalisé par la réponse PiFM du substrat GaSb et les simulations associées sont représentés sur la Figure 2.8. Ici, le modèle dipolaire usuellement appliqué en PiFM ne peut être raisonablement utilisé car la sonde n'est pas plus grande que la particule sous la sonde (l'échantillon). Au contraire, l'extrémité de la sonde est très petite en regard de l'extension latérale des motifs du réseau. Nous considérons ainsi, qu'à l'inverse, c'est la sonde qui peut être assimilée à un dipôle, comme il est généralement considéré dans l'analyse du signal en s-SNOM. L'expression de la force dans le cas d'un dipôle est discuté par ailleurs[172, 154]. Ici nous introduisons cependant la polarisabilité effective du système sonde-échantillon pour rendre compte du champ en extrémité de sonde, en incluant le champ auto-induit. Avec quelques hypothèses, nous obtenons l'expression simple suivante de pour force moyenne nette:

$$< F_z >= C|\alpha_{eff}|^2 \tag{2.1}$$

où le facteur de proportionnalité est donné par $C = \frac{1}{2a}|E_{i,z}|^2 Re(\frac{1}{\alpha})$.

Selon le mode de fonctionnement considéré du PiFM, le signal détecté peut être également sensible à la dérivée de $< F_z >$ par rapport à z. Cette contribution est s'écrit alors:

$$< F_z >'_z = \frac{6K_c}{h^4} < F_z > Re(\beta \alpha^*_{eff} \alpha) \tag{2.2}$$

A partir de Figure 2.8 on peut voir que le signal de force est correctement modélisé avec le modèle simple dipôle de sonde que nous avons proposé. Comme l'indique l'équation 5.1.5, l'expression de la force moyennée dans le temps $< F_z > \propto |\alpha_{eff,z}|^2$ considère l'interaction entre le champ local décrit par $\alpha_{eff,z}$ et une charge ponctuelle unique proportionnelle au moment dipolaire induit p également proportionnelle à $\alpha_{eff,z}$. Les données analytiques PiFM sont ici modélisées en utilisant une distance négligeable entre le sommet de la sonde et le substrat. Ces résultats sont interessants car il est souvent avancé que le PiFM pourrait être essentiellement sensible à une information de type purement "AFM", en raison d'une expansion photoinduite sur les résonances d'absorption de l'échantillon. Ici cependant, le signal de force est correctement ajusté avec l'approximation dipolaire sans recourir à une éventuelle photoexpansion induite.

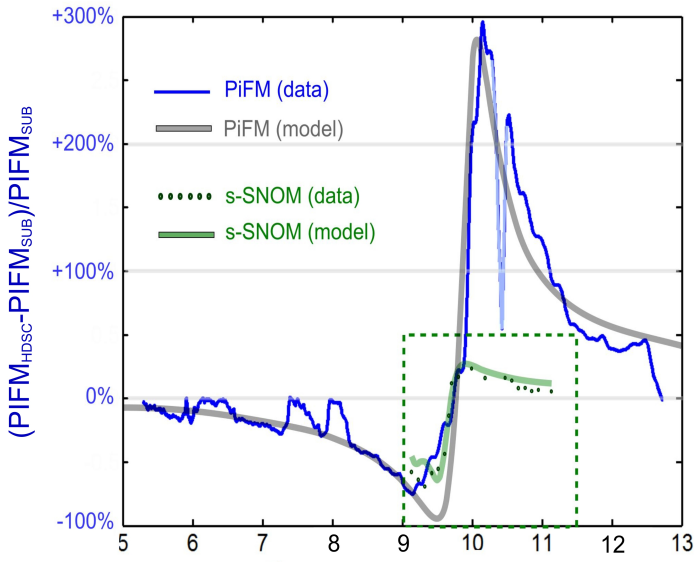

Figure 2.8.: Spectres de champ proche sur le HDSC par rapport au signal de substrat obtenu avec PiFM (sonde de silicium recouverte d'or). Courbes bleues et grises: signal expérimental PiFM et simulation analytique respectivement. Cercles et ligne verte: signal expérimental s-SNOM et simulation respectivement.

Finalement, nous considérons le mode LSPR d'un réseau de nanoantennes périodique 2D en s-SNOM. À 10,8 μm, nous pouvons effectivement observer un champ confiné au bord et en bas des nanoantennes, comme représenté sur les Figures 2.9 (b) et (c). Sur la Figure 2.9(c), le double bord lumineux est attribué à une altération de la sonde. La dissymétrie constatée est attendue en raison de l'angle de l'éclairage incident. La simulation FDTD, Figure 2.9(e), produit le même effet.

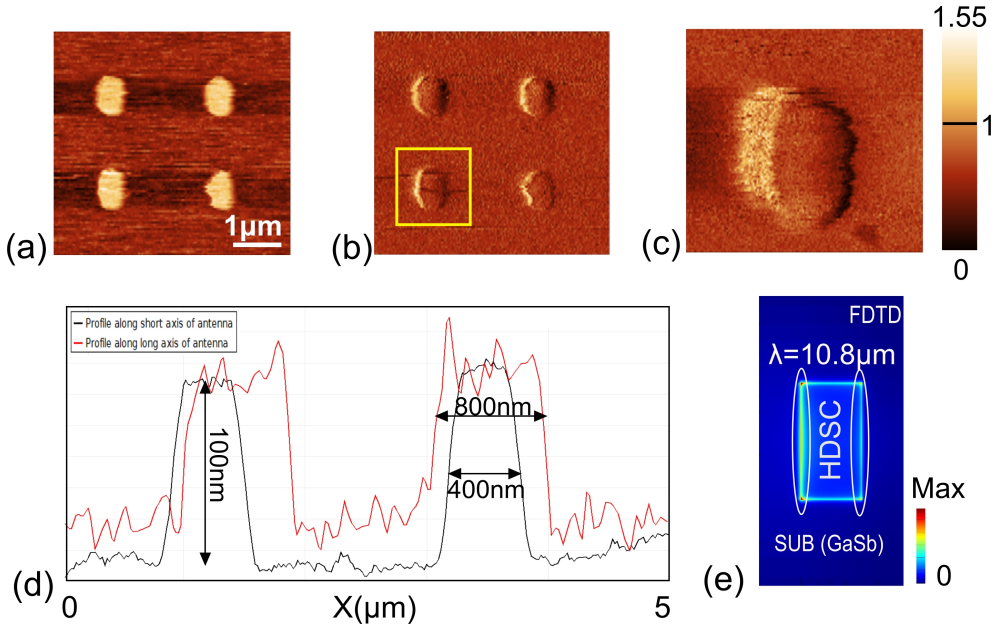

Figure 2.9.: Image s-SNOM de l'échantillon 2D: (a) Topographie de l'échantillon; (b) Amplitude optique; (c) Zoom; (d) Profil de topographie, la courbe noire est le profil le long de l'axe court et la courbe rouge le long de l'axe long; (e) Simulation FDTD de la distribution de champ (plan XY).

Conclusion

En conclusion, des échantillons nanostructurés de HDSC ont été étudiés par nanoscopie spectroscopique en champ proche au voisnage de la fréquence plasma (réseau 1D) et au voisinage d'une résonance LSPR (réseau 2D). Deux techniques de champ proche, s-SNOM (phase-sensitive) et PiFM ont été utilisées pour étudier les réseaux 1D de HDSC, et les informations sur la distribution locale du champ et la permittivité complexe ont été obtenues.

Pour les deux techniques, des modèles analytiques basés sur l'approximation dipolaire ont été utilisés pour modéliser les spectres expérimentaux obtenus. Concernant la modélisation analytique du signal, nous avons proposé d'adapter l'approximation dipolaire classiquement utilisée pour les sondes s-SNOM dans l'IR au cas du PiFM, dans la mesure où la sonde est nettement plus petite que les nanostructures étudiées.

L'imagerie par spectroscopie s-SNOM et PiFM a été réalisée sur des réseaux HDSC ayant une fonction diélectrique connue. Le spectre PiFM présente une résonance d'origine

principalement non dissipative comme pour le s-SNOM, ce qui indique que le signal n'est pas apparemment associé ici à une expansion photoinduite. De plus, des signatures de LSPR sur les bords des motifs du réseau 1D en HDSC ont également été observées avec les deux techniques, bien que légèrement décalées par rapport aux simulations effectuées sur des structures de forme carrée idéales, sans sonde. L'origine de ce décalage peut par ailleurs être expliquée par une légère oxidation, connue, en surface du matériau HDSC. Pour les nanoantennes rectangulaires en HDSC, des images s-SNOM ont été obtenues et l'exaltation du champ local au bord des nanoantennes est clairement visible sur ces images.

Bien que non décrit dans ce résumé, d'un point de vue expérimental, nous avons également développé un système interférométrique afin de pouvoir utiliser un laser IR en mode CW pour la mesure PiFM au lieu d'un laser pulsé. Dans un proche avenir, la réalisation de mesures simultanées de PiFM et s-SNOM avec une même sonde devrait permettre de comparer plus quantitativement les signaux spectroscopiques et plus particulièrement d'évaluer si les modèles phénoménologiques proposés ou des modèles plus avancés peuvent rendre compte du signal de PiFM et s-SNOM.

Bibliography

[1] Joseph Sweetman Ames. Prismatic and diffraction spectra: memoirs by joseph von fraunhofer. *Harper's Scientific Memoirs, Harper and Brothers Publications, New York*, 1898.

[2] Sabine Petit, François Martin, Andrzej Wiewiora, Philippe De Parseval, and Alain Decarreau. Crystal-chemistry of talc: A near infrared (nir) spectroscopy study. *American Mineralogist*, 89(2-3):319–326, 2004.

[3] KV Emtsev, F Speck, Th Seyller, L Ley, and John Douglas Riley. Interaction, growth, and ordering of epitaxial graphene on sic {0001} surfaces: A comparative photoelectron spectroscopy study. *Physical Review B*, 77(15):155303, 2008.

[4] Xavier Crispin, S Marciniak, Wojciech Osikowicz, G Zotti, AW van der Gon, F Louwet, Mats Fahlman, L Groenendaal, Frans De Schryver, and William R Salaneck. Conductivity, morphology, interfacial chemistry, and stability of poly (3, 4-ethylene dioxythiophene)–poly (styrene sulfonate): A photoelectron spectroscopy study. *Journal of polymer science Part B: Polymer physics*, 41(21):2561–2583, 2003.

[5] Arno Villringer, J Planck, C Hock, L Schleinkofer, and U Dirnagl. Near infrared spectroscopy (nirs): a new tool to study hemodynamic changes during activation of brain function in human adults. *Neuroscience letters*, 154(1):101–104, 1993.

[6] M Krssak, K Falk Petersen, A Dresner, L DiPietro, SM Vogel, DL Rothman, GI Shulman, and M Roden. Intramyocellular lipid concentrations are correlated with insulin sensitivity in humans: a 1h nmr spectroscopy study. *Diabetologia*, 42(1):113–116, 1999.

[7] Zhen Hua Ni, Ting Yu, Yun Hao Lu, Ying Ying Wang, Yuan Ping Feng, and Ze Xiang Shen. Uniaxial strain on graphene: Raman spectroscopy study and band-gap opening. *ACS nano*, 2(11):2301–2305, 2008.

[8] John-David T Smith, BT Draine, DA Dale, J Moustakas, RC Kennicutt Jr, G Helou, L Armus, H Roussel, K Sheth, GJ Bendo, et al. The mid-infrared spectrum of star-forming galaxies: global properties of polycyclic aromatic hydrocarbon emission. *The Astrophysical Journal*, 656(2):770, 2007.

[9] Yujun Zhong, Shyamala Devi Malagari, Travis Hamilton, and Daniel M Wasserman. Review of mid-infrared plasmonic materials. *Journal of Nanophotonics*, 9(1):093791, 2015.

[10] Hai Hu, Xiaoxia Yang, Feng Zhai, Debo Hu, Ruina Liu, Kaihui Liu, Zhipei Sun, and Qing Dai. Far-field nanoscale infrared spectroscopy of vibrational fingerprints of molecules with graphene plasmons. *Nature communications*, 7:12334, 2016.

[11] Lifu Xiao and Zachary D Schultz. Spectroscopic imaging at the nanoscale: Technologies and recent applications. *Analytical chemistry*, 90(1):440–458, 2017.

[12] Alexander A Govyadinov, Iban Amenabar, Florian Huth, P Scott Carney, and Rainer Hillenbrand. Quantitative measurement of local infrared absorption and dielectric function with tip-enhanced near-field microscopy. *The journal of physical chemistry letters*, 4(9):1526–1531, 2013.

[13] Alexander S. McLeod, P. Kelly, M. D. Goldflam, Z. Gainsforth, A. J. Westphal, Gerardo Dominguez, Mark H. Thiemens, Michael M. Fogler, and D. N. Basov. Model for quantitative tip-enhanced spectroscopy and the extraction of nanoscale-resolved optical constants. *Phys. Rev. B*, 90:085136, Aug 2014.

[14] Agnes Bogner, P-H Jouneau, Gilbert Thollet, D Basset, and Catherine Gauthier. A history of scanning electron microscopy developments: towards wet-stem imaging. *Micron*, 38(4):390–401, 2007.

[15] F Zenhausern, Y Martin, and HK Wickramasinghe. Scanning interferometric apertureless microscopy: optical imaging at 10 angstrom resolution. *Science*, 269(5227):1083, 1995.

[16] Fritz Keilmann and Rainer Hillenbrand. Near-field microscopy by elastic light scattering from a tip. *PHILOSOPHICAL TRANSACTIONS-ROYAL SOCIETY OF LONDON SERIES A MATHEMATICAL PHYSICAL AND ENGINEERING SCIENCES*, pages 787–806, 2004.

[17] Lukas Novotny and Stephan J Stranick. Near-field optical microscopy and spectroscopy with pointed probes. *Annu. Rev. Phys. Chem.*, 57:303–331, 2006.

[18] Florian Huth, Alexander Govyadinov, Sergiu Amarie, Wiwat Nuansing, Fritz Keilmann, and Rainer Hillenbrand. Nano-ftir absorption spectroscopy of molecular fingerprints at 20 nm spatial resolution. *Nano letters*, 12(8):3973–3978, 2012.

[19] Jens Steidtner and Bruno Pettinger. Tip-enhanced raman spectroscopy and microscopy on single dye molecules with 15 nm resolution. *Physical Review Letters*, 100(23):236101, 2008.

[20] R Zhang, Y Zhang, ZC Dong, S Jiang, C Zhang, LG Chen, L Zhang, Y Liao, J Aizpurua, Y ea Luo, et al. Chemical mapping of a single molecule by plasmon-enhanced raman scattering. *Nature*, 498(7452):82, 2013.

[21] Sandro Mignuzzi, Fumin Huang, Debdulal Roy, and David Richards. Near-field raman enhancement of single molecules and point scatterers. *The Journal of Physical Chemistry C*, 121(34):18800–18806, 2017.

[22] Alexandre Dazzi and Craig B Prater. Afm-ir: technology and applications in nanoscale infrared spectroscopy and chemical imaging. *Chemical reviews*, 117(7):5146–5173, 2016.

[23] Aaron M Katzenmeyer, Vladimir Aksyuk, and Andrea Centrone. Nanoscale infrared spectroscopy: improving the spectral range of the photothermal induced resonance technique. *Analytical chemistry*, 85(4):1972–1979, 2013.

[24] Feng Lu, Mingzhou Jin, and Mikhail A Belkin. Tip-enhanced infrared nanospectroscopy via molecular expansion force detection. *Nature photonics*, 8(4):307, 2014.

[25] Derek Nowak, William Morrison, H Kumar Wickramasinghe, Junghoon Jahng, Eric Potma, Lei Wan, Ricardo Ruiz, Thomas R Albrecht, Kristin Schmidt, Jane Frommer, et al. Nanoscale chemical imaging by photoinduced force microscopy. *Science advances*, 2(3):e1501571, 2016.

[26] Ryan A Murdick, William Morrison, Derek Nowak, Thomas R Albrecht, Junghoon Jahng, and Sung Park. Photoinduced force microscopy: A technique for hyperspectral nanochemical mapping. *Japanese Journal of Applied Physics*, 56(8):08LA04, 2017.

[27] Le Wang, Haomin Wang, Martin Wagner, Yong Yan, Devon S Jakob, and Xiaoji G Xu. Nanoscale simultaneous chemical and mechanical imaging via peak force infrared microscopy. *Science advances*, 3(6):e1700255, 2017.

[28] R Prasad and R Vincent. Resolving phase information of the optical local density of state with scattering near-field probes. *Physical Review B*, 94(16):165440, 2016.

[29] L Novotny and C Hafner. Light propagation in a cylindrical waveguide with a complex, metallic, dielectric function. *Physical review E*, 50(5):4094, 1994.

[30] Julia WP Hsu. Near-field scanning optical microscopy studies of electronic and photonic materials and devices. *Materials Science and Engineering: R: Reports*, 33(1):1–50, 2001.

[31] Fei Huang, Venkata Ananth Tamma, Zahra Mardy, Jonathan Burdett, and H Kumar Wickramasinghe. Imaging nanoscale electromagnetic near-field distributions using optical forces. *Scientific reports*, 5, 2015.

[32] V N'Tsame Guilengui, L Cerutti, J-B Rodriguez, E Tournié, and T Taliercio. Localized surface plasmon resonances in highly doped semiconductors nanostructures. *Applied Physics Letters*, 101(16):161113, 2012.

[33] MJ Milla, F Barho, F González-Posada, L Cerutti, M Bomers, JB Rodriguez, E Tournié, and T Taliercio. Localized surface plasmon resonance frequency tuning in highly doped inassb/gasb one-dimensional nanostructures. *Nanotechnology*, 27(42):425201, 2016.

[34] Franziska B Barho, Fernando Gonzalez-Posada, Maria-José Milla-Rodrigo, Mario Bomers, Laurent Cerutti, and Thierry Taliercio. All-semiconductor plasmonic gratings for biosensing applications in the mid-infrared spectral range. *Optics express*, 24(14):16175–16190, 2016.

[35] R Hillenbrand, T Taubner, and F Keilmann. Phonon-enhanced light-matter interaction at the nanometre scale. *Nature*, 418(6894):159–162, 2002.

[36] M Shamseddine, M Kazan, and M Tabbal. Model for the unpolarized infrared reflectivity from uniaxial polar materials: Effects of anisotropy, free carriers, and defects. *Infrared Physics and Technology*, 55(1):112–121, 2012.

[37] Stephanie Law, Lan Yu, Aaron Rosenberg, and Daniel Wasserman. All-semiconductor plasmonic nanoantennas for infrared sensing. *Nano letters*, 13(9):4569–4574, 2013.

[38] Jacob B Khurgin and Alexandra Boltasseva. Reflecting upon the losses in plasmonics and metamaterials. *MRS bulletin*, 37(8):768–779, 2012.

[39] WG Spitzer and HY Fan. Determination of optical constants and carrier effective mass of semiconductors. *Physical Review*, 106(5):882, 1957.

[40] Thierry Taliercio, Vilianne Ntsame Guilengui, Laurent Cerutti, Eric Tournié, and Jean-Jacques Greffet. Brewster mode in highly doped semiconductor layers: an all-optical technique to monitor doping concentration. *Optics Express*, 22(20):24294–24303, 2014.

[41] Peter R Griffiths and James A De Haseth. *Fourier transform infrared spectrometry*, volume 171. John Wiley & Sons, 2007.

[42] Sieghard Albert, Karen Keppler Albert, and Martin Quack. High-resolution fourier transform infrared spectroscopy. *Handbook of High-Resolution Spectroscopy*, 2011.

[43] Peter R Griffiths, Howard J Sloane, and Robert W Hannah. Interferometers vs monochromators: separating the optical and digital advantages. *Applied Spectroscopy*, 31(6):485–495, 1977.

[44] Peter Fellgett. I.âles principes généraux des méthodes nouvelles en spectroscopie interférentielle-a propos de la théorie du spectromètre interférentiel multiplex. *J. phys. radium*, 19(3):187–191, 1958.

[45] JA Dionne, LA Sweatlock, HA Atwater, and A Polman. Planar metal plasmon waveguides: frequency-dependent dispersion, propagation, localization, and loss beyond the free electron model. *Physical Review B*, 72(7):075405, 2005.

[46] Jongbum Kim, Aveek Dutta, Gururaj V Naik, Alexander J Giles, Francisco J Bezares, Chase T Ellis, Joseph G Tischler, Ahmed M Mahmoud, Humeyra Caglayan, Orest J Glembocki, et al. Role of epsilon-near-zero substrates in the optical response of plasmonic antennas. *Optica*, 3(3):339–346, 2016.

[47] Simon Vassant, Jean-Paul Hugonin, Francois Marquier, and Jean-Jacques Greffet. Berreman mode and epsilon near zero mode. *Optics express*, 20(21):23971–23977, 2012.

[48] Salvatore Campione, Igal Brener, and Francois Marquier. Theory of epsilon-near-zero modes in ultrathin films. 91, 03 2015.

[49] Timur Shaykhutdinov, Andreas Furchner, Jörg Rappich, and Karsten Hinrichs. Mid-infrared nanospectroscopy of berreman mode and epsilon-near-zero local field confinement in thin films. *Optical Materials Express*, 7(10):3706–3714, 2017.

[50] Salvatore Campione, Igal Brener, and Francois Marquier. Theory of epsilon-near-zero modes in ultrathin films. *Physical Review B*, 91(12):121408, 2015.

[51] R Vincent, JI Juaristi, and P Apell. Geometry and surface plasmon energy. *arXiv preprint arXiv:1103.2086*, 2011.

[52] Jacob B Khurgin. How to deal with the loss in plasmonics and metamaterials. *Nature nanotechnology*, 10(1):2, 2015.

[53] Gururaj V Naik, Vladimir M Shalaev, and Alexandra Boltasseva. Alternative plasmonic materials: beyond gold and silver. *Advanced Materials*, 25(24):3264–3294, 2013.

[54] Jorge Pérez-Juste, Isabel Pastoriza-Santos, Luis M Liz-Marzán, and Paul Mulvaney. Gold nanorods: synthesis, characterization and applications. *Coordination Chemistry Reviews*, 249(17-18):1870–1901, 2005.

[55] Leif J Sherry, Rongchao Jin, Chad A Mirkin, George C Schatz, and Richard P Van Duyne. Localized surface plasmon resonance spectroscopy of single silver triangular nanoprisms. *Nano letters*, 6(9):2060–2065, 2006.

[56] Rizia Bardhan, Shaunak Mukherjee, Nikolay A Mirin, Stephen D Levit, Peter Nordlander, and Naomi J Halas. Nanosphere-in-a-nanoshell: A simple nanomatryushka. *J. Phys. Chem*, 100(114):7378–7383, 2010.

[57] S Law, DC Adams, AM Taylor, and D Wasserman. Mid-infrared designer metals. *Optics express*, 20(11):12155–12165, 2012.

[58] Alexandra Boltasseva and Harry A Atwater. Low-loss plasmonic metamaterials. *Science*, 331(6015):290–291, 2011.

[59] Jacob B Khurgin and Greg Sun. Practicality of compensating the loss in the plasmonic waveguides using semiconductor gain medium. *Applied Physics Letters*, 100(1):011105, 2012.

[60] James C Ginn, Robert L Jarecki Jr, Eric A Shaner, and Paul S Davids. Infrared plasmons on heavily-doped silicon. *Journal of Applied Physics*, 110(4):043110, 2011.

[61] Monas Shahzad, Gautam Medhi, Robert E Peale, Walter R Buchwald, Justin W Cleary, Richard Soref, Glenn D Boreman, and Oliver Edwards. Infrared surface

plasmons on heavily doped silicon. *Journal of Applied Physics*, 110(12):123105, 2011.

[62] David J Rowe, Jong Seok Jeong, K Andre Mkhoyan, and Uwe R Kortshagen. Phosphorus-doped silicon nanocrystals exhibiting mid-infrared localized surface plasmon resonance. *Nano letters*, 13(3):1317–1322, 2013.

[63] Li-Wei Chou, Dmitriy S Boyuk, and Michael A Filler. Optically abrupt localized surface plasmon resonances in si nanowires by mitigation of carrier density gradients. *ACS nano*, 9(2):1250–1256, 2015.

[64] Richard Soref. Mid-infrared photonics in silicon and germanium. *Nature photonics*, 4(8):495, 2010.

[65] Richard Soref, Joshua Hendrickson, and Justin W Cleary. Mid-to long-wavelength infrared plasmonic-photonics using heavily doped n-ge/ge and n-gesn/gesn heterostructures. *Optics express*, 20(4):3814–3824, 2012.

[66] Leonetta Baldassarre, Emilie Sakat, Jacopo Frigerio, Antonio Samarelli, Kevin Gallacher, Eugenio Calandrini, Giovanni Isella, Douglas J Paul, Michele Ortolani, and Paolo Biagioni. Midinfrared plasmon-enhanced spectroscopy with germanium antennas on silicon substrates. *Nano letters*, 15(11):7225–7231, 2015.

[67] JR Haynes and W Shockley. The mobility and life of injected holes and electrons in germanium. *Physical Review*, 81(5):835, 1951.

[68] Fo A Trumbore. Solid solubilities of impurity elements in germanium and silicon. *Bell Labs Technical Journal*, 39(1):205–233, 1960.

[69] Robert F Davis. Iii-v nitrides for electronic and optoelectronic applications. *Proceedings of the IEEE*, 79(5):702–712, 1991.

[70] H Ohno, D Chiba, F Matsukura, T Omiya, E Abe, T Dietl, Y Ohno, and K Ohtani. Electric-field control of ferromagnetism. *Nature*, 408(6815):944, 2000.

[71] Hannah J Joyce, Qiang Gao, H Hoe Tan, Chennupati Jagadish, Yong Kim, Jin Zou, Leigh M Smith, Howard E Jackson, Jan M Yarrison-Rice, Patrick Parkinson, et al. Iii–v semiconductor nanowires for optoelectronic device applications. *Progress in Quantum Electronics*, 35(2-3):23–75, 2011.

[72] CK Williams, TH Glisson, JR Hauser, and MA Littlejohn. Energy bandgap and lattice constant contours of iii-v quaternary alloys of the form ax by cz d or abx cy dz. *Journal of Electronic Materials*, 7(5):639–646, 1978.

[73] Martin A Afromowitz. Refractive index of ga1- xalxas. *Solid State Communications*, 15(1):59–63, 1974.

[74] JH Neave, PJ Dobson, JJ Harris, P Dawson, and BA Joyce. Silicon doping of mbe-grown gaas films. *Applied Physics A*, 32(4):195–200, 1983.

[75] W Walukiewicz. Intrinsic limitations to the doping of wide-gap semiconductors. *Physica B: Condensed Matter*, 302:123–134, 2001.

[76] Takumi Yamada, Eisuke Tokumitsu, Koki Saito, Takeshi Akatsuka, Motoya Miyauchi, Makoto Konagai, and Kiyoshi Takahashi. Heavily carbon doped p-type gaas and gaalas grown by metalorganic molecular beam epitaxy. *Journal of Crystal Growth*, 95(1-4):145–149, 1989.

[77] Debin Li and CZ Ning. All-semiconductor active plasmonic system in mid-infrared wavelengths. *Optics express*, 19(15):14594–14603, 2011.

[78] I Vurgaftman, JR Meyer, and LR Ram-Mohan. Band parameters for iii–v compound semiconductors and their alloys. *Journal of applied physics*, 89(11):5815–5875, 2001.

[79] Eisuke Tokumitsu. Correlation between fermi level stabilization positions and maximum free carrier concentrations in iii–v compound semiconductors. *Japanese Journal of Applied Physics*, 29(5A):L698, 1990.

[80] Vilianne Ntsame Guilengui. *Technologie et etude de resonateurs plasmoniques a base d'InAsSb: vers une plasmonique tout semi-conducteur*. PhD thesis, Montpellier 2, 2013.

[81] Anthony J Hoffman, Leonid Alekseyev, Scott S Howard, Kale J Franz, Dan Wasserman, Viktor A Podolskiy, Evgenii E Narimanov, Deborah L Sivco, and Claire Gmachl. Negative refraction in semiconductor metamaterials. *Nature materials*, 6(12):946, 2007.

[82] DC Adams, Sandeep Inampudi, T Ribaudo, D Slocum, S Vangala, NA Kuhta, WD Goodhue, Viktor A Podolskiy, and D Wasserman. Funneling light through a subwavelength aperture with epsilon-near-zero materials. *Physical review letters*, 107(13):133901, 2011.

[83] Hou-Tong Chen, Willie J Padilla, Joshua MO Zide, Arthur C Gossard, Antoinette J Taylor, and Richard D Averitt. Active terahertz metamaterial devices. *Nature*, 444(7119):597, 2006.

[84] Young Chul Jun, Edward Gonzales, John L Reno, Eric A Shaner, Alon Gabbay, and Igal Brener. Active tuning of mid-infrared metamaterials by electrical control of carrier densities. *Optics express*, 20(2):1903–1911, 2012.

[85] A Kasic, M Schubert, S Einfeldt, D Hommel, and TE Tiwald. Free-carrier and phonon properties of n-and p-type hexagonal gan films measured by infrared ellipsometry. *Physical Review B*, 62(11):7365, 2000.

[86] Jinn-Kong Sheu and GC Chi. The doping process and dopant characteristics of gan. *Journal of Physics: Condensed Matter*, 14(22):R657, 2002.

[87] Mário Silveirinha and Nader Engheta. Tunneling of electromagnetic energy through subwavelength channels and bends using ε-near-zero materials. *Physical review letters*, 97(15):157403, 2006.

[88] Nader Engheta. Pursuing near-zero response. *Science*, 340(6130):286–287, 2013.

[89] Iñigo Liberal and Nader Engheta. Near-zero refractive index photonics. *Nature Photonics*, 11(3):149, 2017.

[90] Brian Edwards, Andrea Alù, Michael E Young, Mário Silveirinha, and Nader Engheta. Experimental verification of epsilon-near-zero metamaterial coupling and energy squeezing using a microwave waveguide. *Physical review letters*, 100(3):033903, 2008.

[91] Richard W Ziolkowski. Propagation in and scattering from a matched metamaterial having a zero index of refraction. *Physical Review E*, 70(4):046608, 2004.

[92] Mário G Silveirinha, Andrea Alù, Brian Edwards, and Nader Engheta. Overview of theory and applications of epsilon-near-zero materials. In *URSI General Assembly*, page 44. Citeseer, 2008.

[93] Stefan Enoch, Gérard Tayeb, Pierre Sabouroux, Nicolas Guérin, and Patrick Vincent. A metamaterial for directive emission. *Physical Review Letters*, 89(21):213902, 2002.

[94] Andrea Alu, Mário G Silveirinha, Alessandro Salandrino, and Nader Engheta. Epsilon-near-zero metamaterials and electromagnetic sources: Tailoring the radiation phase pattern. *Physical review B*, 75(15):155410, 2007.

[95] Andrea Alù and Nader Engheta. Achieving transparency with plasmonic and metamaterial coatings. *Physical Review E*, 72(1):016623, 2005.

[96] Jongbum Kim, Aveek Dutta, Gururaj V Naik, Alexander J Giles, Francisco J Bezares, and Chase T Ellis. Role of epsilon-near-zero substrates in the optical response of plasmonic antennas. *Optica*, 3(3):339–346, 2016.

[97] Sebastian A. Schulz, Asad A. Tahir, M. Zahirul Alam, Jeremy Upham, Israel De Leon, and Robert W. Boyd. Optical response of dipole antennas on an epsilon-near-zero substrate. *Phys. Rev. A*, 93:063846, Jun 2016.

[98] Francisco Javier González and Javier Alda. Spectral response and far-field pattern of a dipole nano-antenna on metamaterial substrates having near-zero and negative indices of refraction. *Optics Communications*, 284(5):1429–1434, 2011.

[99] Crissy Rhodes, Stefan Franzen, Jon-Paul Maria, Mark Losego, Donovan N Leonard, Brian Laughlin, Gerd Duscher, and Stephen Weibel. Surface plasmon resonance in conducting metal oxides. *Journal of Applied Physics*, 100(5):054905, 2006.

[100] Satyendra K Mishra and Banshi D Gupta. Surface plasmon resonance-based fiber-optic hydrogen gas sensor utilizing indium–tin oxide (ito) thin films. *Plasmonics*, 7(4):627–632, 2012.

[101] Gururaj V Naik, Jingjing Liu, Alexander V Kildishev, Vladimir M Shalaev, and Alexandra Boltasseva. Demonstration of al: Zno as a plasmonic component for near-infrared metamaterials. *Proceedings of the National Academy of Sciences*, 109(23):8834–8838, 2012.

[102] Guillermo Garcia, Raffaella Buonsanti, Evan L Runnerstrom, Rueben J Mendelsberg, Anna Llordes, Andre Anders, Thomas J Richardson, and Delia J Milliron. Dynamically modulating the surface plasmon resonance of doped semiconductor nanocrystals. *Nano letters*, 11(10):4415–4420, 2011.

[103] Frank HL Koppens, Darrick E Chang, and F Javier Garcia de Abajo. Graphene plasmonics: a platform for strong light–matter interactions. *Nano letters*, 11(8):3370–3377, 2011.

[104] AN Grigorenko, Marco Polini, and KS Novoselov. Graphene plasmonics. *Nature photonics*, 6(11):749, 2012.

[105] Garcia de Abajo F Javier. Graphene plasmonics: challenges and opportunities. *Acs Photonics*, 1(3):135–152, 2014.

[106] Andrea C Ferrari and Denis M Basko. Raman spectroscopy as a versatile tool for studying the properties of graphene. *Nature nanotechnology*, 8(4):235, 2013.

[107] Daniel Rodrigo, Odeta Limaj, Davide Janner, Dordaneh Etezadi, F Javier Garcia de Abajo, Valerio Pruneri, and Hatice Altug. Mid-infrared plasmonic biosensing with graphene. *Science*, 349(6244):165–168, 2015.

[108] Tony Low and Phaedon Avouris. Graphene plasmonics for terahertz to mid-infrared applications. *ACS nano*, 8(2):1086–1101, 2014.

[109] Zizhuo Liu and Koray Aydin. Localized surface plasmons in nanostructured monolayer black phosphorus. *Nano letters*, 16(6):3457–3462, 2016.

[110] Ernst Abbe. Beiträge zur theorie des mikroskops und der mikroskopischen wahrnehmung. *Archiv für mikroskopische Anatomie*, 9(1):413–418, 1873.

[111] EdwardH Synge. Xxxviii. a suggested method for extending microscopic resolution into the ultra-microscopic region. *The London, Edinburgh, and Dublin Philosophical Magazine and Journal of Science*, 6(35):356–362, 1928.

[112] Brief history and simple description of nsom/snom technology. `http://www.nanonics.co.il/nsom-navigation/a-brief-history-and-simple-description-of-nsom-snom-technology`, 2007.

[113] EA Ash and G Nicholls. Super-resolution aperture scanning microscope. *Nature*, 237(5357):510–512, 1972.

[114] Wolfgang D Pohl. Optical near-field scanning microscope, August 5 1986. US Patent 4,604,520.

[115] Dieter W Pohl, W Denk, and M Lanz. Optical stethoscopy: Image recording with resolution $\lambda/20$. *Applied physics letters*, 44(7):651–653, 1984.

[116] A Lewis, M Isaacson, A Harootunian, and A Muray. Development of a 500 å spatial resolution light microscope: I. light is efficiently transmitted through $\lambda/16$ diameter apertures. *Ultramicroscopy*, 13(3):227–231, 1984.

[117] A Harootunian, E Betzig, M Isaacson, and A Lewis. Super-resolution fluorescence near-field scanning optical microscopy. *Applied Physics Letters*, 49(11):674–676, 1986.

[118] Eric Betzig, Jayk Trautman, et al. Near-field optics- microscopy, spectroscopy, and surface modification beyond the diffraction limit. *Science*, 257(5067):189–195, 1992.

[119] John Wessel. Surface-enhanced optical microscopy. *JOSA B*, 2(9):1538–1541, 1985.

[120] M Specht, JD Pedarnig, WM Heckl, and TW Hänsch. Scanning plasmon near-field microscope. *Physical review letters*, 68(4):476, 1992.

[121] Yasushi Inouye and Satoshi Kawata. Near-field scanning optical microscope with a metallic probe tip. *Optics letters*, 19(3):159–161, 1994.

[122] F Zenhausern, MP Oâboyle, and HK Wickramasinghe. Apertureless near-field optical microscope. *Applied Physics Letters*, 65(13):1623–1625, 1994.

[123] A Lahrech, R Bachelot, P Gleyzes, and AC Boccara. Infrared-reflection-mode near-field microscopy using an apertureless probe with a resolution of $\lambda/600$. *Optics letters*, 21(17):1315–1317, 1996.

[124] B Hecht, H Bielefeldt, Y Inouye, DW Pohl, and L Novotny. Facts and artifacts in near-field optical microscopy. *Journal of Applied Physics*, 81(6):2492–2498, 1997.

[125] Anasys instruments. `https://www.anasysinstruments.com`, 2005. Santa Barbara, USA.

[126] Nanonics imaging ltd. `http://www.nanonics.co.il`, 2007. Jerusalem, Israel.

[127] Witec gmbh. `http://www.witec.de`, 2007. Ulm, Germany.

[128] Nt-mdt spectrum instruments. `http://www.ntmdt-si.com`, 1989. Moscow,Russia.

[129] Nicholas E Dickenson, Kevin P Armendariz, Heath A Huckabay, Philip W Livanec, and Robert C Dunn. Near-field scanning optical microscopy: a tool for nanometric exploration of biological membranes. *Analytical and bioanalytical chemistry*, 396(1):31–43, 2010.

[130] Hiroshi Muramatsu, Norio Chiba, Katsunori Homma, Kunio Nakajima, Tatsuaki Ataka, Satoko Ohta, Akihiro Kusumi, and Masamichi Fujihira. Near-field optical microscopy in liquids. *Applied physics letters*, 66(24):3245–3247, 1995.

[131] J Seidel, S Grafström, Ch Loppacher, S Trogisch, F Schlaphof, and LM Eng. Near-field spectroscopy with white-light illumination. *Applied Physics Letters*, 79(14):2291–2293, 2001.

[132] E Betzig, M Isaacson, and A Lewis. Collection mode near-field scanning optical microscopy. *Applied physics letters*, 51(25):2088–2090, 1987.

[133] N Hosaka and Toshiharu Saiki. Near-field fluorescence imaging of single molecules with a resolution in the range of 10 nm. *Journal of microscopy*, 202(2):362–364, 2001.

[134] L Novotny, DW Pohl, and B Hecht. Scanning near-field optical probe with ultrasmall spot size. *Optics letters*, 20(9):970–972, 1995.

[135] Liang Wang, Sreemanth M Uppuluri, Eric X Jin, and Xianfan Xu. Nanolithography using high transmission nanoscale bowtie apertures. *Nano letters*, 6(3):361–364, 2006.

[136] JA Matteo, DP Fromm, Y Yuen, PJ Schuck, WE Moerner, and L Hesselink. Spectral analysis of strongly enhanced visible light transmission through single c-shaped nanoapertures. *Applied Physics Letters*, 85(4):648–650, 2004.

[137] Thomas W Ebbesen, H J Lezec, HF Ghaemi, Tineke Thio, and PA Wolff. Extraordinary optical transmission through sub-wavelength hole arrays. *Nature*, 391(6668):667–669, 1998.

[138] B Knoll and F Keilmann. Near-field probing of vibrational absorption for chemical microscopy. *Nature*, 399(6732):134, 1999.

[139] Nicola Maghelli, Massimiliano Labardi, Salvatore Patanè, F Irrera, and Maria Allegrini. Optical near-field harmonic demodulation in apertureless microscopy. *Journal of microscopy*, 202(1):84–93, 2001.

[140] Renaud Bachelot, Gilles Lerondel, Sylvain Blaize, Sebastien Aubert, Aurelien Bruyant, and Pascal Royer. Probing photonic and optoelectronic structures by apertureless scanning near-field optical microscopy. *Microscopy research and technique*, 64(5-6):441–452, 2004.

[141] Terefe Getaneh Habteyes, Isabelle Staude, Katie E Chong, Jason Dominguez, Manuel Decker, Andrey Miroshnichenko, Yuri Kivshar, and Igal Brener. Near-field mapping of optical modes on all-dielectric silicon nanodisks. *ACS Photonics*, 1(9):794–798, 2014.

[142] Rainer Hillenbrand and Fritz Keilmann. Complex optical constants on a subwavelength scale. *Physical Review Letters*, 85(14):3029, 2000.

[143] Monika Fleischer. Near-field scanning optical microscopy nanoprobes. *Nanotechnology Reviews*, 1(4):313–338, 2012.

[144] Bernhard Knoll and Fritz Keilmann. Enhanced dielectric contrast in scattering-type scanning near-field optical microscopy. *Optics communications*, 182(4-6):321–328, 2000.

[145] R Hillenbrand, B Knoll, and F Keilmann. Pure optical contrast in scattering-type scanning near-field microscopy. *Journal of microscopy*, 202(1):77–83, 2001.

[146] Abeer Al Mohtar, Julien Vaillant, Zoreh Sedaghat, Michel Kazan, Lilian Joly, Claudia Stoeffler, Julien Cousin, A Khoury, and Aurélien Bruyant. Generalized lock-in detection for interferometry: application to phase sensitive spectroscopy and near-field nanoscopy. *Optics express*, 22(18):22232–22245, 2014.

[147] Takuya Matsumoto, Tsutomu Ichimura, Takashi Yatsui, Motonobu Kourogi, Toshiharu Saiki, and Motoichi Ohtsu. Fabrication of a near-field optical fiber probe with a nanometric metallized protrusion. *Optical review*, 5(6):369–373, 1998.

[148] F Keilmann. Surface-polariton propagation for scanning near-field optical microscopy application. *Journal of microscopy*, 194(2-3):567–570, 1999.

[149] Zohreh Sedaghat, Anna Rumyantseva, Aurélien Bruyant, Sergei Kostcheev, Sylvain Blaize, Safi Jradi, Renaud Bachelot, and Antoine Monmayrant. Near-field optical imaging with a nanotip grown on fibered polymer microlens. *Applied Physics Letters*, 100(3):033107, 2012.

[150] JD Jackson. Classical electrodynamics. *Classical Electrodynamics, New York: Wiley, 1962*, 1962.

[151] JE Sipe, Jeff F Young, JS Preston, and HM Van Driel. Laser-induced periodic surface structure. i. theory. *Physical Review B*, 27(2):1141, 1983.

[152] Ole Keller, Mufei Xiao, and Sergey Bozhevolnyi. Configurational resonances in optical near-field microscopy: a rigorous point-dipole approach. *Surface science*, 280(1-2):217–230, 1993.

[153] Olivier JF Martin, Alain Dereux, and Christian Girard. Iterative scheme for computing exactly the total field propagating in dielectric structures of arbitrary shape. *JOSA A*, 11(3):1073–1080, 1994.

[154] Lukas Novotny and Bert Hecht. *Principles of nano-optics*. Cambridge university press, 2012.

[155] David G Grier. Optical tweezers in colloid and interface science. *Current opinion in colloid & interface science*, 2(3):264–270, 1997.

[156] Xiaolin Wang, Shuxun Chen, Marco Kong, Zuankai Wang, Kevin D Costa, Ronald A Li, and Dong Sun. Enhanced cell sorting and manipulation with combined optical tweezer and microfluidic chip technologies. *Lab on a Chip*, 11(21):3656–3662, 2011.

[157] Gregor Thalhammer, Lisa Obmascher, and Monika Ritsch-Marte. Direct measurement of axial optical forces. *Optics express*, 23(5):6112–6129, 2015.

[158] Indrajith Rajapaksa. *Image Force Microscopy*. PhD thesis, 2011.

[159] I Rajapaksa, K Uenal, and H Kumar Wickramasinghe. Image force microscopy of molecular resonance: A microscope principle. *Applied physics letters*, 97(7):073121, 2010.

[160] Molecular vista inc. `http://www.molecularvista.com`, 2011. California, USA.

[161] Junghoon Jahng, Dmitry A Fishman, Sung Park, Derek B Nowak, Will A Morrison, H Kumar Wickramasinghe, and Eric O Potma. Linear and nonlinear optical spectroscopy at the nanoscale with photoinduced force microscopy. *Accounts of chemical research*, 48(10):2671–2679, 2015.

[162] Oleh M Tanchak and Christopher J Barrett. Light-induced reversible volume changes in thin films of azo polymers: the photomechanical effect. *Macromolecules*, 38(25):10566–10570, 2005.

[163] Honghua U Yang and Markus B Raschke. Resonant optical gradient force interaction for nano-imaging and-spectroscopy. *New Journal of Physics*, 18(5):053042, 2016.

[164] Junghoon Jahng, Sung Park, Will A Morrison, Hyuksang Kwon, Derek Nowak, Eric O Potma, and Eun Seong Lee. Nanoscale spectroscopic studies of two different physical origins of the tip-enhanced force in photo-induced force microscopy. *arXiv preprint arXiv:1711.02479*, 2017.

[165] Thejaswi U Tumkur, Xiao Yang, Benjamin Cerjan, Naomi J Halas, Peter Nordlander, and Isabell Thomann. Photoinduced force mapping of plasmonic nanostructures. *Nano letters*, 16(12):7942–7949, 2016.

[166] Antonio Ambrosio, Luis A Jauregui, Siyuan Dai, Kundan Chaudhary, Michele Tamagnone, Michael M Fogler, Dimitri N Basov, Federico Capasso, Philip Kim, and William L Wilson. Mechanical detection and imaging of hyperbolic phonon polaritons in hexagonal boron nitride. *ACS nano*, 11(9):8741–8746, 2017.

[167] Antonio Ambrosio, Michele Tamagnone, Kundan Chaudhary, Luis A Jauregui, Philip Kim, William L Wilson, and Federico Capasso. Selective excitation and imaging of ultraslow phonon polaritons in thin hexagonal boron nitride crystals. *Light: Science & Applications*, 7(1):27, 2018.

[168] Witec gmbh. `http://www.witec.de`, 2007. Ulm, Germany.

[169] Kishan Dholakia and Pavel Zemánek. Colloquium: Gripped by light: Optical binding. *Reviews of modern physics*, 82(2):1767, 2010.

[170] JR Arias-González and M Nieto-Vesperinas. Optical forces on small particles: attractive and repulsive nature and plasmon-resonance conditions. *JOSA A*, 20(7):1201–1209, 2003.

[171] Junghoon Jahng, Jordan Brocious, Dmitry A Fishman, Fei Huang, Xiaowei Li, Venkata Ananth Tamma, H Kumar Wickramasinghe, and Eric Olaf Potma. Gradient and scattering forces in photoinduced force microscopy. *Physical Review B*, 90(15):155417, 2014.

[172] Faezeh Tork Ladani and Eric Olaf Potma. Dyadic green's function formalism for photoinduced forces in tip-sample nanojunctions. *Physical Review B*, 95(20):205440, 2017.

[173] Franziska Barho. *Ingénierie de résonateurs plasmoniques à base de semiconducteurs fortement dopés pour l'exaltation de l'absorption de molécules dans le moyen infrarouge.* PhD thesis, Montpellier 2, 2017.

[174] ZH Nie, D Fava, E Kumacheva, HE Ruda, and A Shik. Plasmon spectra in two-dimensional nanorod arrays. *Nanotechnology*, 20(29):295203, 2009.

[175] Maria Kulawik, Marek Nowicki, Gero Thielsch, Ludger Cramer, H-P Rust, H-J Freund, Thomas P Pearl, and Paul S Weiss. A double lamellae dropoff etching procedure for tungsten tips attached to tuning fork atomic force microscopy/scanning tunneling microscopy sensors. *Review of scientific instruments*, 74(2):1027–1030, 2003.

[176] Aurélien Bruyant, Julien Vaillant, Tzu-Heng Wu, Yunlong Zhu, Yi Huang, and Abeer Al Mohtar. Interferometry using generalized lock-in amplifier (g-lia): A versatile approach for phase-sensitive sensing and imaging. In *Optical Interferometry*. InTech, 2017.

[177] Sébastien Aubert, Aurélien Bruyant, Sylvain Blaize, Renaud Bachelot, Gilles Lerondel, Sylvain Hudlet, and Pascal Royer. Analysis of the interferometric effect of the background light in apertureless scanning near-field optical microscopy. *JOSA B*, 20(10):2117–2124, 2003.

[178] Abeer Al Mohtar. *Localized surface plasmon and phonon polaritons investigated by mid-infrared spectroscopy and near-field nanoscopy*. PhD thesis, University of Technology of Troyes, 2015.

[179] Newport corporation. `https://www.newport.com/f/reflective-microscope-objectives`, 1938. California, US.

[180] Mario Bomers, Aude Mezy, Laurent Cerutti, Franziska Barho, Gonzalez Posada Flores, Eric TourniÃ©, and Thierry Taliercio. Phosphonate monolayers on inassb:si and gasb surfaces for mid-ir plasmonics. *Applied Surface Science*, 451:241–249, 2018.

[181] Franziska B Barho, Fernando Gonzalez-Posada, Maria-Jose Milla, Mario Bomers, Laurent Cerutti, Eric Tournié, and Thierry Taliercio. Highly doped semiconductor plasmonic nanoantenna arrays for polarization selective broadband surface-enhanced infrared absorption spectroscopy of vanillin. *Nanophotonics*, 2017.

[182] Thierry Taliercio, Fernando Gonzalez-Posada Flores, Franziska B Barho, María José Milla-Rodrigo, Mario Bomers, Laurent Cerutti, and Eric Tournié. Plasmonic biosensing based on highly doped semiconductors. In *Optical Sensing, Imaging, and Photon Counting: Nanostructured Devices and Applications 2017*, volume 10353, page 103530S. International Society for Optics and Photonics, 2017.

[183] Alexander A Balandin. Thermal properties of graphene and nanostructured carbon materials. *Nature materials*, 10(8):569, 2011.

[184] Shanshan Chen, Qingzhi Wu, Columbia Mishra, Junyong Kang, Hengji Zhang, Kyeongjae Cho, Weiwei Cai, Alexander A Balandin, and Rodney S Ruoff. Thermal conductivity of isotopically modified graphene. *Nature materials*, 11(3):203, 2012.

Yi HUANG

Doctorat : Matériaux, Mécanique, Optique et Nanotechnologie

Année 2018

Nanospectroscopie infrarouge de structures semiconductrices fortement dopées par microscopie à sonde diffusante et microscopie de force photoinduite

Dans cette thèse, les propriétés plasmoniques de nanostructures d'InAsSb fortement dopées (HDSC : Highly doped Semiconductor) sont étudiées par nanoscopie de champ proche dans l'infrarouge moyen. Après une introduction sur les matériaux plasmoniques dans l'infrarouge, nous présentons les outils de caractérisation associés. Ici, deux types d'échantillons sont étudiés, des réseaux 1D et des réseau 2D d'HDSC. Ces échantillons sont caractérisés par microscopie de champ proche optique à sonde diffusante (s-SNOM) et par une technique plus récente de microscopie à force photoinduite (PiFM). Les aspects fondamentaux et instrumentaux de ces deux approches nanoscopiques sont présentés. Pour les réseaux HDSC, les deux techniques de nano-imagerie spectroscopiques sont mises en œuvre au voisinage de la fréquence plasma, où la fonction diélectrique avoisine zéro (ENZ : Epsilon-Near-Zero material). Les réponses obtenues par ces deux techniques sont alors comparées et discutées. Pour les réseaux bidimensionnels, l'analyse est réalisée par la microscopie à sonde diffusante, sensible à la phase, qui révèle l'existence d'un mode d'arête extrêmement confiné, comme prédit par les simulations électromagnétiques.

Mots clés : plasmons - microscopie en champ proche - spectroscopie infrarouge – nanotechnologie - matériaux nanostructurés.

Local Infrared Spectroscopy of Highly Doped Semiconductor Structures Based on Scattering-type Nanoscopy and Photoinduced Force Microscopy

In this thesis, highly doped semiconductor (HDSC) InAsSb nanostructures have been investigated by near-field nanoscopy in the mid-infrared range. First, infrared plasmonic materials are introduced as well as well as the characterization tools used in this thesis. Herein, two types of nanostructured HDSC samples are studied: HDSC 1D gratings and HDSC 2D array. To characterize the HDSC samples, both phase-sensitive scattering type nanoscopy (s-SNOM) and the more recent Photoinduced Force Microscopy (PiFM) are used. The fundamental aspects of these two microscopies are presented and detailed instrumental information is provided. For HDSC 1D gratings, both techniques are used for spectroscopic nano-imaging in the vicinity of the plasma frequency, where the material behaves as an epsilon-near-zero (ENZ) material. The two responses are compared and discussed in terms of model. For HDSC 2D array, the investigation is carried out by s-SNOM. Both localized plasmonic resonance and ENZ properties are observed and compared with analytical simulations. The signature of a highly localized surface plasmon resonance confined on the edge mode is observed in the experimental images, in agreement with electromagnetic simulations.

Keywords: plasmons (physics) - near-field microscopy - infrared spectroscopy – nanotechnology - nanostructured materials.

Thèse réalisée en partenariat entre :

Ecole Doctorale "Sciences pour l'Ingénieur"